Universidad Nacional Autónoma
de México

Posgrado en Ciencia e Ingeniería de Materiales

Study of the properties of bubble flows in non-Newtonian fluids

TESIS

que para obtener el grado de

Doctor en Ciencia e Ingeniería de Materiales

presenta

Juan Rodrigo Vélez Cordero

Asesor: Dr. Roberto Zenit Camacho

México D.F. 2011

Esta tesis esta dedicada a la memoria de

mi abuelo Juan Vélez Muciño,

porque los esfuerzos del pasado

son los logros del presente

JURADO ASIGNADO

Presidente: Dr. Francisco Javier Solorio Ordaz

Secretario: Dr. Ángel Enrique Chávez Castellanos

Primer Vocal: Dr. Roberto Zenit Camacho

Segundo Vocal: Dr. James J. Feng

Tercer Vocal: Dr. Enrique Geffroy Aguilar

Sitio donde se realizó la tesis:

Instituto de Investigaciones en Materiales UNAM
Departamento de Reología

University of British Columbia
Department of Chemical and Biological Engineering

Tutor:
Dr. Roberto Zenit Camacho

en colaboración con el
Dr. James J. Feng

AGRADECIMIENTOS

Agradezco:

a Dios por toda su creación y hacer de la viscoelasticidad una propiedad comprensible (hasta cierto punto)

a mis padres, por todo su amor y apoyo en estos cuatro años de trabajo (incluyendo el económico); a mi Madre por inyectarme de su gran alegría y entusiasmo cada semana, a mi Padre por todos los ratos de retiro en los valles de Morelos, a Magda por sus palabras espirituales, a Franky por ser un gran “Tejano” y compartir su vida con nosotros

a mi hermano Eluar y a su novia Nancy por hacer interesantes y placenteros los fines de semana, sea en casa o en la eterna Coyoacán

al pastor Gustavo Mejía y a la Iglesia Reencuentro, porque si el alma no esta bien, nada lo esta

a mis amigos del alma: Barbara Betancourt, Cristina Krap y Diego Sámano, por estar en *todos* los momentos, gracias por poder confiarles la historia de mi vida

a todas las amigas y amigos del Insituto de Investigaciones en Materiales, muy especialmente a Ismael Garduño y Alejandro Ortiz, por incluirme en tantas actividades y hacerme sentir parte del grupo. No me olvido en ninguna manera de todos los demás y me da miedo ponerlos por omitir alguno

a mi tutor, Roberto Zenit, por haber sido mi gran maestro en todo esto, y, seguramente; un gran amigo y colaborador en el futuro

a todos los que ayudaron directamente a la realización de esta tesis: James Feng (colaborador en la UBC), Diego Sámano (estudio de la interacción de dos burbujas), Mariana Ramírez Gilly, Fausto Calderas y Luis Medina (mediciones reológicas), Miguel Ángel Pineda, Adrian Gallardo, Fernando Molina y Miguel Díaz (construcción del banco de capilares y columna de burbujeo, taller del IIM), Pengtao Yue y Diwen Zhou (simulaciones numéricas), Enrique Soto (colaborador cuyo trabajo es antecedente directo del presente), Alberto Tecante y Octavio Manero (parte del comité tutor)

al grupo de fluidos multifásicos: (como en las películas, los puse por orden de aparición): a Ernesto (su mente es tan compleja como el tema que estudia: turbulencia), a Charly (el gran conocedor de la técnica PIV y Señor de los vórtices), Rene (porque mi vida podría ser parte de una super-matrix hecha por el), Fede (la mezcla perfecta entre ficción y realidad, niñez y madurez, master de las computadoras), Adriana (por su ejemplo de persistencia en el trabajo y por enseñarme que no es necesario dicer mucho para comunicar poco), Santos (experto en LabView, criollo por deseo y chilango a la fuerza), Mónica (por Acapulco, por adaptarse tan bien a un laboratorio lleno de hombres, por haber tenido algo bello que ver en el lab entre tanto ...), Enrique Sandoval (por abrirnos su casa, por la música en el lab, conocedor de flujo de partículas, desde canicas hasta football), Enrique Guzmán (futuro erudito, una platica superficial con el valen cientos de platicas profundas), Isaías (por apoyarme en mis dudas acerca de la hermana de los flujos burbujeantes, la sedimentación; por estar en el estudio y en el juego), a todas las “niñas” y “niños” del lab: Carolina (válvulas cardiacas), Julian (robo-espermas) ... diría el Roger: *“miles de veces la viscosidad del agua te cuesta un apéndice”*

a todo el personal académico y administrativo del Instituto de Investigaciones en Materiales, muy en especial, a Juan Hernández Cordero, por su apoyo y amistad; al Coordinador del posgrado en ciencia e ingeniería de materiales, Dr. Tatsuo Akachi; a sus asistentes: Lilia García, Ma. Esther Carrillo e Isabel Gómez.

Ciudad Universitaria, México, marzo del 2011

Resumen

El presente trabajo trata sobre las propiedades hidrodinámicas de ensambles de burbujas en soluciones poliméricas (no Newtonianas). Se obtuvieron mediciones cualitativas o cuantitativas del tamaño medio de burbuja, velocidad media de burbuja, dispersión de las burbujas, varianza de la velocidad de burbuja y niveles de agitación en el líquido. Este trabajo difiere de los muchos otros que se han hecho en el campo por dos principales razones: En primer lugar, ofrece un estudio de tales propiedades teniendo una monodispersión del tamaño de burbuja; esto nos permite asilar los efectos causados sólo por la interacción hidrodinámica entre burbujas. En segundo lugar, analiza por separado los efectos que tienen los gradientes de viscosidad y la elasticidad en el flujo. Los resultados obtenidos en la columna de burbujeo fueron complementados con el estudio experimental y numérico de la interacción entre dos burbujas. Para los experimentos se empleo una cámara de alta velocidad y la técnica de imagen de velocimetría de partículas para caracterizar el campo de flujo. Las simulaciones numéricas se realizaron con la técnica Arbitraria Lagrangiana-Euleriana. Los fluidos adelgazantes ($0.3 < n < 0.8$) fueron hechos con soluciones de xantana mientras que los fluidos tipo Boger (líquidos con elasticidad y viscosidad casi constante) fueron hechos con soluciones de poliacrilamida (semidiluidas) y un polímero asociativo (concentradas).

En los fluidos adelgazantes se encontró que la velocidad media de ascenso de las burbujas resultó mayor que aquellas medidas en las burbujas individuales, en conformidad con estudios anteriores. Se encontró que la magnitud de la velocidad del ensamble de burbujas es determinada grandemente por al aparición de cúmulos de burbujas. Dichos cúmulos, los cuales aparecen para determinados valores del índice de flujo y diámetro de burbuja, presentaron una estructura muy diferente a aquellos observados en fluidos Newtonianos. Además, se encontró que la aparición de cúmulos produce un incremento dramático en la varianza de la velocidad de burbuja dentro de la columna. Se identificaron una serie de condiciones para la aparición de cúmulos de burbujas en estos fluidos. En relación con esta capacidad de formación de cúmulos hallada en columnas burbujeantes con líquidos adelgazantes inelásticos, se encontró además que un par de burbujas ascendiendo en los mismos fluidos mostraron un comportamiento diferente al típicamente mostrado por un fluido Newtoniano. La diferencia más notable se presentó en el proceso denominado “drafting-kissing-tumbling” o DKT, por sus siglas en inglés: para el caso del par de burbujas ascendiendo en los fluidos adelgazantes, la fase de “tumbling” o “de voltereta” (las burbujas se separan después de juntarse) no ocurre y las burbujas forman un par estable. El proceso DKT es igualmente influenciado por la cantidad de inercia y deformabilidad de las burbujas individuales y por el ángulo inicial entre ellas. Los resultados experimentales y numéricos sugieren que la estela adelgazante formada detrás de las burbujas juega un papel importante en la velocidad del par y en la formación de cúmulos en los fluidos adelgazantes.

En el caso del fluido Boger semidiluido, se encontró que la dispersión de las burbujas y los niveles de agitación en el líquido están relacionados con el valor del volumen crítico en el cual aparece la discontinuidad del salto de velocidad en las burbujas individuales. Para las burbujas con un volumen menor al crítico se formaron grandes cúmulos verticales. Cuando las burbujas tuvieron, por otro lado, un volumen mayor al crítico, la dispersión

de las burbujas se mejoró notoriamente. El análisis de los resultados sugiere que este comportamiento es debido a cambios en las condiciones de frontera en la interfase gas-líquido, específicamente, de una condición rígida a una de “resbalamiento” o libre de esfuerzos. Esta hipótesis fue igualmente apoyada por las curvas de volumen-velocidad obtenidas con la solución Boger concentrada para las burbujas individuales y para grupos de burbujas. Finalmente, vale la pena decir que la formación de cúmulos en fluidos elásticos también depende de la cantidad de esfuerzo elástico acumulado durante el paso consecutivo de burbujas.

Abstract

The present work considers the hydrodynamic properties of bubble swarms rising in polymeric (non-Newtonian) solutions. Qualitative or quantitative measurement of the mean bubble size, mean bubble velocity, bubble dispersion, bubble velocity variance and agitation levels in the liquid were obtained. This work differs from the many others that have been done in the field for two main reasons: First, it offers a study of such properties having a nearly mono-dispersed bubble size; this allows us to isolate the effects caused solely by the hydrodynamic interaction among bubbles. Second, it analyzes separately the effects that the viscosity gradients and elasticity have on the flow. The results obtained in the bubble column were complemented with the experimental and numerical study of the interaction of two bubbles. For the experiments, a high speed camera and the Particle Image Velocimetry technique were used to characterize the flow field. The numerical simulations were conducted with the Arbitrary Lagrangian-Eulerian technique. The thinning fluids ($0.3 < n < 0.8$) were made with xanthan gum solutions while the Boger-type fluids (liquids with elasticity and nearly constant viscosity) were made with solution of polyacrylamide (semidiluted) and an associative polymer (concentrated).

For the thinning fluids it was found that the mean rise velocity of the bubbles was larger than that of an individual bubble, in accordance with previous studies. The magnitude of the swarm velocity was found to be greatly influenced by the appearance of bubble clusters. These bubble clusters, which appeared for certain values of the flow index and bubble diameter, were found to have a very different structure from those observed in Newtonian liquids. Furthermore, it was found that the appearance of clusters produced a dramatic increase of the bubble velocity variance within the column. A set of conditions was also identified for the appearance of bubble clusters in this fluids.

In relation with this clustering capacity found in shear-thinning inelastic bubbly columns, it was found that a pair of bubbles rising in the same fluids showed a different behavior from the typical Newtonian one. The most noticeable difference is the so-called drafting-kissing-tumbling (DKT) process: for the case of bubbles rising in thinning fluids, the tumbling phase does not occur and the pair tends to form a stable doublet. The DKT process is also influenced by the amount of inertia and deformability of the individual bubbles and the initial angle between them. The experimental and numerical results suggest that the thinning wake formed behind the bubbles plays an important role in the speed of the pair and the formation of clusters in thinning fluids.

In the case of the semidiluted Boger fluid, it was found that the bubble dispersion and agitation values within the liquid were highly related with the value of the critical volume at which the velocity discontinuity occurs in the single bubble case. For bubbles having a volume below the critical one, large vertical clusters were formed. When the bubbles had, on the other hand, a volume above the critical one, the bubble dispersion was significantly improved. The analysis of the results suggest that this behavior is due to changes of the boundary conditions at the gas-liquid interface, specifically, from a rigid to a stress-free or slip boundary condition. This hypothesis was also supported by the volume-velocity curves obtained for the concentrated Boger solution with single bubbles and bubble groups. Finally, it is worth mentioning that the formation of clusters in elastic fluids also depend on the amount of elastic stress accumulated during the consecutive

passage of bubbles.

Contents

Chapter 1

Introduction

1.1 The birth of a new discipline

It was the beginnings of the forties of the last century and the world was heading to the second biggest war in history. As many others American citizens, Elmer L. Gaden was sent abroad to serve the U.S. Navy (Humphrey 1991). Perhaps, Elmer heard the news about the healing capacity of the penicillin used in infected battle wounds (Katzen & Tsao 2000). After the war ended, people working in the pharmaceutical business turned their attention to the mass-production of penicillin and other antibiotics such as streptomycin and tetracycline (Humphrey 1991). The engineers that were in charge of the project realized that the most efficient way to produce large quantities of penicillin was by aerobic submerged culture of the strains penicillin-producing fungi; however, in those days no one knew how to this, in other words, no one knew how to design a bioreactor capable to supply the oxygen demand of the biochemical reaction. The Merck Chemical Company made an important contribution in the subject and Elmer was in the center of the research (Humphrey 1991): he explained how to estimate the amount of oxygen needed to run an effective fermentation. Elmer L. Gaden was a pioneer of a new branch of the chemical engineering that we now know as "biochemical engineering" and which deals specifically with chemical reactions that employ living organisms as catalysts.

1.2 Biochemical engineers learning rheology

After the introduction of an efficient submerged culture process, the production of antibiotics became a very profitable business: in the last years the production of antibiotics has been about 35,000 tons per year with sales of about $30 billion USD (Gavrilescu & Chisti 2005; now a days some may be produced by organic synthesis). Other products of interest began to be produced by a similar process: food-processing enzymes, biomass, xanthan gum and other food aditives and bioetanol, to mention a few (Gavrilescu & Chisti 2005, Kantarci *et al.* 2005). The treatment of wastewater using activated sludges also shares the same unit process (Yang *et al.* 2009, Kantarci *et al.* 2005): a liquid mixture of organic material being aerated by bubbles generated in a gas sparger and agitated by the same bubble flow or by the movement of an impeller. The biochemical engineers soon realized that such mixture of organic materials did not follow the ordinary behavior of those which we call "Newtonian fluids", that is, fluids in which the momentum per unit area and time (or stress τ) needed to maintain the fluid in movement is a linear function of the velocity gradient (or shear rate $\dot{\gamma}$):

$$\tau = -\mu\dot{\gamma} \tag{1.1}$$

where μ is the viscosity of the fluid (the formal deduction of eq. 1.1 comes from considering a pure shear flow, see Bird *et al.* 1998). For instance, water, whose molecule size is 0.278nm, follow this linear relation. We can sustain then that the viscosity of water comes form the internal friction between its molecules, picturing them as "rounded" objects. The fluids obtained in a submerged culture, typically a mix of high molecular weight products and living cells, have a very different behavior. To illustrate such difference, consider for example a fungal mycelium (such as the ones used in the production of penicillin) "floating" in the submerged culture. Using a microscope, the mycelium will look like a white mass made by many spaghetti threads (hyphae); this is the typical morphology of a fungus (Metz *et al.* 1981). Therefore, the characteristic shapes of a fungal culture are neither small not rounded. Much smaller bodies than the hyphae, like proteins and carbohydrates, secreted by the fungus into the medium, will also have a very different structure than that appointed to the molecule of water. When proteins, carbohydrates, fungal hyphae and many other tiny bodies encounter in the organic liquid are submitted to an external shear deformation, they will come aligned in the direction of the velocity field (provided that the bodies acquire an anisotropic shape); if the shear rate increases, more bodies will get the chance to attain the orientation of the velocity field. This will cause a macroscopic phenomenon known as "shear-thinning", which means the decrease of the liquid viscosity with the increase of the rate of shear deformation. One way to express such progressive decrease of the viscosity with the shear rate is by using the following empirical expression:

$$\eta = k\dot{\gamma}^{n-1} \tag{1.2}$$

where k is known as the consistency index and n the flow index, which is an indicator of the thinning behavior of the fluid. When the viscosity has a nonlinear dependence with the shear rate, the η symbol is used instead of μ. Note that for n values lower than one, the exponent becomes negative, thus the thinning behavior is obtained. When the flow index acquires a value higher than one, the exponent is positive and the viscosity will increase with the shear rate. This behavior contrast with the thinning one and its called "shear-thickening". The detailed discussion of the origin of this behavior, which can be due to the formation of structure in the microscopic level or by macroscopic interactions in particulated media, is out of the scope of the present work. More discussion on this issue can be found in Choplin & Sabatié (1986), Indei (2007), Feys *et al.* (2009). Is worth mentioning that the consistency and flow indexes do not have a transcendental physical meaning and their only purpose is to display a practical relation of the viscosity with the shear rate.

It is common to find the rheological characterization of the working fluids in biotechnological reports (Nienow 1990, Rodríguez-Monroy & Galindo 1999, Peña *et al.* 2002). For example, the culture media having the fungus *Streptomyces avermitilis* can reach a consistency index of $500 mPa \cdot s$ (water is around $1 mPa \cdot s$) and a n value of 0.3 (Nienow 1990). The culture having *Xanthomonas campestris*, used to produce xanthan gum, can reach a k value up to $1500 mPa \cdot s$ (Peña *et al.* 2002). The k and n values of another culture media and the viscosity values reached by activated sludges used in the wastewater treatment are shown in figure 1.1. We have used the case of the fermentation broths to give examples of some non-Newtonian fluids because they have a close relation with the topic of this thesis. However, the non-Newtonian fluids represent a big family of liquids which includes other polymer solutions and melts, liquid crystals, gels, suspensions, emulsions, micellar solutions, slurries and foams (Larson 1999, Kishore *et al.* 2008, see figure 1.2 for some additional examples).

Having all this range of viscosity values as a function of the shear rate and time, biochemical engineers understood that it was essential to know the rheology of the fluid in order to get a good estimation of the momentum, mass and heat transfer occurring in the bioreactor. A lot of new challenges appeared when the handing of non-Newtonian fluids became an issue. To begin with, the non-Newtonian fluids are usually more viscous than the Newtonian ones; this causes the decrease of the mass transfer coefficients and requires an improvement of the bioreactor design in order to increase the availability of gas. Other problems that appeared were the short residence time of the gas due to bubble coalescence, heterogeneous bubble distribution along the bioreactor, producer cells (like fungus or bacteria) being covered by the secreted polymer and therefore reducing the absorption rate of oxygen, cell adsorption on the air bubble surface (Lawford & Rousseau 1991, Galaction *et al.* 2004, Kilonzo & Margaritis 2004), to mention some of them. There were two ways to tackle all these problems: one was the study of the impeller design, which include the choose of the number of impellers needed along the bioreactor and the spacing between them; the other way was to study the agitation produced solely by the bubble flow. Both strategies are important in the development of gas-liquid contactors and both require a specialized knowledge in the subject. This work only focuses in the latter: the bubble columns.

1.3 Basic concepts on bubble columns

There are some good reasons for choosing bubble columns instead of the agitated vessels as gas-liquid contactors: using less mechanical parts, the bubble columns can yield the same mass transfer coefficients as the agitated vessels using similar power input values (Heijnen & Van't Riet 1984). Additionally, we can have a better control of the bubble size in non-coalescence conditions because there will be no mechanical stresses exerted on the bubble surface. However, bubble columns are highly inefficient when the viscosity of the liquid is too high (above one hundred times that of water). In those cases the use of impellers becomes indispensable.

Bubble columns have been used for many decades in several branches of the chemical and metallurgical industries. Some references concerning their applications can be found in the works of Shah *et al.* (1982), Deckwer (1992) and Kantarci *et al.* (2005). Bubble columns are not only used as central operation units but also for several product recovery processes such as separation by adsorption in bubble flows (Zlokarnik 1990). In spite of the mechanical simplicity that characterizes bubble columns which grant them with oper-

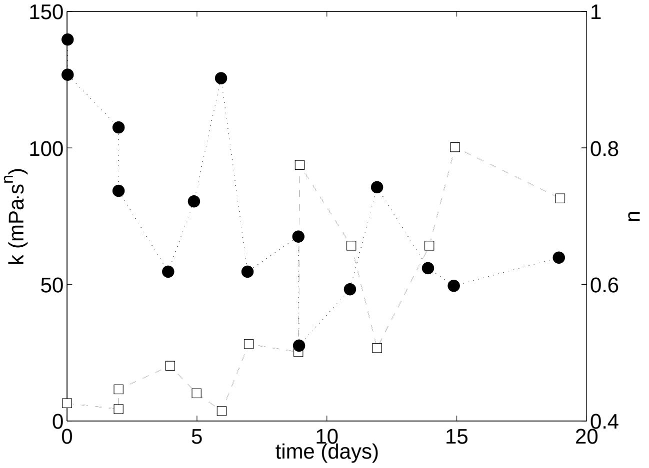

(a)

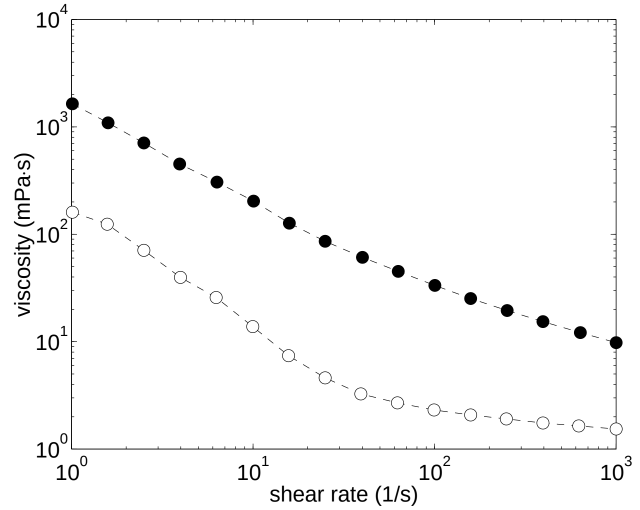

(b)

Figure 1.1: (a) Evolution of the flow index n (●) and consistency index k (□) of *B. vulgaris* cultures (plant cells used to produce food dyes) grown in shaken flasks and stirred tanks (Rodríguez-Mondory & Galindo 1999); (b) viscosity of activated sludges containing 2.7 (○) and 16 (●) g/L of suspended solids (Yang *et al.* 2009).

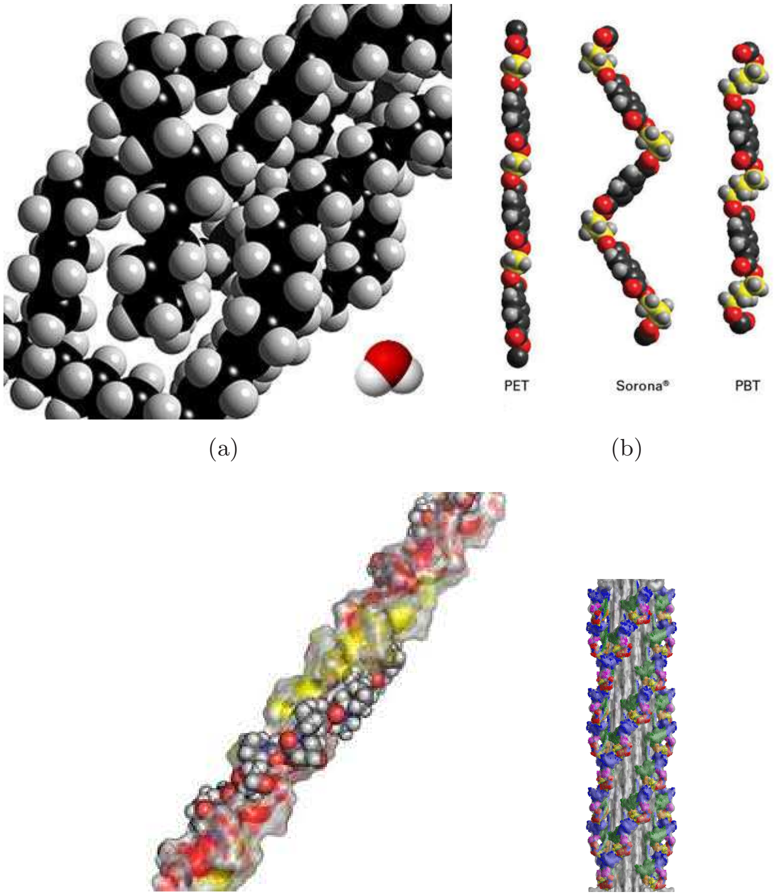

(a) (b)

(c) (d)

Figure 1.2: (a-c) Molecular structure of some polymers: (a) molecular backbone of a polyethylene chain, a molecule of water is put as reference; (b) molecular structure of PET (polyethylene terephthalate), PBT (polybutylene terephthalate) and a polymer developed by DuPont©, which has an intermediate structure in comparison with the other two; (c) molecular structure of collagen, the most abundant protein in mammals and which composes the connective tissue. (d) Structure of a myosin filament, an important component of the muscular tissue. The collagen and myosin structures can be found in *www.3dchem.com* and *www.pdbj.org/emnavi/* respectively.

ative and cost benefits (Kilonzo & Margaritis 2004), their basic engineering design is not a simple task. Given a certain chemical process and liquid phase properties, an engineer has to implement the optimum column geometry, sparger configuration and power input (superficial gas velocity U_g) to satisfy the uptake rate of the ongoing chemical reaction, in addition to achieving the optimum mixing and heat transfer properties between phases. Such estimations require the knowledge of functional relations among the central operational variables such as the mean bubble diameter $\overline{d}_b$, mean bubble velocity $\overline{U}_{SW}$ and gas fraction Φ_g. Some authors have also studied the development of the liquid velocity and its variance as a measure of the amount of agitation or *pseudo-turbulence* conferred by the dispersed phase (Van Wijngaarden 1998, Martínez-Mercado 2007). An example of the intricate relation among the variables of a bubble column can be seen in figure 1.3. Consider, for example, the variables involved in the value of the volumetric oxygen transfer coefficient, k_La. This coefficient is directly related with the rheology of the fluid because this affects the diffusive transport of oxygen or other gases through the bubble surface. k_La depends also on the available gas-liquid interfacial area found in the total volume of the liquid, which in turn depends on the size of the bubble and the gas fraction Φ_g. While the bubble size depends directly in the sparger type and gas velocity U_g, the gas fraction depends also on the superficial gas velocity, the bubble velocity (which again depends on the bubble size) and in the liquid circulation patterns, which are related with the flow regimes. To finish, the flow regimes depend on the gas velocity (see figure 1.4), the bubble size, the column diameter (see figure 1.5) and in the rheology of the fluid.

Due to this complex relation among the operational variables of the bubble columns, a large literature concerning bubble flows in Newtonian and non-Newtonian fluids exist seeking for a better understanding of the bubble columns performance. The reference to some of this works are included in the background section. Some general guidelines about the bubble columns are here mentioned:

- In the homogeneous regime the gas fraction Φ_g depends linearly on the gas velocity U_g for the cases when the mean velocity of the liquid is zero or there is no liquid circulation patterns; in such conditions the gas fraction can be estimated as $\Phi_g = U_g/\overline{U}_{SW}$.

- The heterogeneous regime is usually found when the gas velocity becomes higher than 2cm/s.

- The gas-liquid interfacial area per unit volume is calculated as $a = 6\Phi_g/\overline{d}_b$. Therefore, engineers usually prefer to produce small bubbles and inject large quantities of gas into the column in order to obtain large values of a.

- The usual way to control the circulation patterns of the liquid is by changing the inner geometry of the column. A simple way to do this is by introducing an inner tube into the column (figure 1.6a) or divide the column in different stages (figure 1.6b). The internal geometry of the columns also depends on the specific process. For example, packed columns (figure 1.6c) are frequently employed in the biotechnology industry because they offer a mechanical support to living cells (Kantarci *et al.* 2005).

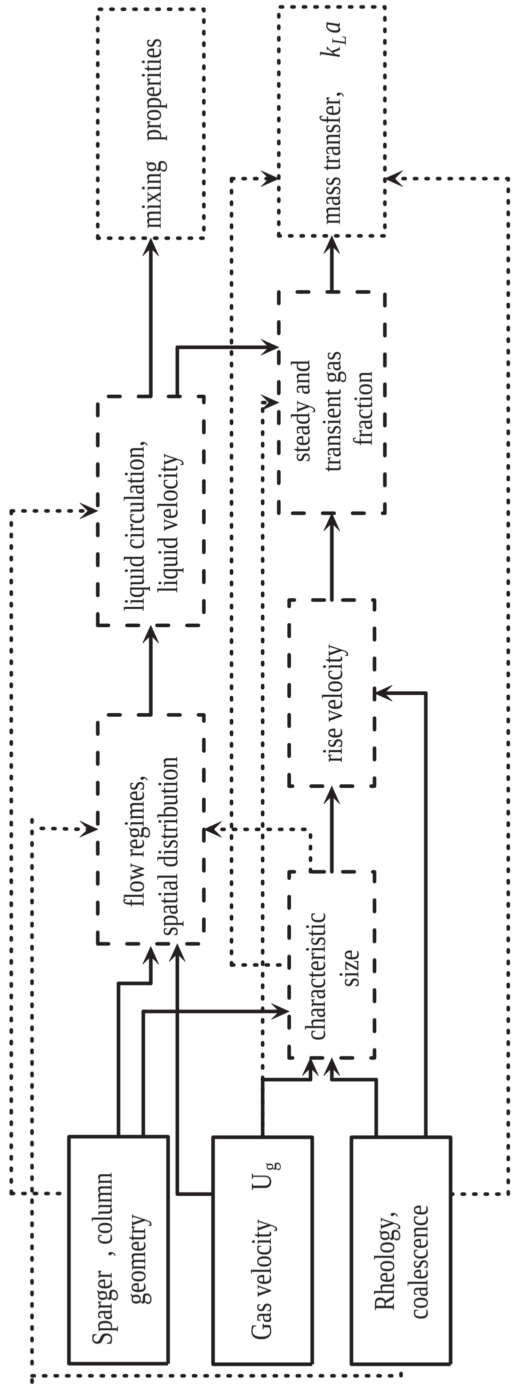

Figure 1.3: Diagram showing the relations among the variables of a bubble column (based in the work of Heijnen and Van't Riet 1984). The boxes with a (−) frame type represent the operational variables, the boxes with a (−−) frame type represent variables that are measured, boxes with (...) type represent variables that are calculated after using an appropriate model.

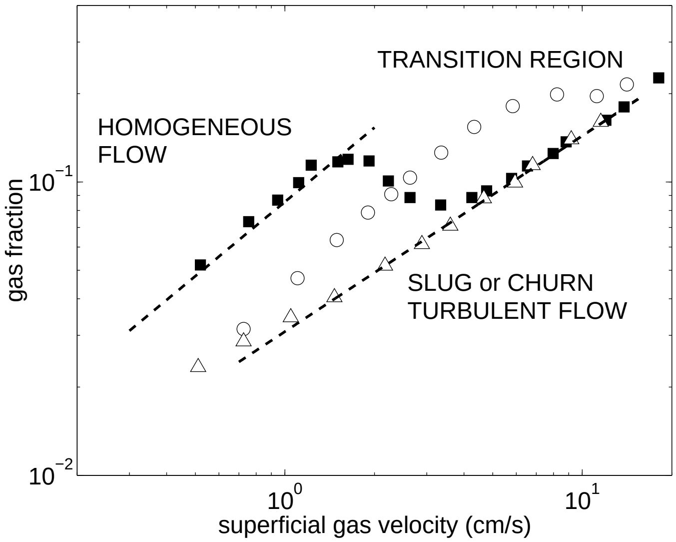

Figure 1.4: Flow regimes found in a bubble column filled with caboxymethyl celullose (CMC) solutions: (○) 0.0% CMC, (■) 1.0% CMC, (△) 1.8% CMC. The different regimes are separated by segmented lines. The homogeneous or bubbly flow regime is characterized by a nearly mono-dispersed bubble size; note that in this regime the gas fraction increase linearly with the gas velocity. The heterogeneous or transition regime is characterized by a multi-dispersed bubble size; in this case the gas fraction decreases due to bubble coalescence (the increase of the bubble size will reduce the retention time of the gas). When the gas velocity is large enough, the slug or churn turbulent regimes appear, depending on the column size. Note that for the 1.0% CMC solution the gas fraction in the homogeneous flow is larger than that in water. Data taken from the work of Schumpe & Deckwer (1982).

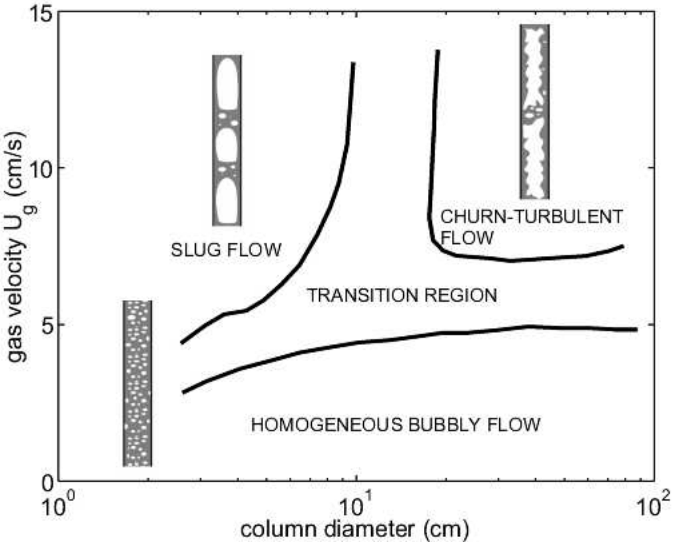

Figure 1.5: Map of the flow regimes as a function of the gas velocity and column diameter. After the transition region, the bubble flow can produce two regimes depending on the bubble size: if the column diameter is small, the bubbles will acquire a bullet shape and will occupy almost all the column diameter, this regime is called slug flow. In the churn-turbulent regime the distribution of the bubble size becomes very irregular in space and time, so the flow becomes oscillatory and the liquid near the tube wall is continually being pulsed up and down. Figure reproduced from the work of Shah *et al.* (1982).

- Processes run in batch or semibatch operations are more likely to experience an increase of viscosity, as is the case of an aerobic submerged culture.

As this work deals with the properties of bubble flows in non-Newtonian fluids from a standpoint of basic science, all the results presented here were obtained using the simplest bubble column geometry. The details are presented in the experimental setup.

1.4 Polymeric solutions

The bubble column geometry is not the only thing that was simplified in this study. Instead of using very complex fluids as the ones obtained in a fermentation process, the researchers usually employ model fluids for which the rheological behavior can be modeled and predicted and which can facilitate the interpretation of the results. These model liquids are usually composed by just one type of polymer dissolved in a good solvent. The term “good solvent” refers to a solvent that has a strong attractive energy with the functional groups of the polymer (Doi & Edwards 1986), allowing the stretching of the polymer chains. A Θ solvent, on the contrary, is a term used to refer to a solvent that has a poor interaction with the functional groups of the polymer. In this case the polymer chains form a compact body in which the interaction with the solvent are reduced to a minimum. From a pure mechanical standpoint (without getting into details of the molecular structure of the polymer), a polymeric solution can be represented by a special

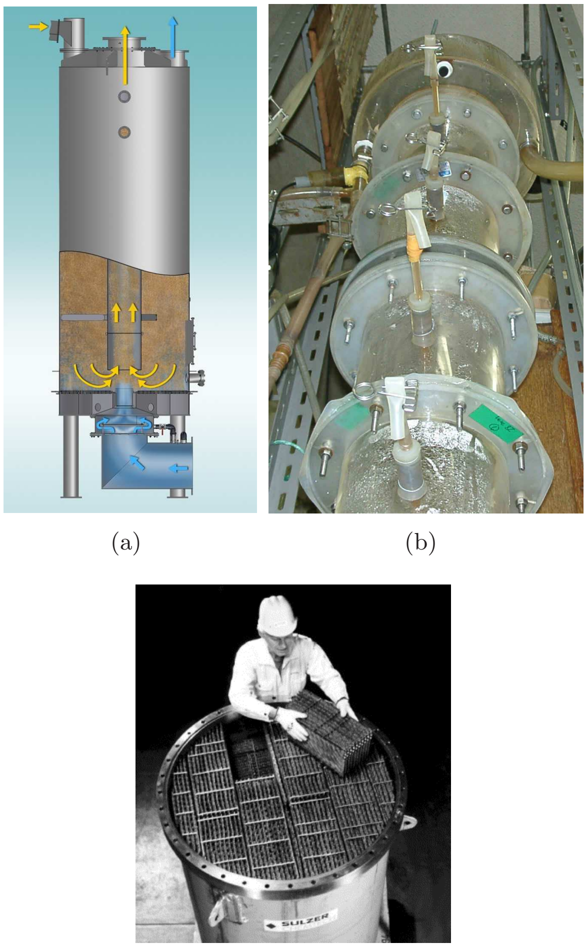

(a) (b)

(c)

Figure 1.6: Different bubble columns geometries: (a) airlift column, (b) a multistage column, (c) a packed column; this geometry has immobilized beds employed as a structured support for the catalyst (see Götze *et al.* 2001).

arrange of dashpots, which represent the viscosity of the fluid ($\tau = \eta\dot{\gamma}$, as in eq. 1.1), and springs, which represent the elastic properties of the fluid. This elastic behavior comes from the fact that certain polymer chains are flexible and tend to an equilibrium shape after stop exerting a small amount of deformation, as it happens with a rubber band. The restored force per unit area is thus equal to the force needed to deform the elastic part of the the polymer:

$$\tau = E\gamma \tag{1.3}$$

where γ is the deformation and E the elastic modulus. In the case of diluted and semidiluted polymer solutions, the elastic and viscous properties can be represented by a three-parameter viscous model (Mase 1970, Bird *et al.* 1987), shown in figure 1.7. A diluted polymer solution is characterized by having few polymer-polymer interactions, each polymer chain being separated from the other ones and occupying a volume with radius R_g. In a semidiluted polymer solution some polymer chains became closer and start overlapping with each other. The polymer concentration c^* in which the transition from the diluted to the semidiluted condition occurs can be approximated as (Doi & Edwards 1986):

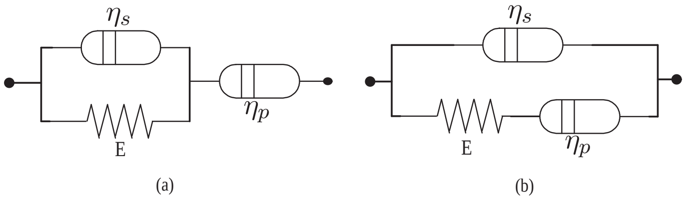

Figure 1.7: Three-parameter viscous model. E is the elastic modulus, η_s is the solvent contribution to the total viscosity, η_p is the polymer contribution to the total viscosity.

$$\frac{c^* N_A}{M_w} \simeq \frac{1}{(4/3)\pi R_g^3} \tag{1.4}$$

where the left hand-side of the equation represents the number of molecules per unit volume and the right hand-side the inverse of the volume occupied by a single polymer chain; N_A is the Avogadro's number and M_w is the molecular weight of the polymer. Lets consider, for example, the case of a polyacrylamide having a molecular weight of 5×10^6 g/mol (like the one used in this study); the critical concentration c^* in water will be 6.6% (using $R_g = 310nm$, see Mark 1999). In a 0.1M NaCl solution this number will be greatly reduced (0.013%, $R_g = 2477nm$) due to the interactions with the salt.

The spring and dashpot arrangements shown in figure 1.7 represent an elastic response of the liquid being delayed by the solvent viscosity η_s. Let us analyze first the figure on the left. This arrange is composed by a dashpot η_p put in series with a Kelvin-Voigt unit in which the total stress is given by the sum of the stress applied in the spring and in the dashpot η_s:

$$\tau = E\gamma_{K-V} + \eta_s\dot{\gamma}_{K-V} \tag{1.5}$$

As the total deformation is given by the sum of the deformation in the K-V unit and the deformation in the dashpot η_p, i.e. $\gamma = \gamma_{K-V} + \gamma_{dashpot}$, equation 1.5 can be written in terms of the total deformation and its time derivatives:

$$\frac{d\tau}{dt} = E\dot{\gamma} - \frac{E}{\eta_p}\tau + \eta_s\frac{d\dot{\gamma}}{dt} - \frac{\eta_s}{\eta p}\frac{d\tau}{dt} \tag{1.6}$$

multiplying by η_p/E and grouping the different terms, we get the following expression:

$$\tau + \lambda_1\frac{d\tau}{dt} = \eta_p\left(\dot{\gamma} + \lambda_2\frac{d\dot{\gamma}}{dt}\right) \tag{1.7}$$

where $\lambda_1 = (\eta_p + \eta_s)/E$ and $\lambda_2 = \eta_s/E$. In the case of the figure placed on the right, we can see that the total stress is the sum of the stress in the dashpot η_s and the stress in the Maxwell unit:

$$\tau = \eta_s\dot{\gamma} + \tau_{Maxwell} \tag{1.8}$$

The stress in the Maxwell unit can be known using the fact that the total deformation is equal to the sum of the deformation in the spring and in the dashpot η_p, i.e. $\gamma = \gamma_s + \gamma_d$ (which is equal to the deformation experienced by the dashpot η_s). Using the basic equations of the spring and the dashpot and the time derivatives of the deformation, it turns out that the Maxwell stress is equal to:

$$\tau_p + \lambda_1\frac{d\tau_p}{dt} = \eta_p\dot{\gamma} \tag{1.9}$$

where $\lambda_1 = \eta_p/E$. Hence, the Maxwell stress is related to the polymer stress τ_p. The arrangement shown in figure 1.7b allows us to calculate the total stress using two distinct stresses, one related to the solvent, $\tau_s = \eta_s\dot{\gamma}$, and the other related to the stress τ_p (eq. 1.9). Considering that $\tau = \tau_s + \tau_p$ or $\tau_p = \tau - \eta_s\dot{\gamma}$, and that $\eta = \eta_s + \eta_p$, equation 1.9 can be expressed in terms of the total stress:

$$\tau + \lambda_1\frac{d\tau}{dt} = \eta\left(\dot{\gamma} + \lambda_2\frac{d\dot{\gamma}}{dt}\right) \tag{1.10}$$

where λ_2 is now equal to $\lambda_1(\eta_s/\eta)$. We can see that the two arrangements shown in figure 1.7 lead to the same mathematical expression. On the other hand, with the second arrangement we have the advantage that the total stress can be decouple into the solvent and polymer stresses. Equation 1.10 is known as the Jeffrey's model and it was originally proposed to study the propagation of waves in the earth's mantle (Bird *et al.* 1987). The rheologist noted that the Jeffrey's model is not independent from the particular coordinate choice. One way to make it invariant frame is by introducing the upper convected derivative defined as:

$$\overset{\nabla}{\underline{\underline{A}}} = \frac{\partial\underline{\underline{A}}}{\partial t} + \underline{v}\cdot\nabla\underline{\underline{A}} - \underline{\underline{A}}\cdot(\nabla\underline{v}) - (\nabla\underline{v})^T\underline{\underline{A}} \tag{1.11}$$

Equation 1.10 can be thus expressed as:

$$\underline{\underline{\tau}} + \lambda_1\overset{\nabla}{\underline{\underline{\tau}}} = \eta\left(\underline{\underline{\dot{\gamma}}} + \lambda_2\overset{\nabla}{\underline{\underline{\dot{\gamma}}}}\right) \tag{1.12}$$

and is known as the Olroyd-B model, which, unlike the Jeffrey's model, is a nonlinear differential equation due to the appearance of the velocity and its gradients in the convected derivative. This equation can also be deduced using the kinetic theory, in particular, employing the so called "elastic dumbbell model" (Bird *et al.* 1987). The double line format $\underline{\underline{A}}$ depicts a tensor of second order.

Note that the Olroyd-B model only takes into account the elastic property of the fluid (contained in the relaxation time λ_1) and a constant viscosity. Therefore, it cannot predict any thinning behavior. The variation of the viscosity with the shear rate is some how easy to explain and modeled (using, for example, the empirical equation 1.2), but requires certain structural information of the material or other sort of mathematical considerations (besides picturing a collection of springs and dashpots) in order to be included in a constitutive equation based not only on empirical reasons. One could be tempted to introduce equation 1.2, for example, into equation 1.12, and get both behaves using a single model. This cannot be done, however, because we have split the total viscosity into η_s and η_p and we ignore how they vary with the shear rate. This can be done only if $\lambda_2 = 0$ (returning to the Maxwell model); the resulting equation is called the "White-Metzner" model. Other models, which take into account some particularities of the structure of the material, can predict the thinning and elastic behavior; for example, the FENE (finitely extensible nonlinear elastic connector) model (Bird *et al.* 1987), the Phan-Thien-Tanner model, based on network theory (Phan-Thien & Tanner 1977) and the Bautista-Manero-Puig model (BMP-Model, Bautista *et al.* 1999), which includes a kinetic equation of the material structure. Other mathematical expressions such as the Oldroyd-8-constant model or the third-order fluid equation can also predict a viscoelastic behavior with variable viscosity in some limited conditions (Bird *et al.* 1987). The use and test of these models in the present study would require time and it would distract us from the main theme of this work. Therefore, the power law (eq. 1.2) and the Oldroyd-B (eq. 1.12) models were the only ones considered in this work, specially when the numerical results were compared with experiments.

1.4.1 How polymeric solutions are studied: shear versus extensional flows

Many studies have considered flows submitted to simple shear deformation (the shear rate $\underline{\underline{\dot{\gamma}}}$ tensor only has non-zero values in the off-diagonal positions). The notion that we have about the viscosity arises from considering a pure shear flow. This shear viscosity is easy to measure if a sample of the test fluid is placed between two parallel disks (or using a cone-plate geometry) and one of them is rotated. The amount of stress necessary to keep the disk moving at a certain steady shear rate value is measured by a device call rheometer. The resulting viscosity value is a very important datum even for the case of a spherical body (like a bubble) moving through a liquid. However, the flow around a spherical body is far from pure shear; it is close to pure shear near the equator but will be lower as we move to the poles. In the case of a bubble rising in a liquid, the flow formed behind the south pole is extensional. Frederick T. Trouton was the first one to note that the ratio of the extensional viscosity with the shear viscosity for Newtonian fluids is three, which is a necessary consequence of an incompressible material submitted to extensional flow (strong stretch in one direction and two equal contractions in the other two directions, see Morrison 2001 or Petrie 2006). This ratio is higher than three in the case of polymeric solutions due to the stretching capacity of the polymer chains in the flow direction and will thus affect the fluid flow that will appear behind the bubble or other spherical bodies. Note also that the extensional flow needs its own relaxation time since the time λ_1 defined in eq. 1.12 uses the shear viscosity contribution of the polymer. In general, the measurements of the extensional properties of a material, such as the extensional viscosity and the extensional relaxation time, are more difficult to carry out than the measurements of the shear properties because, unlike the latter ones, where the geometry of the sample do not change, in an extensional flow the geometry of the sample do change with time (like the decrease of the diameter of a liquid thread placed between two plates moving away from each other). Therefore, the extensional rate in this kind of devices (for more information see Macosko 1994 or Stelter *et al.* 2000) is not steady, unlike the one achieved in a conventional rheometer. Due to the relevance of extensional deformation in the flow of polymeric solutions around rounded objects, in the discussion of the semidiluted Boger fluid (see section 7.1.1) some extensional data taken from other work (Stelter *et al.* 2000) has been included.

In addition to the common shear test that is done to measure the viscosity of a fluid at a steady shear rate (the value of the deformation γ is large), there is another test that is often used to know which of the behaviors, elastic or viscous, is dominant. This test is done at small deformations such that the stress can be described as a linear function of the strain; the deformation is thus exerted in an oscillatory way. The resulting stress will also oscillate at the same frequency w but will be shifted by a phase angle δ with respect to the strain wave (Macosko 1994, Morrison 2001):

$$\tau = \tau_0 \sin(wt + \delta) \tag{1.13}$$

(the strain is equal to $\gamma = \gamma_0 \sin(wt)$, where the subscript '0' refers to the maximum deformation applied by the rheometer). After using a trigonometric identity we obtain:

$$\tau = G'\gamma_0 \sin(wt) + G"\gamma_0 \cos(wt) \tag{1.14}$$

where $G' = (\tau_0 \cos\delta/\gamma_0)$ is the parameter which is in phase with the strain (storage modulus, related with the elastic behavior) and $G'' = (\tau_0 \sin\delta/\gamma_0)$ is the parameter which is in phase with the strain rate (loss modulus, related with the viscous behavior). When $0 < \delta < \pi/2$ the stress τ will not be in phase with either the strain or the strain rate. The G' and G'' moduli, when plotted in terms of the frequency w, give us an idea of which behavior is dominant for a certain frequency range (see section 5.2).

1.5 Some useful dimensionless numbers

Much of the discussion appearing in this study employs several dimensionless numbers that group some relevant parameters of the bubble flows. Leaving apart the bubble-bubble and bubble-wall interactions, the resistance force exerted on a deformable bubble rising through a fluid by means of the buoyancy force can be expressed as:

$$F = \phi(\rho, \eta, U, d_b, \sigma, g) \tag{1.15}$$

where the force F is a function of the liquid density ρ, the liquid viscosity η, the bubble velocity U, the bubble diameter d_b, the surface tension σ and the gravity g. The Π-Buckingham theorem state that an equation containing n dimensional variables can be expressed by an equivalent equation containing $n-k$ dimensionless numbers, where k is the number of dimensionally independent physical quantities. In our case, $n = 7$ (including the force F) and $k = 3$ (units of weight, distance and time); hence, the dimensionless equation will have 4 dimensionless numbers (including that for the force). If we choose ρ, U and d_b as the fluid, kinematic and geometric fixed variables, we will obtain:

$$\frac{F}{\rho U^2 d_b^2} = f\left(Re, We, Fr\right) \tag{1.16}$$

where the Reynolds, Weber and Froude numbers are defined as:

$$Re = \frac{\rho U d_b}{\eta} = \text{inertia forces/viscous forces} \tag{1.17}$$

$$We = \frac{\rho U^2 d_b}{\sigma} = \text{inertia forces/superficial forces} \tag{1.18}$$

$$Fr = \frac{U^2}{g d_b} = \text{inertia forces/gravity forces} \tag{1.19}$$

Choosing now ρ, g and d_b as the fixed variables we obtain:

$$\frac{F}{\rho g d_b^3} = f\left(Eo, \frac{1}{\sqrt{Fr}}, \frac{\rho\sqrt{g} d_b^{3/2}}{\eta}\right) \tag{1.20}$$

where:

$$Eo = \frac{\rho g d_b^2}{\sigma} = \text{buoyancy forces/superficial forces} \tag{1.21}$$

Eo is called the Eötvös number (or Bond number if the radius of the bubble is chosen instead of its diameter). If we choose the following combination: η, g and σ, we now obtain:

$$\frac{\eta^2 F g}{\sigma^3} = f\left(Mo, \frac{1}{Ca}, \frac{\sigma^2}{\eta^2 d_b g}\right) \tag{1.22}$$

where:

$$Mo = \frac{\eta^4 g}{\rho \sigma^3} \tag{1.23}$$

$$Ca = \frac{\eta U}{\sigma} = \text{viscous forces/superficial forces} \tag{1.24}$$

The Morton number, Mo, can be understood as a collection of the physical properties of the fluids. This number, as well as the Capillary number, Ca, can be obtained combining other dimensionless numbers, for example, $Mo = We^3/(Fr Re^4)$, $Ca = We/Re$. If a function of the rise velocity U in terms of the bubble diameter is given, like $U = \sqrt{g d_b}$ (Smolianski *et al.* 2008), the Morton number becomes a function of the Eötvös and Reynolds numbers: $Mo = Eo^3/Re^4$. Other dimensionless numbers can appear if additional variables are included. For instance, if we consider the relaxation time λ_1 due to the elastic properties of the fluid, the common dimensionless number use in regard is $De = 2\lambda_1 U/d_b$, called the Deborah number[1]. If surface tension gradients appear in the bubble surface due to the presence of some molecules with surface activity, the Marangoni number $Ma = 2\Delta\sigma/d_b\tau$ (τ is the shear stress) is commonly used (Rodrigue & DeKee 2002).

1.6 Forces acting on a bubble

This work studies bubble swarms rising in non-Newtonian fluids. However, one can realize (and need) that much of the comprehension regarding the behavior of bubble swarms can be obtained by analyzing a small group of bubbles. Actually, one may deduce the behavior of many-bodies interactions by analyzing the interaction of just two bodies (Manga & Stone 1995). This is the reason why in this work the study of the interaction of two bubbles was also done. Therefore, before studying bubble swarms, one needs to have a good understanding of the forces acting on a single body.

In the case of a bubble formed by injecting gas through a needle with diameter d_{cap}, the buoyancy and surface forces can be equated to estimate the diameter of the bubble:

$$d_b = 2\left(\frac{3}{4}\frac{d_{cap}\sigma}{\rho g}\right)^{1/3} \tag{1.25}$$

When the bubble rises freely through the liquid, the forces acting on the bubble can be sketched as in figure 1.8 (Dijkhuizen *et al.* 2010). In the steady state

$$\overrightarrow{F_B} - \overrightarrow{F_D} - \overrightarrow{F_L} = 0 \tag{1.26}$$

where $\overrightarrow{F_B}$, $\overrightarrow{F_D}$ and $\overrightarrow{F_L}$ are the buoyancy, drag and lift forces.

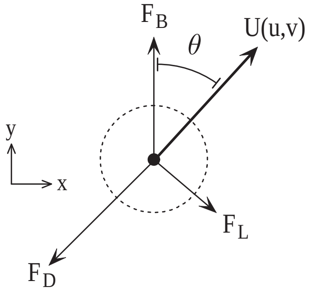

Figure 1.8: Forces acting on a single bubble rising with velocity U.

As the drag and lift forces have a direction perpendicular to each other, they can be easily separated. For the case of the drag force we have that:

$$\frac{4}{3}\pi\rho g(d_b/2)^3\cos\theta = \frac{1}{2}C_d\pi\rho(d_b/2)^2|U|^2 \tag{1.27}$$

---

[1] The reason of calling the $2\lambda U/d_b$ relation the "Deborah" number has an interesting relation with a tale that appears in the Bible, see Macosko (1994) or read Judges 5:4-5.

where the left hand-side of the equation denotes the buoyancy force and the right hand-side the drag force, C_d is the drag coefficient. From this equation we can obtain the value of C_d:

$$Cd = \frac{4d_b g}{3|U|^2}\cos\theta = \frac{4d_b g U_y}{3|U|^3} \tag{1.28}$$

Note that if the lateral velocity is zero ($U_x = 0$), then C_d is:

$$C_d = \frac{4}{3}\frac{d_b g}{U^2} \tag{1.29}$$

For the lift force we have:

$$\frac{4}{3}\pi\rho g(d_b/2)^3(-\sin\theta) = \frac{4}{3}C_L\pi(d_b/2)^3\frac{\partial U_y}{\partial x}|U| \tag{1.30}$$

where the left hand-side of the equation is the buoyancy force and the right hand-side the lift force (C_L is the lift coefficient). Note that the lift force arises when there is an horizontal gradient of the vertical velocity, the same which can be produced by the movement of the surrounding liquid or by the passage of other bubbles. From eq. 1.30 we can obtain the lift coefficient:

$$C_L = -\frac{g\sin\theta}{\frac{\partial U_y}{\partial x}|U|} = -\frac{gU_x}{\frac{\partial U_y}{\partial x}|U|^2} \tag{1.31}$$

Other forces can also act on the bubble when an accelerated motion occurs such as the added mass and the Basset forces (Zhang & Fan 2003). In this study such forces were not considered for the sake of simplicity (and are not needed when direct numerical simulations are used) and actually become practically untractable (in the mathematical sense) in bubble swarms.

1.6.1 Which additional forces can appear in non-Newtonian flows?

In the case of the thinning fluids with no elasticity, we may think that this property will not introduce additional forces in the flow field since such fluids can be considered generalized Newtonian fluids. However, we will see that the viscosity gradients generated in the thinning fluids can change the general behavior seen in Newtonian flows (see section 6.2.3). In contrast with the thinning fluids case, liquids having elastic properties (with or without thinning behavior) will generate additional forces that will actually oppose the inertial ones. The inclusion of such force can be seen by setting a simple experiment consisting in a container filled with the fluid and in which a rod is placed and rotated in the center (see figure 1.9, Bird *et al.* 1987). We can obtain an equation to identify the pressure profile in a particular direction by using the equation of motion in steady state and using cylindrical coordinates. The profile of the normal pressure ($\tau_{zz} + p$) exerted on the liquid surface can thus be expressed as:

$$\frac{d(\tau_{zz} + p)}{d\ln r} = 2\tau_{r\theta}\frac{d}{d\tau_{r\theta}}(\tau_{rr} - \tau_{zz}) + (\tau_{\theta\theta} - \tau_{rr}) + \rho U_\theta^2 \tag{1.32}$$

where τ_{ab} indicates the stress value placed in the *a-plane* having a *b-direction* and p is

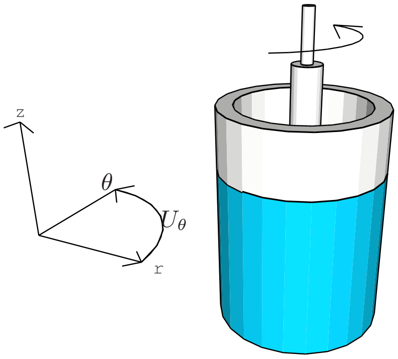

Figure 1.9: A rod rotating inside a cylinder

the hydrostatic pressure. In Newtonian fluids, which are characterized by an isotropic microstructure regardless the value of the shear rate, all the normal stress differences, such as $\tau_{\theta\theta} - \tau_{rr}$ (N_1) or $\tau_{rr} - \tau_{zz}$ (N_2) will be zero. Therefore, the normal pressure $\tau_{zz} + p$ will increase with the radius, as ρU_θ^2 has a positive value. In this case the normal pressure will produce a slight rise of the fluid near the cylinder wall, as is commonly observed. In the case of a polymer solution, the flow field will cause the stretching of the polymer chains in the direction of the flow which ultimately leads to the appearance of an anisotropic microstructure. As the polymer chains will tend to return to its original shape, they will generate restoring forces that are anisotropic in nature (Barnes *et al.* 1989). This is the origin of the normal stress differences. In general, the first normal stress difference $\tau_{\theta\theta} - \tau_{rr}$ ($\tau_{11} - \tau_{22}$) is negative and much larger than the second difference $\tau_{rr} - \tau_{zz}$ ($\tau_{22} - \tau_{33}$); hence, in this case the normal pressure will increase as the radius decreases depending on the magnitude of N_1. This effect will produce a rise of the fluid in the rod, contrary of what is seen in the Newtonian fluids[2]. There are other interesting effects produced by the normal forces reported in the literature. For instance, Joseph & Feng (1996) noted that the normal forces acting on a solid body in plane flows are compressive in nature and will tend to join two separated bodies in the perpendicular direction of the flow. The first normal stress difference N_1 can be measured in a rheometer using a cone-plate geometry (Morrison 2001).

1.7 A note on flows at low Reynolds numbers

The average value of the Reynolds number obtained in this work for all the experimental cases was about seven, with a maximum of 40 and a minimum of 0.0001. For Re of O(10) the inertial forces are larger than the viscous ones but the latter still play an important role in the fluid flow. In the limit of $Re \rightarrow 0$, the flow around a rising bubble is caused solely by viscous stresses. The streamlines representing the motion of the fluid in this limit can be described by the stream function Ψ (Batchelor 1991):

---

[2] This phenomenon is called the rod-climbing effect or Weissenberg effect, after Karl Weissenberg, who originally studied this phenomenon (Bird *et al.* 1987).

$$\Psi = Ur^2 \sin^2\theta \left(\frac{3}{4}\frac{a}{r} - \frac{1}{4}\frac{a^3}{r^3} \right) \tag{1.33}$$

where a is the bubble radius and r is the radial distance from the bubble center (spherical coordinates are considered and symmetry in the $\phi - direction$). In the creeping flow regime ($Re \rightarrow 0$), the drag coefficient is $C_d = 24/Re$ if the bubble has a no-slip condition at the surface (Stokes prediction), and $C_d = 16/Re$ if the bubble has a free surface condition (Hadamard prediction). On the other hand, in the limit of $Re \rightarrow \infty$, there is no transmission of the motion by molecular contacts; the flow will be cause solely by body forces (as gravity) or pressure gradients. It can be shown that $C_d = 0$ for a potential flow around a sphere (D'Alambert's paradox). The streamlines representing the motion of the fluid around a spherical body will be now described by the stream function (Currie 1974, Batchelor 1991):

$$\Psi = \frac{1}{2}Ua^3\frac{\sin^2\theta}{r} \tag{1.34}$$

It is instructive to calculate how the velocity decays with the distance r in both, creeping and potential flows. For this, we can use two equations for the r and θ velocities which automatically satisfy the continuity equation:

$$U_r = \frac{1}{r^2 \sin\theta}\frac{\partial\Psi}{\partial\theta}, U_\theta = -\frac{1}{r\sin\theta}\frac{\partial\Psi}{\partial r} \tag{1.35}$$

For the creeping flow case we obtain that U_r, $U_\theta \propto r^{-1}$ for $r >> a$ ([3]). In the case of the potential flow we obtain that U_r, $U_\theta \propto r^{-3}$. Hence, we observe that the decay of the liquid velocity is much smaller for low Re flows than in the high Re ones. We can expect then that the movement of a single bubble at low Re numbers will be "felt" by another bubble some diameters apart from it. In the following, the term "long range interactions" will be used to refer to this effect, in contrast with the "short range interactions" that are seen in high Re flows.

---

[3] If the Oseen's equation is used instead we will obtain that $U_r \propto r^{-2}$ outside the Oseen wake and U_r, $U_\theta \propto r^{-1}$ within the Oseen wake.

Chapter 2

Background

In this chapter some of the studies that have been conducted on single, pair and bubble swarms in non-Newtonian flows will be presented. Although the text is mainly focused on viscoelastic fluids, some of the works that have been done in Newtonian fluids will be discussed in order to understand the similarities and differences between these flows and the non-Newtonian ones. The text also includes some references about sedimentation of particles. This is done for two reasons: there is a lot of literature concerning this issue, and secondly, its phenomenological behavior is similar to that observed in rising bubbles, the main differences being, of course, the density differences between the disperse and continuous phases and the degree of surface deformation. The reader will note that although there are some important studies about bubble swarms rising in non-Newtonian fluids, the information is still scarce and a clear explanation of the separate contributions of the thinning and elastic parts of the fluid is not yet available.

2.1 Single bubbles

The study of single bubbles rising in viscoelastic fluids constitute, together with the study of sedimentation of spheres, an important area of research in polymeric flows and are the first step towards the understanding of multiphase flow systems in non-Newtonian fluids (Chhabra 1993). Perhaps the most fascinating effects seen in single bubbles rising in viscoelastic fluids are the formation of a negative wake (the liquid moves contrary to the bubble direction) at some distance from the bubble's back and the discontinuity seen in the volume-velocity relation of the bubble. Several studies, beginning with the seminal work of Astarita & Apuzzo (1965), were devoted to the investigation of the origin of these two phenomena (Acharya *et al.* 1977, Liu *et al.* 1995, Rodrigue & De Kee 2002, Herrera-Velarde *et al.* 2003, Dou & Phan-Thien 2004, Kemiha *et al.* 2006, Soto *et al.* 2006, Pilz & Brenn 2007, Pillapakkam *et al.* 2007, Lind & Phillips 2010).

There has been two main hypotheses regarding the origin of the velocity jump. The first one, which we can call the surface-active agents mechanism, claims that the jump is triggered by a sudden liberation of polymer molecules (or other molecules with surface activity) from the bubble surface (Rodrigue *et al.* 1998, Rodrigue & DeKee 2002). Therefore, this mechanism propose a change on the bubbles surface: from a rigid to a stress-free

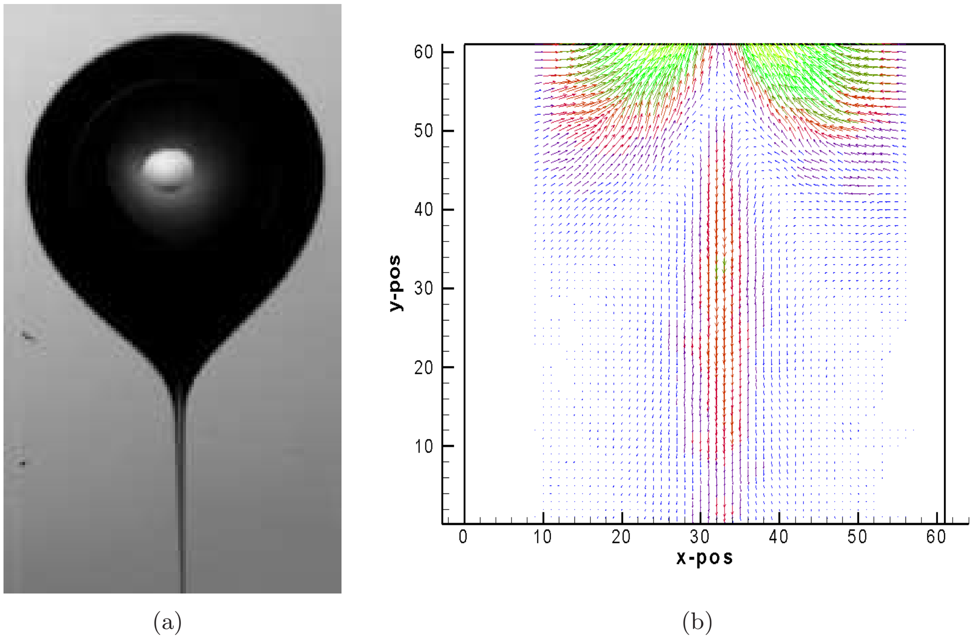

(a)

(b)

Figure 2.1: A bubble rising in a concentrated polymer solution (HASE); (a) picture of a bubble in which a long tail is formed behind (taken from Soto *et al.* 2006); (b) velocity map of the flow left by a bubble rising in the same fluid, the capture of the liquid motion was done using the particle image velocimetry technique. In this picture the negative wake is constituted by a fluid field (more precisely, a vector map) having an inverted cone shape whose direction is downwards and which is located in the center behind the bubble.

or slip condition. The fact that solid particles do not present a velocity jump (Acharya *et al.* 1977, although they present a negative wake) supports this hypothesis. The second explanation for the velocity jump, the hydrodynamic mechanism, proposes that the jump is produced by the formation of the negative wake (Herrera-Velarde *et al.* 2003, Pillapakkam *et al.* 2007, Lind & Phillips 2010) which in turn causes an action-reaction effect on the bubble velocity. This explanation took importance since it was observed that the velocity jump occurs at the same bubble volume in which the negative wake appears (Herrera-Velarde *et al.* 2003). The thinning properties of the fluid additionally contribute to the magnitude of the velocity jump $H = U_{after}/U_{before}$, where U is the terminal velocity of the bubble before and after the velocity jump, respectively (Rodrigue & De Kee 2002). The velocity jump discontinuity and negative wake seen in viscoelastic fluids have also been related with the formation of a sharp cusped end on the bubble surface since the three phenomena appear at the same value of the bubble volume (or critical volume V_{crit}, Liu *et al.* 1995, Herrera-Velarde *et al.* 2003, Soto *et al.* 2006, see figure 2.1).

The origin of the negative wake has been attributed to the extensional properties of the fluid (Dou & Phan-Thien 2004, Mendoza-Fuentes *et al.* 2009). In this regard, fluids that have a fast elastic response (low values of the ratio of the extensional and shear viscosity) are more prone to form a negative wake. We can get a mental picture of this process by imagining stretching a rubber band. If the rubber is somewhat stiff, we will need to apply a high force to deform it; as soon as we stop applying the extensional force, the rubber band will return to its original shape very fast (in the polymer solution this will originate an inversion point in the flow where the fluid will tend to return to its original position). On the contrary, if the rubber is soft, we will need less force to deform it; when we stop applying the force, the rubber band will slowly return to its original shape (the appearance of a negative wake in the polymer solution may not occur). Dou & Phan-Thien (2004) proposed the following condition to the appearance of a negative wake:

$$\frac{\partial \eta_{ext}}{\partial \dot{\epsilon}} / \eta_{ext} - \frac{1}{\dot{\epsilon}} \backsim \text{small values} \tag{2.1}$$

where η_{ext} is the extensional viscosity and $\dot{\epsilon}$ the rate of extensional deformation. Mendoza-Fuentes *et al.* (2009) reported that this condition applies for settling particles in associative polymers (the value of the above relation actually acquires values below zero when the negative wake appears). There has been a discussion, as mentioned above, whether the negative wake formation is a necessary condition or not for the velocity jump to occur.

Regarding the thinning behavior, the study of single bubbles has mainly been done in order to compare experimental results with theoretical or numerical simulations or to test numerical algorithms (Hirose & Moo-Young 1969, Bhavaraju *et al.* 1978a, Rodrigue *et al.* 1999a, Dhole *et al.* 2007, Radl *et al.* 2007, Zhang *et al.* 2010). However, as far as we now, only Zhang *et al.* (2010) have compared a dynamic parameter (Reynolds number) between their experimental and numerical results. The agreement that they found is reasonable although the deviation between the experimental and numerical results tend to increase with the thinning behavior (decreasing the flow index n). In general, one may think that a bubble rising in a thinning fluid will reach a higher velocity than that attained in a Newtonian fluid at the same conditions. However, this can be intuitively wrong and the comparison depends on which physical parameters are kept equal in both, the thinning and its Newtonian counterpart. In chapter 4 this issue will be discussed.

Another interesting fluids, which were not treated in this work, are the Bingham fluids. These fluids are characterized for presenting an initial resistance to move when an external force is applied. When this initial resistance, or yield stress, is surpassed, the fluid starts moving as a Newtonian fluid. This particular feature offers some experimental and numerical challenges. For example, when dealing with the mathematical expression of a Bingham fluid, which is not a continuous function due to the presence of a critical point that separates the unyielded and yielded behavior, or when exploring the conditions when the bubble is trapped (immobilized) by the fluid (Singh & Denn 2008, Tsamopoulos *et al.* 2008). The shape of a bubble rising in this type of fluids can also acquired a prolate shape and other particular shapes due to the relative movement of the unyielded and yielded regions surrounding the bubble (Singh & Denn 2008). In Newtonian and thinning fluids the bubble shape is generally spherical (for small bubbles) or ellipsoidal (oblate, for large bubbles).

2.2 Bubble pairs

2.2.1 Newtonian fluids

The study of the interaction of two bubbles was initially motivated by the coalescence phenomena due to its impact in the bubble columns efficiency. That was how researchers took two different paths concerning this issue: one was the study of the coalescence mechanism itself, which is highly dependent on the liquid composition (Lessard & Ziemiski 1971, Tse *et al.* 2003, Liao & Lucas 2010); the other was the study of the trajectories that two bubbles take before coalescence (Crabtree & Bridgwater 1971, Katz & Meneveau 1996, Sanada *et al.* 2009), which is the main subject of the present work.

For the case of creeping flow, Stimson & Jeffery (1926) analytically predicted the velocity of two spheres moving in-line in terms of the separation distance between them. As widely described by Happel & Brenner (1991), two bodies moving in this way in the creeping flow regime acquire a higher velocity than that attained by a single body; the velocity increases as the separation distance decreases. As the flow field does not have inertia, the bodies keep their distance without approaching each other. This trend is in agreement with experimental data (Happel & Pfeffer 1960) and with other analytical expressions (Happel & Brenner 1991) and applies to both, settling particles and rising bubbles.

When the inertia is small but finite ($Re \sim 0.25$) the vorticity around a spherical body looses its fore-aft symmetry and the trailing body acquires a higher velocity than the leading one, reaching the latter after some time. Crabtree and Bridgwater (1971) were the first ones to approximate the trailing bubble velocity as the sum of the terminal velocity of the single bubble plus its wake velocity at the distance where the trailing bubble is found. This hypothesis was referred to as a 'superposition principle' by Bhaga and Weber (1980). In later works (Narayanan *et al.* 1974, Bhaga & Weber 1980, Zhang & Fan 2003) this hypothesis was tested and confirmed for two in-line bubbles rising with Reynolds numbers up to $O(100)$. Crabtree and Bridgwater also reported the curious phenomenon (not fully explained yet) in which the trailing bubble experiences a significant deformation (from oblate to prolate form) moments before touching the leading one. Such deformation was also reported and photographed by Narayanan *et al.* (1974). These last authors worked with different bubble sizes producing basically two different wake structures: one forming a thin trailing wake and the other forming a wake with a stable toroidal vortex. For the former it was observed that the Stimson and Jeffery's equation described well the rise velocities of the trailing bubbles even though it was formulated for creeping flows and spherical bodies. For the second case, a superposition principle similar to the one proposed by Crabtree & Bridgwater was used. Bhaga and Weber also worked with bubbles forming a wake with a toroidal vortex (Reynolds≈ 80, Eötvös≈ 70). The experimental measurements of the wake velocity were in agreement with the velocity calculated using the superposition principle. Manga and Stone (1993, 1995) studied the effects of bubble deformability in the interactions among them. They found that bubble alignment and coalescence is enhanced when the buoyancy forces are much larger than the restoring forces produced by the interfacial tension on the bubble surface.

The interaction of two bubbles rising in potential flow was the subject of the theoretical work of van Wijngaarden and coworkers (vanWijngaarden 1976, Biesheuvel & vanWijngaarden 1982, Kok 1993a). In these papers it was found that two bubbles rising in potential flow experience an attractive force if their angle of approach lies within $\pm 54^\circ$ from the horizontal, but feel a repulsion otherwise. The attractive force is due to the low pressure zone formed between the bubbles since the liquid velocity in this zone is larger. On the other hand, the repulsive force felt by the bubbles when they are aligned close to the vertical arrangement is due to the dynamic pressure that one bubble exerts on the other.

The behavior predicted in potential flows contrasts greatly with that observed in viscous dominated flows (Vasseur & Cox 1977, Happel & Pfeffer 1960, Legendre *et al.* 2003). In such flows the behavior is actually the opposite: bubbles will experience a repulsive force if they lie near the horizontal alignment and an attraction if they lie close the vertical one. Such behavior can be explained in terms of the vorticity distribution: the vortices around each bubble will interact and repel each other if they are aligned horizontally. This applies as well if a bubble rises near a vertical wall (Vasseur & Cox 1977). In the vertical alignment a net "suction" of the trailing bubble by the leading one occurs due to the vorticity asymmetry of the two bubble hemispheres. Now, it could happen that the two bubbles rising in this way will find an equilibrium distance between them when the viscous (attractive) and inertia (repulsive) forces cancel each other. That is to say, when the trailing bubble experiences the same amount of suction by the leading bubble wake and repulsion caused by its own upper wake when the two bubbles interact at short separation distances. This issue was in fact numerically analyzed by Yuan and Prosperetti (1994). They found such an equilibrium position between two in-line spherical bubbles rising in different hydrodynamic conditions ($20 < Re < 200$). Experimentally, an unstable equilibrium distance can indeed be found for clean bubbles which preserve its spherical shape as increasing the Re number (i.e. rising in silicone oils, Watanabe & Sanada 2006). Such equilibrium distance, which has been numerically found to be dependent on the Re number (Yuan & Prosperetti 1994, Hallez & Legendre 2011), is unstable in the sense that bubbles often escape from the vertical line.

Several experimental and numerical studies of the interaction of two bubbles at intermediate Re numbers have been devoted to the construction of the bridge that joins the creeping and potential flows (Bhaga & Weber 1980, Kim *et al.* 1993, Kok 1993b, Katz & Meneveau 1996, Hallez & Legendre 2010, Sanada *et al.* 2009). These studies have revealed that two bubbles rising in-line follow the viscous dominated flow behavior at least up to a Reynolds number of $O(100)$, i.e., the trailing bubble approximating the leading one. The question if an equilibrium distance appears or not during this process, i.e. the trailing bubble being ejected from the vertical line or reaching and making contact with the leading bubble, seems to depend on the shape and the surface properties of the bubbles. In particular, Kok (1993b) observed in contaminated water (water with surfactant, $Re \approx 200$) that a trailing bubble reaches, touches, then turns its orientation angle to 0° with respect to the leading one and finally separates from it; a mechanism commonly referred to as the drafting-kissing-tumbling process (Brennen 2005). This process is commonly observed in rigid bodies at low Re numbers (Happel & Pfeffer 1960, Jayaweera *et al.* 1964). In the case of two bubbles released side-by-side it has been found that they always repel each other for $Re < 30$ and attract each other for $Re > 0(200)$, being the transition behavior $30 < Re < O(200)$ dependent on the separation distance (Legendre *et al.* 2003).

Regarding the drag force experienced by a pair of bubbles, in the vertical alignment the mean drag experienced by each bubble is less than the single bubble case. This is because the conjunction of the two bubbles will "form a body" aligned in the direction of the flow (Yuan & Prosperetti 1994, Ruzicka 2000). The prediction of the drag coefficients of two bubbles rising side-by-side is more complicated. With the help of the experimental measurements of the drag coefficients in fixed rigid particles (Liang *et al.* 1996), together with the numerical works of Kim *et al.* (1993) and Legendre *et al.* (2003), it has been found that two horizontal bubbles will experience less drag than the single one for low Reynolds flows ($Re < 50$). In this case the drag value increases with the separation distance approaching the single bubble value at high values of it. In small Re flows the long range interactions between bubbles gain importance; hence, two bodies moving side-by-side separated by a small distance, typically less than a bubble radius, will be surrounded by a unique vortex (Liang *et al.* 1996); therefore, the two bubbles will find less resistance to motion. The opposite effect is found for high Re flows where wake instabilities can occur. This explanation is at least consistent with the behavior that has been observed in Newtonian bubbly flows at low Re, that is, the formation of clusters formed by little more than five bubbles (Cartellier *et al.* 1997). In such flow conditions, however, the bubble clusters are highly unstable as the gas fraction is increased.

2.2.2 Non-Newtonian fluids

Important advances concerning the interaction of two bubbles rising in non-Newtonian flows have been given by the experimental and numerical studies of Li *et al.* (1997 & 1998), Radl *et al.* (2007), Sousa *et al.* (2007) and Wenyuan *et al.* (2009). Using fluids with shear-thinning and elastic behavior, Li *et al.* (1998) and Radl *et al.* (2007) elucidated that the viscosity gradients together with the amount of elasticity (memory effects) enhance bubble interactions (the term "viscosity gradients" is explained in section 6.2.3). The idea of "corridors" of reduced viscosity is commonly brought to mind when one imagines a trailing bubble following a leading bubble in a viscoelastic fluid. The corresponding decrease of the drag force was further related to the accumulation of residual stress via rheological simulations, a term coined by Li *et al.* (1997). In that work, the passage of bubbles was simulated by exerting consecutive deformations to a fluid sample in a rheometer. The viscosity reduction in the bubble wake and the time lag needed for the zero-shear viscosity reestablishment extends the influence that a leading bubble has on other bubbles. This effect is not expected to occur in Newtonian fluids. The most outstanding behavior that has been observed regarding non-Newtonian effects was the repulsive effect that the formation of a negative wake produces between a leading Taylor bubble and a trailing one (Sousa *et al.* 2007). This effect has, nevertheless, been observed only in slug flow regimes where the bubbles fill completely the column diameter. As far as we know, only Wenyuan *et al.* (2009) have experimentally studied the interaction of two bubbles rising in thinning fluids (carboxymethyl cellulose, CMC, solutions). Their results, however, are very similar to those seen in Newtonian flows and this can be attributed to the fact that they worked with fluids having a flow index very close to one

($0.9 < n < 0.94$). As previously mentioned, Singh and Denn (2008) and Tsamopoulos *et al.* (2008) have numerically studied the movement of bubbles and droplets in Bingham fluids. As these fluids have a yield stress value, the flow around the bubble is divided in three zones: an unyielded zone localized in the equatorial plane of the bubble, a yielded zone surrounding this one and which in turn is surrounded by a second external unyielded region. When the fluid properties and bubble size are such that the external and internal unyielded regions merge, the bubble will not move. Singh and Denn also studied the interaction of two and three bubbles rising in a Bingham fluid. During the collision, the shape evolution of the bubbles is similar to that seen in Newtonian fluids. The authors also noted that given a collection of fluid properties and bubble size that will result in the immobilization of one bubble, the addition of a second or a third bubble vertically aligned with the first one will produce enough stress to the fluid that the bubble group will start to move through the liquid.

From this brief review we can perceive that there is a good understanding of the non-Newtonian behavior: the memory that a fluid has about the reduced viscosity path left by a previous bubble will enhance the bubble interactions. However, we can note that there are some points that need clarification; for instance, it is important to explore the interaction of a bubble pair in a wider range of the flow index values and see how different is the behavior with respect to the Newtonian case; moreover, the role of elasticity, in one hand, and the thinning behavior, in the other, on the bubble interaction need to be fully elucidated. These particular issues are treated in this thesis.

2.3 Bubble swarms

Several theoretical, numerical and experimental studies, carried out in two phase flows (including sedimentation and bubble flows), have shown that a group of bodies moving through a non-Newtonian fluid form aggregates or clusters (Joseph *et al.* 1994, Gheissary & van den Brule 1996, Hu *et al.* 2001, Radl *et al.* 2007, Phillips & Talini 2007). Such aggregates are more dense in terms of the number of bodies embedded in the cluster than the ones seen in Newtonian flows at high Reynolds numbers (Zenit *et al.* 2001, Figueroa-Espinoza & Zenit 2005). Bubble clustering cause bubble coalescence and a premature transition to the heterogeneous or churn-turbulent flows in non-Newtonian fluids (Buchholz *et al.* 1978, Schumpe & Deckwer 1982). Although there has been a number of studies of particle clustering and orientation of lengthened bodies in sedimentation (Joseph & Liu 1993, Joseph *et al.* 1994, Gheissary & van den Brule 1996), little has been reported for the case of bubbly or homogeneous bubble flows. Most of the published papers on non-Newtonian bubble columns have focused their attention on the development of the gas fraction, Φ_g, in terms of the superficial gas velocity, U_g. Many authors have used CMC solutions (flow index $n > 0.5$, Buchholz *et al.* 1978, Schumpe & Deckwer 1982, Deckwer *et al.* 1982, Godbole *et al.* 1984, Haque *et al.* 1987 & 1988) in coalescence conditions and worked with relatively large values of the superficial gas velocity ($U_g > 2cm/s$, Godbole *et al.* 1984, Haque *et al.* 1987 & 1988) such that the churn-turbulent flow was generally achieved.

Buchholz *et al.* (1978) reported that the mean bubble rise velocity $\overline{U}_{SW}$ measured in a single stage column was higher than the single bubble velocity U_{SI}. Additionally,

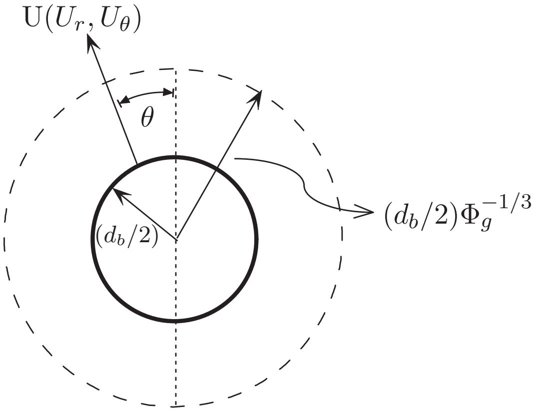

Figure 2.2: Happel cell model. This model is actually a special boundary condition which consists in simplify the bubble-bubble interactions by postulating that each bubble is surrounded by a hypothetical spherical envelope with a slip boundary condition and who's radius is equal to $(d_b/2)\Phi_g^{-1/3}$. The governing equations are then solved in the space between the bubble surface and this envelope.

this difference increased with the thinning behavior of the fluid. However, the changes of the $\overline{U}_{SW}/U_{SI}$ ratio with the gas fraction were not reported explicitly. Schumpe and Deckwer (1982) found that the homogeneous bubble regime in CMC solutions could only be achieved having U_g values below a critical one ($\sim 0.5cm/s$), this value being a function of the effective viscosity. Haque *et al.* (1987, 1988) reported an estimation of the mean bubble diameter and velocity of bubble swarms rising in viscoelastic fluids. One of the key assumptions in this estimation is that the mean bubble velocity values are equal to the single bubble velocity, which is not always true. As far as we know, there are no previous studies of mono-dispersed bubble swarms in shear-thinning fluids at low superficial gas velocities ($U_g < 1cm/s$) where the bubbly flow regime can be observed. Having a monodispersed bubble distribution allows us to isolate the effects caused solely by the hydrodynamic interaction among bubbles.

Many relevant contributions to the subject have arisen from numerical and analytical studies. Several methods such as variational principles (Gummalam & Chhabra 1987), perturbation methods (Bhavaraju *et al.* 1978b) and approximations to the Newtonian behavior (Hirose & Moo-Young 1969) have been used to solve numerically the rising of bubble swarms through shear-thinning fluids. Bubble interactions were simplified using the Happel cell model (Happel 1958) depicted in figure 2.2; hence no direct bubble interactions have been studied previously. Only Radl *et al.* (2007) have fully resolved the flow field around a group of bubbles. These authors directly simulated the interactions of bubbles (up to 9) rising in shear-thinning conditions. They showed that the bubble interactions are significantly enhanced when viscosity gradients are present. They also identified “mini-bubble” clusters that travel faster than the single bubble cases. Bhavaraju *et al.* (1978b) reported that for creeping flow conditions the drag coefficient C_d decreased with the increase of the thinning behavior for bubble swarms, which is the opposite of what happens for single bubbles. Ascending isolated bubbles have a larger

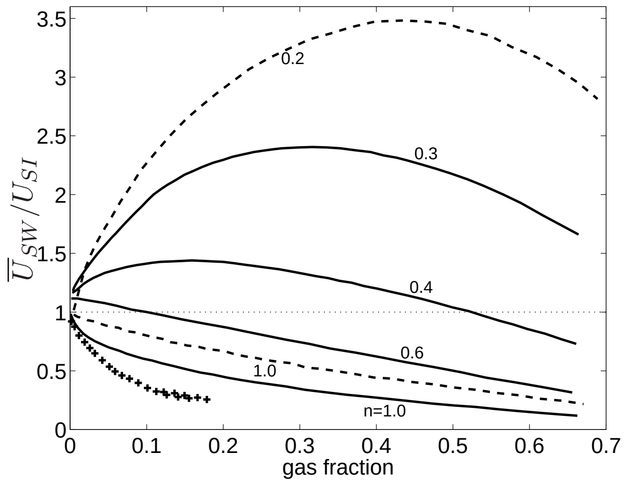

Figure 2.3: Velocities ratios $\overline{U}_{SW}/U_{SI}$ as a function of the gas fraction. ($-$) theoretical values for creeping flow (Gummalam & Chhabra 1987), ($--$) theoretical values for high Re flows ($100 < Re < 300$, Chhabra 1998); (+) experimental data taken from Zenit *et al.* (2001), $n = 1.0$ and $Re \approx 300$; n is the flow index.

C_d as the thinning condition increases in creeping flows (Hirose & Moo-Young 1969, Acharya *et al.* 1977, Haque *et al.* 1988, Rodrigue *et al.* 1999a). In more recent studies, which took into account the inertial forces in the momentum equation (Zhu *et al.* 2003, Kishore *et al.* 2008), the increase in the drag force for the single bubble case occurred only below a critical Reynolds number (approximately from 3 to 10). Gummalam and Chhabra (Gummalam & Chhabra 1987, Chhabra 1998)[4] reported that for the creeping and high Re numbers ($100 < Re < 300$) flows, the $\overline{U}_{SW}/U_{SI}$ ratio increases for gas fractions around 0.2-0.5 and flow index values below 0.5. Above these gas fraction values the velocity ratio decreases; therefore, a maximum in the velocity ratio was observed, as shown in figure 2.3. These authors explained that such behavior was due to the constrain of the flow lines (as the effective volume for each bubble is decreased as the gas fraction increases) resulting in an increase of the shear rate which in turn results in lower apparent viscosities. A positive slope of the velocities ratio curve means that the viscosity gradients effects surpass the hydrodynamic hindrance effects. The slope of the $\overline{U}_{SW}/U_{SI}$ curve is commonly negative in Newtonian bubbly liquids with large Reynolds and small Weber numbers (Spelt & Sangani 1998, Zenit 2001). It is important to point out that the theoretical results of Bhavaraju *et al.* (1978b), Gummalam & Chhabra (1987) and Chhabra (1998) have not been compared with experiments yet. The comparison between the theoretical results of Gummalam and Chhabra with experimental results together with the study of bubble clusters seen in numerical and experimental studies conform two of the main objectives of the present investigation.

---

[4] In Gummalam & Chhabra (1987), the authors warn us that the values having $0.1 < n < 0.3$ have to be treated with reserve due to the inaccuracy of the method that they used.

Chapter 3

Objectives

Through all the background, some of the aspects in multiphase flows in non-Newtonian liquids that still need additional research have been identified. The main objectives of the present work are:

- Measure the mean bubble size and velocity as a function of the gas fraction in thinning inelastic bubbly flows and compare the results with the available theoretical data.
- From the measurements of the diameter and velocity of the bubbles, determine the variance of the gas phase velocity and relate it with the appearance of bubble clusters in the thinning inelastic fluids.
- Determine the hydrodynamic conditions in which the bubble clusters are formed in the thinning inelastic fluids.
- Measure the mean cluster size at different values of the gas fraction and determine the effect that the bubble diameter has on its size.
- Obtain the mean and standard deviation of the liquid velocity in elastic fluid flows with low thinning behavior. Explain the relation of possible changes in the bubble dispersion (clustering) with the flow changes seen in the single bubble case (i.e. velocity jump discontinuity). These first objectives needed the following specific tasks:
  1. Design and assembly of the capillary banks needed for the production of mono-dispersed bubble flows.
  2. Design of the working fluids. An effort was made in designing thinning fluids with negligible elasticity and elastic fluids with low thinning behavior. The reason in doing this was to identify the separate contributions of both behaviors.
  3. Measurement of the bubble velocities and diameters and the cluster size using a high speed camera and a homemade algorithm run in $Matlab^{®}$.

When these objectives were achieved, the advisory committee and I realized that further research was needed in order to explain the experimental results, that was how the following objective was proposed:

- Explain the behavior seen in the bubble flows in terms of the interaction of two bubbles rising in the different non-Newtonian fluids. Analyze the effects of the initial distance and angle between bubbles in the subsequent interaction among them. This second objective needed the following specific tasks:
    1. Design and assembly of an equipment capable to produce two in-line bubbles and two bubbles placed in an horizontal (off-line) arrange.
    2. Measurement of the bubble velocities and center-to-center distance between bubbles using a movable high speed camera. This particular task was done by an undergraduate student (see Sámano 2011).
    3. Study the interaction of two bubbles placed in an arbitrary initial arrangement (with an initial contact angle θ_o) using finite element methods for deformable bodies, in particular, the Arbitrary Lagrangian-Eulerian technique.

It is well known that the initial ideas that one proposes in a scientific work before doing any experiment are frequently changed or even forgotten. Curiously, there is a part of the original research protocol (which does not mention anything about bubble clustering and their growth) that is worth mentioning. The statement in question said something like *"... the change of the bubble shape seen in viscoelastic fluids, which has been associated with the velocity jump discontinuity in single bubbles, will have a significant influence in the development of the pseudo-turbulence*[5]. At the end of the research a couple of measurements of the agitation levels were done in the elastic fluids and it was found that indeed, the change of the bubble shape seen in viscoelastic fluids has a significant effect on the mixing and bubble dispersion. This effect is nevertheless not a direct consequence of the change of the bubble shape but of the change of the boundary condition at the bubble surface (see section 7.3).

---

[5] During my candidacy exam I actually had a very intense debate about the meaning of "pseudo-turbulence", a word that refers to the liquid agitation provoked by the passage of bubbles and not by the movement of the liquid. This term is used by serious researchers (see vanWijngaarden 1998). Another word can also be used, "burbulence", but is better not to use this term because it can be confused with the medical meaning, which says that *burbulence* is a group of intestinal symptoms including fullness, bloating or distention, borborygmus and flatulence.

Chapter 4

Computational technique

In the background chapter we noted that a good part of the comprehension of the multiphase flow dynamics has resulted from the analysis of numerical simulations using different computational algorithms. This is because the numerical simulations allow us to see if the assumptions that we have assigned to a specific problem are actually true. The Arbitrary Lagrangian-Eulerian (ALE) technique is part of a family of algorithms grouped in what is called "direct numerical simulations"; that is, the governing equations (mass, momentum and constitutive equations) are solved in all space and time scales (the computational time and space is smaller than the characteristic time and size of the flow). This technique was developed by Hu *et al.* (2001) to solve the motion of particles in two- and three-dimensional flows and modified by Yue *et al.* (2007) to study bubble and foam problems in 2D and axisymmetric geometries. A detailed description of this technique and its algorithm can be found in Yue *et al.* (2007) and Prosperetti & Tryggvason (2009). The general features of the code will be described briefly.

The technique combines an Eulerian and Lagrangian descriptions of the flow and bubble motion using an unstructured finite element mesh. This means that the boundary nodes of the mesh follow the motion of the bubbles and the walls with possible slip. In the interior of the domain, however, the mesh motion does not follow the fluid flow but is computed from an elliptic partial differential equation which guarantees a smooth variation. The code includes a remeshing tool that generates a new mesh upon detecting elements with unacceptable distortion. When this happens, a projection scheme is also invoked to project the flow field obtained on the old mesh onto the new one. An example of a mesh generated around two bubbles is shown in figure 4.1. The flow equations include the continuity equation:

$$\nabla \cdot \underline{u} = 0 \tag{4.1}$$

and the momentum equation:

$$\rho \left[\frac{\partial \underline{u}}{\partial t} + (\underline{u} - \underline{u_m}) \cdot \nabla \underline{u} \right] = -\nabla p + \nabla \cdot \underline{\underline{\tau}} + \rho \underline{g} \tag{4.2}$$

where, in the case of the thinning fluids, the stress $\underline{\underline{\tau}} = \eta \left[\nabla \underline{u} + (\nabla \underline{u})^T \right]$ is computed using the power-law model for the viscosity:

$$\eta = k \left[\sqrt{\frac{1}{2}(\underline{\underline{\dot{\gamma}}} : \underline{\underline{\dot{\gamma}}})} \right]^{n-1} \tag{4.3}$$

For the elastic fluids, the viscosity was held constant and the stress was split into the solvent and polymer stresses (as mentioned in section 1.4) according to the Oldroyd-B model:

$$\underline{\underline{\tau}} = \underline{\underline{\tau_s}} + \underline{\underline{\tau_p}} = \eta_s \left[\nabla \underline{u} + (\nabla \underline{u})^T \right] + \underline{\underline{\tau_p}} \tag{4.4}$$

$$\underline{\underline{\tau_p}} + \lambda_1 \left[\frac{\partial \underline{\underline{\tau_p}}}{\partial t} + (\underline{u} - \underline{u_m}) \cdot \nabla \underline{\underline{\tau_p}} - \underline{\underline{\tau_p}} \cdot \nabla \underline{u} - (\nabla \underline{u})^T \cdot \underline{\underline{\tau_p}} \right] = \eta_p \left[\nabla \underline{u} + (\nabla \underline{u})^T \right] \tag{4.5}$$

In these equations $\underline{u}$ is the liquid velocity, ρ the density, p the pressure, η the viscosity, $\underline{g}$ the gravity, k the consistency index, n the flow index, λ_1 the relaxation time, $\underline{\underline{\dot{\gamma}}} = \left[\nabla \underline{u} + (\nabla \underline{u})^T \right]$ the shear rate tensor and $\underline{u_m}$ the mesh velocity, which was obtained from the displacement of the mesh nodes according to the fixed computational coordinates. The referential time derivative $\frac{\partial}{\partial t} = \frac{\delta}{\delta t}|_{fixX}$ is made using the coordinate $\mathbf{X}$ affixed to the moving mesh.

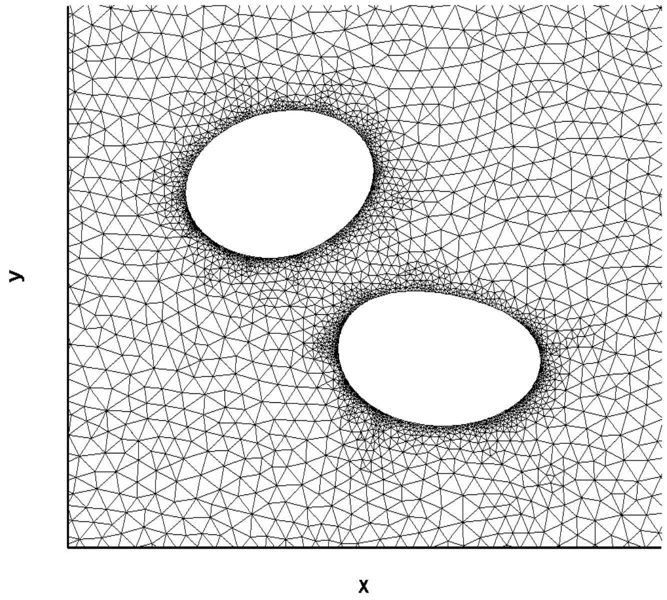

Figure 4.1: Mesh generation around two bubbles (2D). Note that the mesh generated next to the bubble surface is finer than the mesh generated in more distant regions. After the code generates an appropriate grid on the bubble and domain surfaces, the segmentation of the interior of the domain in triangular shaped elements is done by the Delaunay-Voronoi algorithm.

As we have introduced another variable to the constitutive and momentum equations, namely, the mesh velocity $\underline{u_m}$; we need an extra equation to solve the system. As it was mentioned above, the equation that rules the mesh velocity inside the domain is an elliptic partial differential equation:

$$\nabla \cdot (k^e \nabla \underline{u_m}) = 0 \tag{4.6}$$

This equation gives a smooth variation of the mesh velocity because the Laplace operator guarantees that there will be no preferential directions in the mesh motion. k^e is the inverse of the local element volume and serves to direct most of the mesh deformation in regions far from the bubbles.

The governing equations were temporarily discretized using an implicit scheme to enhance stability implementing a Crank-Nicolson scheme in the time derivative:

$$\left(\frac{\delta A}{\delta t}\right)^{n+1} = \frac{2A^{n+1} - A^n}{t^{n+1} - t^n} - \left(\frac{\delta A}{\delta t}\right)^n \tag{4.7}$$

where the superscripts n and $n+1$ indicate the time step. The spatial discretization of the equations was done using the standard finite element Galerkin formalism. The methodology of this technique may be harder to understand than the usual finite difference schemes where the concept of normal flux is related to the structure of the mesh. However, the finite element method has the advantage of adapting complex structures that will be mathematically complex to implement in the finite difference schemes. The finite element method is based on the general method of weighted residuals (to learn more about the subject see the books of Kwon & Bang 1997 and Chung 2002). The idea of this method is to solve differential equations like 4.1-4.5, which have the form:

$$D(u, u_m, \tau, p) = 0 \tag{4.8}$$

by using the trial functions $\widetilde{u}$, $\widetilde{u_m}$, $\widetilde{\tau}$ and $\widetilde{p}$ (usually polynomial equations of first or second order) which fulfills the Dirichlet boundary conditions. We expect that this approximate solution will vary from the exact solution over the whole domain. In order to minimize such variations, we can introduce a weighting function w and state that the weighted average of the residual over the whole domain (D) is zero. In mathematical terms:

$$\int_D wR\,dx = 0 \tag{4.9}$$

where R is the residual, that is, the differential equations put in terms of the trial functions instead of the common variables. Different types of weighted functions can be chosen leading to different methods (collocation method, least squares, Galerkin method, see Kwon & Bang 1997). In the case of the Galerkin method the weighted functions are defined in terms of the trial functions. Since the position of the nodes (vertices) of each triangle that compose the whole domain depends on the shape of the triangle itself (which may have sides with different lengths), the weighted functions are known as shape functions.

The boundary conditions that were applied to the problem of one or two bubbles rising in the different fluids were the following: at the bottom wall the no slip condition was applied; at the right and left walls the slip condition in the $y - direction$ was applied and the horizontal velocity component was set to zero; stress condition was applied at the liquid surface, both on the normal component ($\tau_{\mathbf{yy}} = p - p_o = 0$) and the tangential component ($\tau_{\mathbf{xy}} = 0$); on the bubble surface the boundary condition was obtained from the Young-Laplace equation:

$$\underline{n} \cdot (-p\underline{\underline{I}} + \underline{\underline{\tau}}) = (-p_b + K\sigma)\underline{n} \tag{4.10}$$

with the tangential components also set to zero (no surfactants). Here, $\underline{n}$ is the normal vector to the bubble surface, K the surface curvature, σ the surface tension and p_b the pressure inside the bubble. The initial pressure of the bubble is given by $p_b = p_o + \rho g_y(H - h) + 2\sigma/r$ where H is the height of the domain, h the height in which the bubble was released, r the half of the bubble diameter defined by equation 5.1 and p_o the reference pressure (1.01×10^5Pa). In the simulations, p_b is updated according to $p_b V_b = constant$, where V_b is the bubble volume. The domain size was $16r \times 50r$. This size was the same for the 2D and axisymmetric calculations; hence, $16r$ is the width for the 2D domain and also the diameter of the cylinder of the axisymmetric geometry; $50r$ is the height in both geometries. Non-dimensionalized variables were introduced to the code considering the following scales: ρ for the density ($\rho^* = 1$), r for the length, r/U_{SI} for the time, U_{SI} for the velocity and ρU_{SI}^2 for the pressure and stress, U_{SI} being the terminal velocity of the single bubble measured in the experiments. The viscosity, surface tension and gravity were non-dimensionalized using the experimental values of the Re ($= \rho U_{SI} r/\eta$), We ($=\rho U_{SI}^2 r/\sigma$) and Eo numbers, respectively, and the scales mentioned above. The nonlinear set of equations are solved using the Newton-Raphson method together with Krylov subspace iterative solvers such as the preconditioned generalized minimum residual (GMRES)[6]. The simulations were conducted in a computational grid located in Canada (glacier.westgrid or driftwood.iam.ubc). A typical job consisting of 25,000 elements takes less than a day to complete a run with 10,000 time steps. An upper limit for the time step is given by $\Delta t = 0.0005t^*$, where $t^* = r/U_{SI}$. For the single and in-line bubbles (sections 6.1 and 6.2.1) the axisymmetric geometry was used while for the bubbles rising side-by-side or with other angles (sections 6.2.2 and 6.2.3) the 2D solver was used. The data resulted form the simulations were further analyzed and plotted using $Tecplot^{®}$.

4.1 Comparison between Newtonian and non-Newtonian flows

This work compares the behavior of the bubble flow in Newtonian and non-Newtonian fluids keeping certain properties 'equal'. Although this comparison is much more easy to

---

[6] The Newton-Raphson algorithm is used to find the roots of the nonlinear set of equations using an initial guess value. The resulting linear system within each Newton iteration and the linear system of eq. 4.6 are solved using the GMRES algorithm. This GMRES algorithm is a kind of an orthogonalization procedure; by orthogonalization we may think in the geometric principle that the shortest distance from a point (the final values that solve the equations) to a plane (the equations themselves) is the length of the perpendicular joining them, see Gill *et al.* 1991.

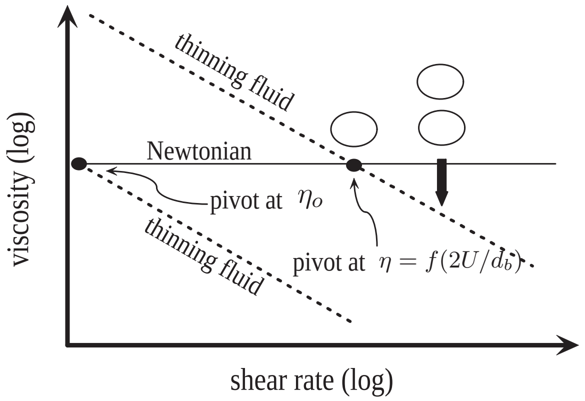

Figure 4.2: Scheme indicating the relation of a Newtonian fluid with its thinning counterpart. The ovoids, representing a bubble and a bubble pair, indicates the characteristic shear rate value of the flow: if the viscosity value is fixed at the characteristic shear rate of a single bubble, a bubble pair will rise faster due to the lower viscosity profile, see section 6.2.1.

do with computational simulations than with real experiments, there are some guidelines that we must observe. Having a Newtonian fluid with viscosity η, we can make an hypothetical thinning fluid with an index flow n by rotating the constant viscosity curve using η_o (zero-shear viscosity) as a pivot or using a viscosity defined at the characteristic shear rate of the flow $\dot{\gamma} = 2U/d_b$ (see figure 4.2). If the first option is chosen (as in Zhang *et al.* 2010), we can expect then that all the simulations run in the thinning fluid, whatever the size of the bubble is chosen, will have a higher terminal bubble velocity than that obtained in the Newtonian fluid since the viscosity will be always lower. Interestingly, if the second option is chosen, it happens that the bubble rising in the thinning fluid will reach a lower velocity than the bubble (having the same size) rising in the Newtonian one. This is due to the higher viscosity profile appearing in the regions far from the bubble (see section 6.1). In view of these differences, one is forced to clarify which variables between the Newtonian and its thinning counterpart are being changed and which are fixed in a numerical simulation. One can further compare the numerical results using the Reynolds number as the fixed variable (see Dhole *et al.* 2007, Kishore *et al.* 2008), but in this case the size of the bubble, or the liquid density are not fixed. What was done in this study was to leave all the physical variables equal between the Newtonian and its thinning counterpart (or viceversa), including the apparent viscosity at the characteristic shear rate (pivot at $2U/d_b$). Hence, the only variables that were changed were the flow index n and the consistency index k.

Chapter 5

Experimental setup

5.1 Column and bubble generation

A rectangular channel with $5 \times 10 \times 160$ cm^3 equipped with a gas chamber (7.5% of the channel height) was used, similar to that used by Martínez-Mercado *et al.* (2007). Pure nitrogen was introduced to the bubble column using a needle valve (*Cole-Palmer 1682ml/min MAX, stainless steel ball*). The superficial gas velocity U_g range was between 0.09 and 0.6 cm/s. The gas volume fraction, Φ_g, was obtained using the relation $\Phi_g = \Delta H/H$, where H is the liquid height without gas (140cm) and ΔH the height difference produced by the introduction of the gas in the column. The experimental setup can be seen in figure 5.1

Three capillary banks were constructed in order to produce different bubble sizes (d_b). The internal diameter of the capillaries (D_{cap}) was selected considering the equilibrium condition between buoyancy and surface tension forces (eq. 1.25). In order to avoid the generation of gas jets, the hydraulic resistance through the capillaries should be large such that the bubble volume depends mainly on the buoyancy and surface forces and lesser in the gas flow rate (Oĝuz & Prosperetti 1993). The equivalent capillary lengths necessary to achieve such hydraulic resistance are sometimes of the order of meters; instead of installing long capillaries, a second capillary with a smaller inner diameter was inserted to the main capillary but the bubble formed on the larger diameter end. This arrangement provides the sufficient hydraulic resistance to produce individual bubbles. As we can see in figure 5.2, identical capillaries were placed in an acrylic perforated plate ordered in an hexagonal arrange. The design parameters of the three capillary banks are summarized in Table 5.1.

	D_{cap}(mm)	N	$\overline{d}_b$(mm)	$\lambda/\overline{d}_b$	$\lambda_{wall}/\overline{d}_b$	L(cm)
1	0.2	63	2.15	2.8	6.7	4.3
2	0.6	27	3.15	2.7	4.9	8.0
3	1.6	16	4.20	2.7	3.7	8.0

Table 5.1: Design parameters of the capillary banks. D_{cap}, internal diameter of the capillaries; N, number of capillaries; $\overline{d}_b$, experimental mean bubble diameter; λ, spacing between capillaries; λ_{wall}, spacing between capillaries and the wall; L, capillary length.

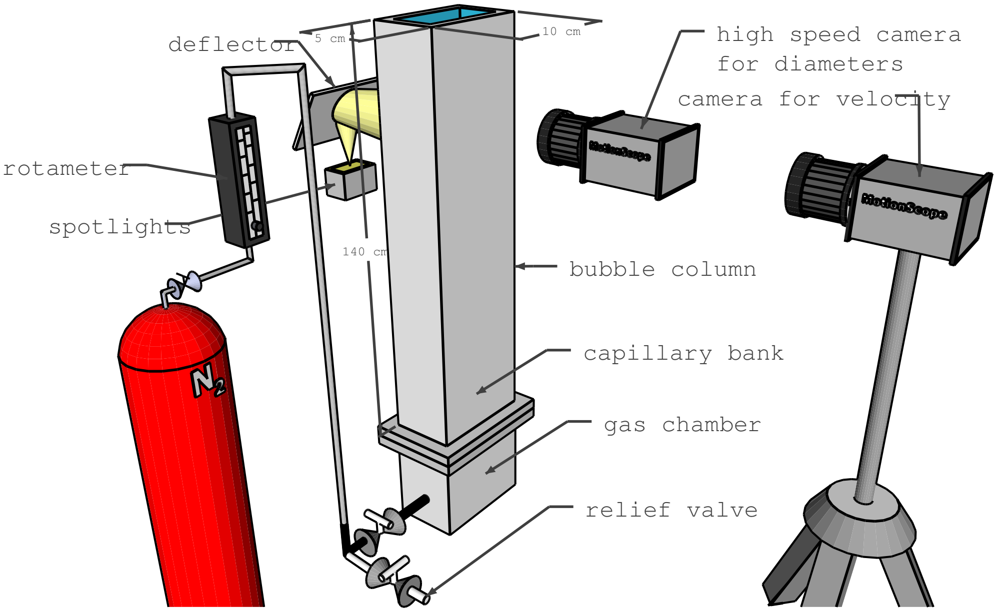

Figure 5.1: Experimental Setup

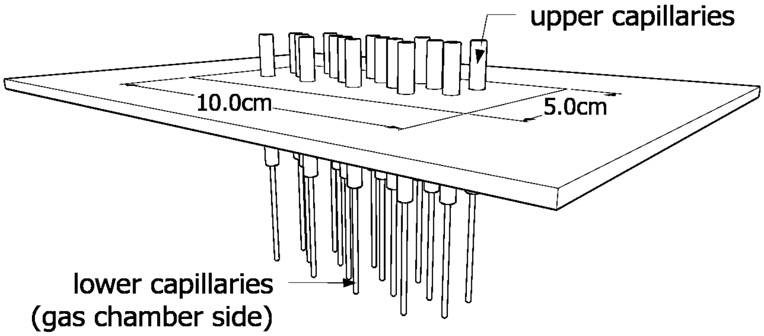

Figure 5.2: Scheme of a capillary bank

	Capillary I.D.	Bubble diameter
small	0.2 mm	2.1 mm
medium	0.6 mm	2.8 mm
large	1.2 mm	3.6 mm

Table 5.2: Bubble diameters obtained by the capillaries (I.D.: inner diameter of the capillaries) shown in figure 5.3.

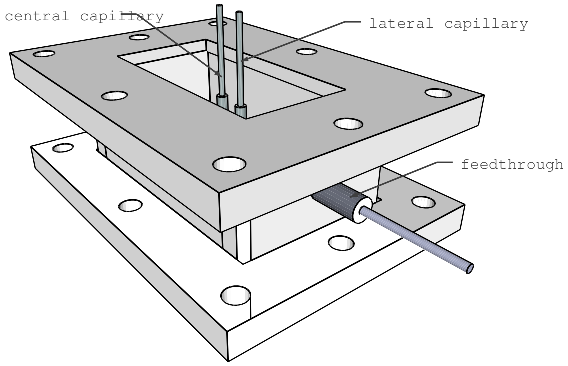

Figure 5.3: Device for the generation of two in-line bubbles or two bubbles rising side-by-side.

A special device was constructed for the generation of the bubble pairs (figure 5.3). This device can be attached to the column and replace the capillary bank and the gas chamber when the bubble pair experiments were carried out. To generate in-line bubble pairs (vertical alignment), one capillary was inserted through the bottom of the column, using a sealed feedthrough (*Spectite Series PF*), at the center of the base plate. To generate bubble pairs aligned horizontally, a second capillary was inserted through the side wall, using an elbow and another feedthrough connector. In this manner the initial horizontal separation could be varied. Table 5.2 shows the bubble size that were obtained with the different capillaries using the experimental setup for the bubble pair generation. Air was injected through the capillaries with a syringe pump (*KDScientific 100L*). To ensure that the polymer solution was completely at rest, a time interval of approximately 5 minutes was left in between experiments. Regarding this point, a notable difference in the terminal velocities of two bubbles released one after the other was not seen for periods above one minute. The whole column was disassembled and cleaned at the end of the day.

5.2 Fluids

The thinning fluids used in this study fulfilled two conditions: (1) show a shear-thinning power-law behavior with negligible elastic properties and (2) allow the formation of mono-dispersed bubbly flows, that is, with a narrow dispersion of $\overline{d}_b$. For the case of the elastic fluids, the liquids were formulated such that they had a nearly constant viscosity. Although we can be certain that the total separation of the elastic and thinning properties of a polymer solution is rather impossible, we can make solutions with low elasticity by using rigid polymer molecules. It was found that xanthan gum (rigid-like polymer) solutions in water/glycerin mixtures fulfilled the above conditions for the thinning fluids. These solutions are more stable in the presence of $MgSO_4$ (which was added to delay coalescence, Lessard & Ziemiski 1971) than carbopol, CMC or guar gum solutions. The preparation of the thinning solutions was as follows: first the xanthan gum (*Keltrol E 415, KELCO, USA*) was dissolved in water (at $55°C$), then the salt (0.04M of $MgSO_4$, *2500-01 J.T. Baker*) was added and finally the glycerin.

The elastic fluids with nearly constant viscosity (Boger-type fluids) can be made either by dissolving a small amount of flexible polymer in a highly viscous solvent, such as the "classical" Boger fluids (James 2009), or by hindering the orientation of the polymer chains with the flow by forming a transient network (Tan *et al.* 2000). Although historically, Boger fluids are usually diluted polymer solutions, we will use this term to denote a fluid with elasticity and nearly constant viscosity regardless its composition or polymer concentration. One of the elastic fluids (semidilute solution, Boger-1) was made by dissolving 400ppm (0.04%) of ionic polyacrylamide (Paam, *Aldrich 181277*, $M_w = 5 \times 10^6$g/mol) in a 80/20 (v/v) glycerin-water mixture having 9.8g/L of $MgSO_4$.

The rheological measurements were done in a rheometer (*TA Instruments AR1000N*) with a cone-plate geometry (60mm, 2°, a gap of 65 μm). The surface tension measurements were performed with a DuNouy ring (diameter of 19.4mm, *KSV Sigma 70*). All the solutions were stirred before the surface tension measurement. The temperature of the room was $23°C$. The physical properties of the solutions are summarized in Table 5.3; the flow curves of the thinning solutions and the curve of the Boger-1 fluid are shown in figure 5.4 and 5.5 respectively. Three additional curves are included in figure 5.5. The first and second curves are the viscosity and normal stress of a Boger fluid used by Pelletier *et al.* (2003), similar to the one employed in this work. The reason of including this fluid is to support the argument, used in section 7.1.1, that although our Boger-1 fluid was made with a ionic polymer, the addition of the salt made it behave like a flexible polymer, as it shows a behavior similar to that used by Pelletier *et al.* , which used nonionic polyacrylamide. The third curve is the viscosity of the Boger-1 fluid used in this study two weeks after the experiments. The curve shows a thickening behavior at $\dot{\gamma} > 100$. This kind of behavior was already described by Choplin and Sabatié (1986) and is due to conformational changes of the macromolecules and possible formation of intermolecular bonds induced by high shear rates (which are well above the value where the velocity jump occurs, $\dot{\gamma} \approx 40$, see section 7.1.1). The polymer concentration parameter c for this fluid, defined as the ratio of the polymer and solvent contribution to the zero-shear viscosity, $c = \eta_p/\eta_s$, is 0.85. The solutions were left in repose for a minimum of 24 hours before experiments.

At a shear rate of $10s^{-1}$ all the thinning fluids (fig.5.4) have a viscosity of around one hundred times that of water. The shear-thinning fluids have a power-law behavior in almost all the shear rate interval; a mild plateau can be observed for shear rates below $0.1s^{-1}$. This indicates that the polymer chains are gently stretched by a flow field, having a short range of linear viscoelasticity. Within this short linear range, the elastic modulus G' becomes bigger than the loss modulus G" only at high frequencies ($> 100s^{-1}$) as can be seen in figure 5.6. Both G' and G" were obtained by a Fourier Transform (FT) of the stress relaxation curves measured with an *ARG2* rheometer of controlled stress (Calderas

Fluids	ρ kg/m^3	σ mN/m	η or k $mPa{\cdot}s^n$	n
Newtonian: 83% glycerin/water	1214.6	61.9	104.2	1.0
0.02% xanthan gum in 75% glycerin/water	1193.1	63.0	118.7	0.85
0.035% xanthan gum in 70% glycerin/water	1179.5	62.0	143.4	0.76
0.1% xanthan gum in 60% glycerin/water	1152.1	65.0	360.0	0.55
0.23% xanthan gum in water	997.5	66.5	574.9	0.32
Boger-1: 0.04% polyacrylamide in 80 % glycerin/water	1206.7	55.6	108.4	0.96

Table 5.3: Physical properties of the fluids: ρ, density; σ, surface tension; η, viscosity; k, consistency index; n, flow index. The percentages of liquid mixtures are given in volume terms, the percentages of the polymers solutions in weight terms. All the solutions had 9.86g/L of $MgSO_4$.

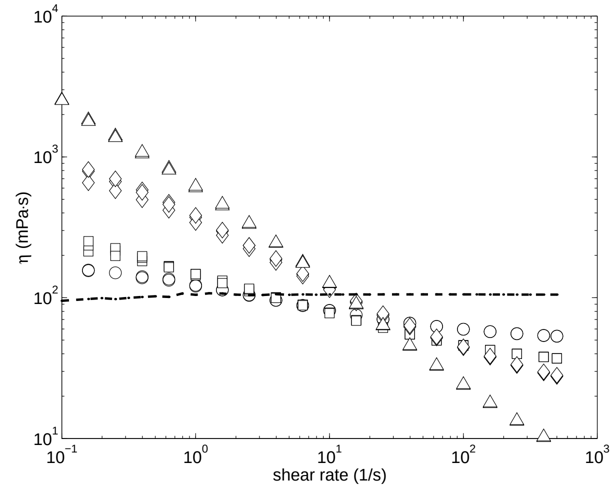

Figure 5.4: Flow curves of the thinning fluids. η: apparent viscosity, (−−) Newtonian fluid, (○) n=0.85, (□) n=0.76, (◊) n=0.55, (△) n=0.32.

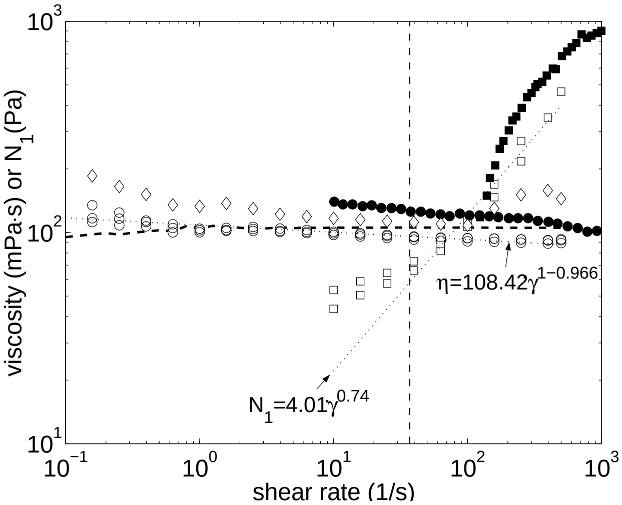

Figure 5.5: Flow curve of the Boger-1 fluid: (○) viscosity, (□) normal stress; (−−) viscosity of the Newtonian fluid; (●) viscosity of a Boger fluid reported by Pelletier *et al.* (2003): 830ppm of polyacrylamide ($M_w = 3.18 \times 10^6$g/mol) in a 80/20 (w/w) glycerin-water mixture, (■) normal stress of the Boger fluid of Pelletier *et al.* ; (◇) viscosity of the Boger fluid used in this work measured two weeks after the experiments. Vertical line: shear rate at which the velocity jump occurs, see section 7.1.1. The exponent in the viscosity equation (1-0.966) indicates the value of the flow index, $n = 0.966$.

et al. 2009). The normal forces (the absolute value of the first normal stress difference) of the thinning fluids, measured with the cone-plate geometry, reach a maximum value of 7 Pa at $100s^{-1}$ but decreased as the shear rate increased (data not shown). This behavior contrasts with the one shown by a viscoelastic fluid (a 0.2% polyacrylamide solution can reach a normal stress value of 100 Pa for the same range of shear rates) or an upper-convected Maxwell fluid where the normal stress grows as a function of $\dot{\gamma}^2$; clearly the behavior of our thinning fluids is very different. Note that the frequency value (inverse of the relaxation time) at which the dynamic moduli curves intersect in the shear thinning (xanthan) solutions is about two orders of magnitude higher than the corresponding value of the Boger-1 fluid. With these fluids (and with their rheological characterization) we were able to isolate, as much as possible, the thinning effects from the elastic ones over a wide range of characteristic flow times. The fluids were discarded after one week of experimental work.

A concentrated polymer solution, Boger-2 fluid, was also used in section 7.1.2. This solution was made with an associative polymer, HASE (hydrophobically modified alkali-soluble emulsion), dissolved in water (1.5%) adjusting the pH to 9.0 with a 0.1M solution of 2-amino-2-methyl-1-propanol (Soto *et al.* 2006, Mendoza-Fuentes *et al.* 2009). At this pH the polymer chains become expanded allowing the hydrophobic groups of the chain to associate intra- and intermolecularly. The flow curve can be seen in figure 5.7. This concentrated polymer solution presents a Newtonian behavior over a wide range of shear rates. Note that for the same shear rate values, the normal forces are higher in the Boger-2 fluid than in the Boger-1 fluid. As the viscosity of this fluid is highly increased by the

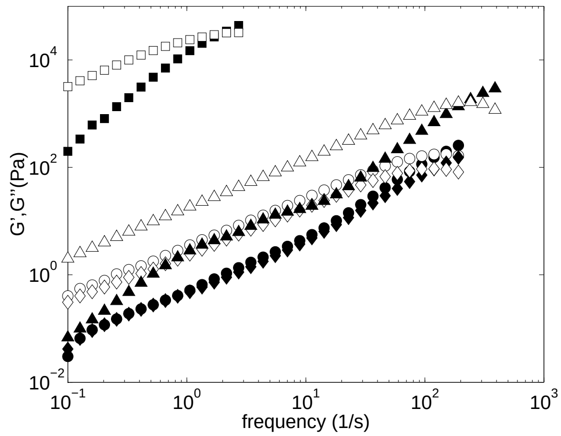

Figure 5.6: Dynamic moduli of three shear thinning solutions and the Boger-1 fluid. Filled symbols: elastic modulus G'; empty symbols: loss modulus G"; (○) n=0.85, (◊) n=0.55, (△) n=0.32; (□) dynamic moduli of the Boger-1 fluid. For the estimation of G' and G" the procedure followed by Calderas *et al.* (2009) was used.

hydrophobic associations among polymer chains, the value of the parameter c is very high ($c > 2000$).

.

5.3 Bubble size and velocities measurements

For the measurements of the mean bubble diameters, $\overline{d}_b$, and the mean bubble velocities, $\overline{U}_{SW}$, a high speed camera (*MotionScope PCI 8000s*) was employed. A recording rate of 500 frames/s and a shutter speed of 1/1000 was used. The camera was positioned 20cm below the liquid surface facing the larger side of the bubble column. Two different videos were obtained per experiment: one for the $\overline{d}_b$ measurements, where the camera was placed 120cm from the bubble column (using a 105mm objective lens) and another for the bubble velocity measurements, where the camera was placed a little bit farther, 180cm from the bubble column (using a 60mm objective lens, see fig. 5.1). Diffuse back light was used, with a light source placed at 90° from the camera direction and reflected by a panel. The video frames were analyzed using a conventional image processor software (Matlab ©, see figure 5.8). For bubbles having ellipsoidal shape, the equivalent mean bubble diameter $\overline{d}_b$ was calculated using the measurement of the short and long diameters of the elliptic bubble projections:

$$\overline{d}_b = (\overline{d}^2_{MAX}\overline{d}_{MIN})^{1/3} \tag{5.1}$$

where $\overline{d}_{MAX}$ is the larger bubble diameter and $\overline{d}_{MIN}$ the shorter bubble diameter. In some bubbly flows an equivalent mean cluster diameter was also measured. Although clusters shapes are highly irregular, an estimation of its size was made using equation 5.1, now taking the longer and shorter diameters of the cluster. The reported $\overline{U}_{SW}$ values were the average of the vertical component of the velocity vector. About 100 measurements were done for each experimental condition. When bubble aggregates appeared, the velocity

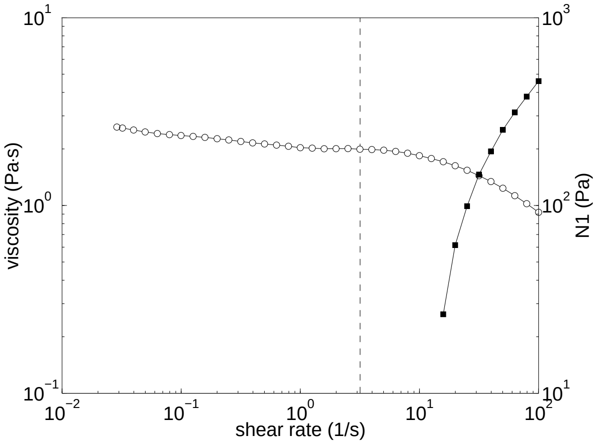

Figure 5.7: Flow curve of the 1.5 % HASE (Boger-2) fluid. Empty symbols: viscosity η; filled symbols: normal stress $N1$, vertical line: shear rate at which the velocity jump occurs, see section 7.1.2.

of individual bubbles located at the periphery of the clusters was measured; these were more easy to recognize than the bubbles located in the interior of the cluster. In the case of the elastic fluids, bubbles can acquire an inverted teardrop shape. In those cases, the Pappu's theorem was used to compute the volume V:

$$V = 2A\pi r_{centroid} \tag{5.2}$$

where A is the half of the projected area of the bubble, considering its axis of symmetry, and $r_{centroid}$ is the length between the axis of symmetry and the centroid of A.

For the case of the bubble pair experiments, the bubbles were followed by the camera mounted on a vertical rail activated by a DC motor (Sámano 2011). The velocity of the motor was regulated with a DC power supply. A recording rate of 60 frames/s was used. The image sequence obtained with the camera was binarized using a threshold value computed according to the Otsu's method provided by Matlab ©. As the pictures were taken by a moving reference frame, we used a pattern of circles, glued on the side of the column, to calculate the displacement of the camera in between frames; once the displacement of the camera was known is was possible to compute the absolute displacement of the bubbles. This procedure consisted of two parts: first a pair of consecutive images (j and $j-1$) are selected from the sequence. Then the same circle of the reference pattern is identified in each image and the position of its centroid is calculated. After doing this, the reference position is taken from the first image; hence the location of the bubbles is determined and their evolution from one frame to the next one. This procedure is repeated for the entire image sequence. In this manner, the uncertainty in locating the bubble position is minimized eliminating problems due to vibration of the camera and changes in lighting. The velocity of the bubbles at the image j was calculated using a central difference scheme. The distance between bubbles was directly computed from the images.

The velocity and size of isolated bubbles were also measured covering a bubble volume range from 0.1 to $100 mm^3$. Such measurements were done in a cylindrical column with

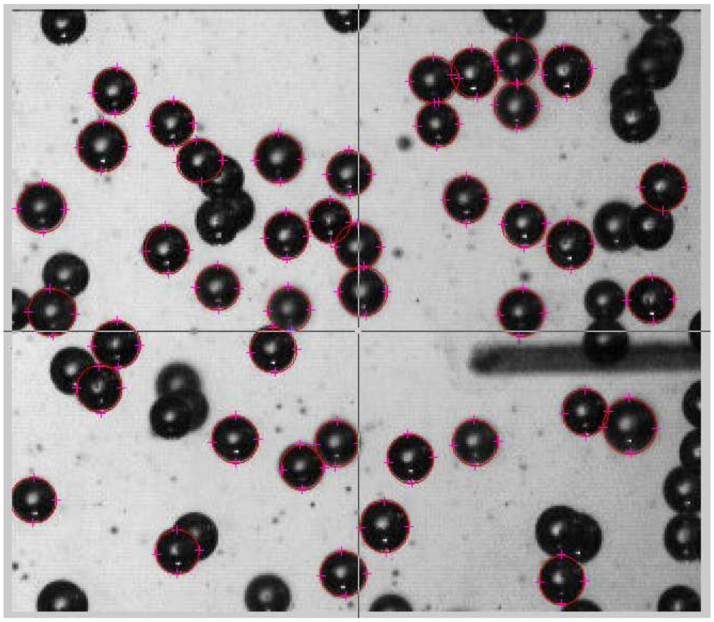

Figure 5.8: Image of the bubbles being recognized by a semi-manual algorithm. Four points over the bubble surface are selected and used for the computation of the equivalent diameter. For the estimation of the vertical velocity, the linear distance marked by a bubble through all the image window (an average velocity) was measured.

an inner diameter of 9cm equipped with a bubble dispenser similar to the one used by Soto *et al.* (2006).

In some flow conditions, the liquid velocity field was also obtained. This was done with the Particle Image Velocimetry (PIV) technique. The PIV technique in 2D is explained in detail elsewhere[7]. It consist in projecting a laser sheet (*NEW WAVE Research*) on the flow perpendicular to the direction of the camera (*Megaplus Camera, Model ES 1.0*). The liquid is seeded with tracer particles (10μm of rhodamine colored particles) so the movement of the liquid can be reconstructed computing (*FlowManager v4.6, Dantec Dynamics*) the displacement of the particles between two light pulses.

---

[7] *www.dantecdynamics.com*

Chapter 6

Results: Shear thinning inelastic fluids

The results are presented in two parts: one for the thinning fluids and the other for the elastic ones. Also, for each case there are three sections: single bubbles, bubble pairs and bubble swarms. Although this scheme presents the results in an orderly way, it does not necessary represent the time evolution of the project. The results presented in this chapter have been published in two papers (Vélez *et al.* 2011a and Vélez *et al.* 2011b).

6.1 Single bubbles in thinning fluids

The values of the drag coefficient, C_d, of the individual bubbles as a function of the Reynolds number, Re, are shown in figure 6.1. The Reynolds number and drag coefficient were calculated using equations 1.17 and 1.29 and using the power law model for the viscosity:

$$\eta = k\left(\frac{2U_{SI}}{d_b}\right)^{n-1} \tag{6.1}$$

In addition to the common functional dependence of the drag coefficient in the Reynolds number within the laminar flow regime, we can also observe that the experimental C_d values found for the thinning fluids are higher than those found for the Newtonian fluid. This increase of the drag coefficient with the thinning behavior has been already reported by theoretical (Hirose & Moo-Young 1969, Bhavaraju *et al.* 1978a) and experimental (Bhavaraju *et al.* 1978a, Haque *et al.* 1988) studies for the creeping and small but finite Reynolds regimes. Note that for the Newtonian fluid the Oseen wake is already seen at $Re \sim 7$. Although our fluids are not totally free from elastic effects (see section 5.2), the fact that a velocity jump discontinuity was not observed supports the statement that the elastic effects were very small indeed.

Figure 6.1 also includes some numerical results for single bubbles. Noticeable differences between the experimental and numerical results for the Newtonian fluid were seen below a Reynolds number of one, where the numerical drag values approach the Hadamard prediction (due to the prescribed slip condition at the bubble surface). Note that the agreement between the experimental and numerical values for the Newtonian

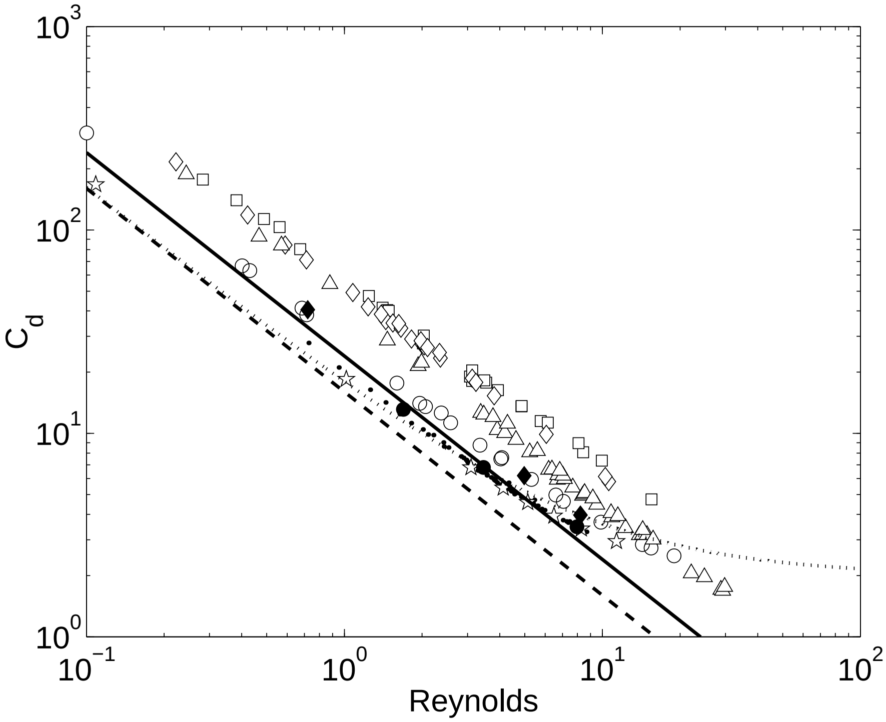

Figure 6.1: Drag coefficient as a function of the Reynolds number for the single bubbles. Experimental values: (·) Newtonian fluid, (○) n=0.85, (□) n=0.76, (◊) n=0.55, (△) n=0.32; Numerical values: (⋆) Newtonian fluid, (●) n=0.85, (⧫) n=0.55; (−) Stokes prediction, (−−) Hadamard prediction, (...) Oseen correction for a fluid sphere $C_d = 16/Re + 2$.

fluid is good (points and stars in figure 6.1, maximum error around 3%), indicating that the spatial resolution and the computational domain size were adequate. For the thinning fluids, it was found that the numerical terminal velocities were in all the cases higher (25% in the $n = 0.85$ fluid up to two times the experimental velocity in the $n = 0.55$ fluid) than those obtained in the experiments. The use of the Carreau model[8] gave the same results. It is not clear if this difference is due to the choice of a definition of the apparent viscosity (eq. 6.1), or due to other effects such as the time that molecules take to attain a random orientation (zero-shear viscosity) after deformation or because there is an adsorption of the polymer molecules on the bubble surface thus changing the boundary conditions. Zhang *et al.* (2010) found better agreement between their numerical and experimental values (using the same constitutive equations as in this work but with other test liquid and without addition of salt), although it seems that their error increases as the thinning behavior increases and the Reynolds number was close to zero. In the following we will see that in spite of this inaccuracy of the numerical results, the essence of bubble pairing is still captured by the simulations.

In figure 6.2 the drag coefficient of the single bubbles rising in different shear-thinning liquids is presented in a different manner. The experimental and numerical drag coefficients were normalized by their Newtonian counterparts ($n = 1$) to form the ratio $Y(n)$:

$$Y(n) = \frac{Cd_{thinning}}{Cd_{Newtonian}} \tag{6.2}$$

The ratio $Y(n)$ has been used by several authors (Hirose & Moo-Young 1969, Bhavaraju *et al.* 1978a, Rodrigue *et al.* 1999a) to investigate the drag force in shear-thinning fluids. The theoretical values obtained by Rodrigue *et al.* (1999a) and Bhavaraju *et al.* (1978a) are shown in this figure as well as the experimental results obtained by other authors. The assumption of clean spherical bubbles was used in both theoretical studies for creeping flow; also both studies used a perturbation method. The only difference between them was the way of expanding the second invariant of the rate of deformation tensor $\dot{\gamma}$. Following the standard notation for the drag coefficient used by these authors, the experimental and numerical $Y(n)$ values for very low Re flows ($Re < 1$) were calculated using the Stokes and Hadamard solutions respectively:

$$Y(n)_{exp} = \frac{Cd_{thinning}}{Cd_{Newtonian}} = \frac{\dfrac{4d_b g}{3U_{SI}^2}}{24/Re} = \frac{d_b g Re}{18U_{SI}^2} \tag{6.3}$$

and

$$Y(n)_{num} = \frac{\dfrac{4d_b g}{3U_{SI}^2}}{16/Re} = \frac{d_b g Re}{12U_{SI}^2} \tag{6.4}$$

Theoretical, numerical and experimental results show the same trend: as the thinning behavior is increased (decreasing n) the bubbles experience more drag than their Newtonian counterparts. These observations can be interpreted as follows: the maximum shear

---

[8] The Carreau model is $\eta = \eta_\infty + (\eta_o - \eta_\infty)(1 + [\lambda\dot{\gamma}]^2)^{(n-1)/2}$, where η_o is the zero-shear viscosity value, η_∞ the viscosity at high shear rates, λ a time constant and n the flow index.

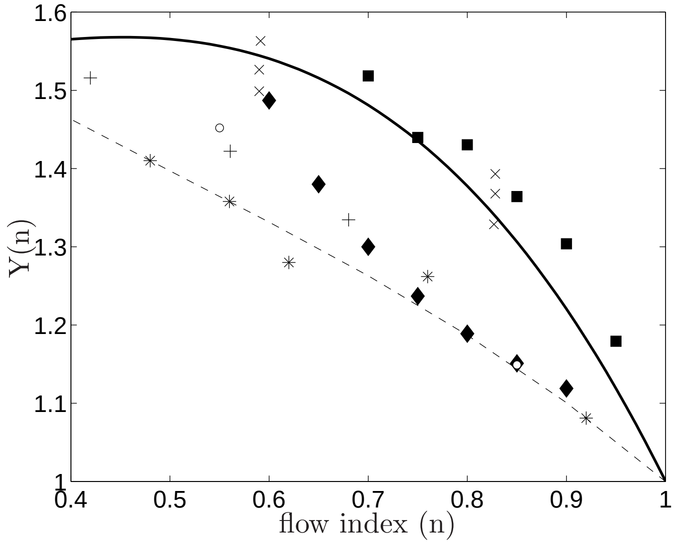

Figure 6.2: Drag coefficient ratio Y(n) as a function of the flow index. Numerical results: (■) $0.6 < Re < 1$, (◆) $7 < Re < 9$. Theoretical predictions: (−) Bhavaraju *et al.* (1978a), (−−) Rodrigue *et al.* (1999a). Experimental values: (○) this work $0.4 < Re < 1.2$, (×) 0.1 and 0.15% carbopol solutions from Bhavaraju *et al.* (1978a), (∗) 0.1-2.0% CMC solutions, $Re < 6$ from Haque *et al.* (1988), (+) 0.1-1.0% carbopol solutions with trietanolamyde, Re=3 from Chehata (2004).

rate experienced by the liquid is about U_{SI}/r, therefore the minimum viscosity value is approximately $k(U_{SI}/r)^{n-1}$ (note that for the drag estimation the equilibrium equation between buoyancy and drag forces was used and this expression do not need a viscosity value). For the single bubble case and at low Re numbers the shear rate decreases with the distance from the bubble, which in shear-thinning fluids result in higher viscosity values. The total effect is the increase of the resistance of the bubble motion, which can be seen by an increase of the pressure drag coefficient (see the C_{Dp} values in Table 4 of Dhole *et al.* 2007, $Re < 50$) which lessen the effect of the reduction of the friction drag term that occurs as n decrease (this component of the total drag is actually negligible for bubbles without surface active agents).

Other simulations with higher Reynolds numbers ($Re\sim 8$) were also conducted; the corresponding $Y(n)$ values are also shown in figure 6.2. In this case, since the Re number is not small the Hadamard prediction cannot be used and a direct comparison with the theoretical values (Hirose & Moo-Young 1969, Bhavaraju *et al.* 1978a, Rodrigue *et al.* 1999a) cannot be made. Therefore, to calculate the value of $Y(n)$ the drag of the thinning fluid was divided by the value attained by its Newtonian counterpart using the same physical parameters but changing the flow index value to one, leaving the same viscosity value at the characteristic shear rate U_{SI}/r. The $Y(n)$ values were thus calculated as:

$$Y(n) = \frac{Cd_{thinning}}{Cd_{Newtonian}} = \left(\frac{U_{SI_{Newtonian}}}{U_{SI_{thinning}}}\right)^2 \tag{6.5}$$

The results have the same trend as in the low Re case, that is, the drag increases with the thinning behavior. Zhang *et al.* (2010) made a similar comparison of their numerical terminal bubble velocities obtained with thinning and Newtonian fluids. In order to make the comparison they changed the value of the flow index (similar to what was done here) but considering a constant zero-shear viscosity value. These authors found that the terminal velocity of bubbles rising in thinning fluids was higher than the corresponding Newtonian case.

6.1.1 Wall effects

It is clear that the velocity of the bubbles will be reduced by the arrest of the fluid motion at the walls of the container: if the distance between the bubble and the wall is reduced, the decrease of the rise velocity will be higher. The correction of the rise velocity due to the proximity of the wall can be known using the method of reflections (the zero-velocity of the wall is reflected in the bubble velocity, and viceversa, see Happel & Brenner 1991). For creeping flows, there is an equation (Faxen equation) used to estimate such velocity correction:

$$\frac{U}{U_\infty} = 1 - \frac{r}{R}\left[2.1044 - 2.088\left(\frac{r}{R}\right)^2 + ...\right] \tag{6.6}$$

where U_∞ is the rise velocity without wall effects, r the bubble radius and R the radius of the container. We may wonder now how much is the rise velocity reduced due to the proximity of the wall in the experiments and calculations shown here. To answer this, several simulations were run in the ALE code varying the ratio of the bubble and column radius r/R . The results for the Newtonian fluid ($Re \approx 1$) are shown in figure 6.3. We can see that the walls of the bubble column, even the ones forming the shortest width, produce a small effect on the bubble velocity (rising in the center of the column) for $Re > 1$. The wall effects will be more pronounced in the cases were $Re < 1$; however, the Faxen's correction will only be around 7% since the single bubbles were released in the column having $R/r \approx 30$. Even more, we can expect that the wall effects will be reduced when the thinning behavior is increased, according to Mena *et al.* (1987). The notion of the velocity correction due to wall effects is important in the study of single bubbles but irrelevant (or difficult to address) for the case of bubble swarms. In that case, the general trend is that the bubbles rising close to the walls will move more slowly than the bubbles rising in the center of the column.

6.2 Bubble pairs in thinning fluids

6.2.1 Two-bubble interaction: vertical alignment

Let us first consider the numerical results. Two identical spherical bubbles were placed one above another, with a center-to-center separation of 4r using the same physical properties as the ones used in the single bubble simulation with $Re{\sim}8$. Upon start of the simulation, both rise and in time the lower bubble catches up with the leading one. When the bubbles reached a certain gap separation distance, two $Y(n)$ values (equation 6.5) were calculated, one for the trailing bubble (comparing the bubble velocities of the Newtonian and thinning

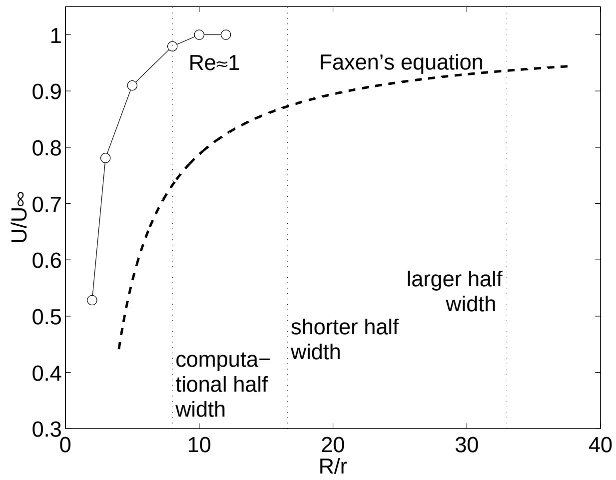

Figure 6.3: Wall effects on the bubble velocity ratio U/U_∞. (∘) numerical results for the Newtonian fluid, $Re \approx 1$; (− − −) Faxen's equation for creeping flows; the vertical lines refer to the half of the distance between the largest and shortest widths of the bubble column (the largest half width almost coincides with the radius of the column used to released single bubbles, see Soto *et al.* 2006), and the half of the computational width.

fluids) and another for the leading one. The results for two separation distances, $0.1r$ and $0.5r$, are shown in figure 6.4. In this figure we can see that as the bubbles become closer to each other, the trend seen for single bubbles changes: the $Y(n)$ values fall slightly below one. This means that two bubbles rising one after the other in a thinning fluid experience less resistance than their Newtonian counterparts. This behavior is inherent to the way the thinning fluid simulations were conducted. As previously said, the apparent viscosity corresponding to a characteristic shear rate U_{SI}/r of the single bubbles was fixed for both, the thinning and Newtonian cases. When for both a second bubble is added, the shear rate is increased in both fluids, the difference being that in the thinning case a zone with a lower viscosity near the bubbles will appear (see figure 4.2). The comparison made between the single bubble and bubble pair is similar to that made by Singh & Denn (2008), in the sense that the comparison depends on how the fluid properties are initially defined and serve as input information. For example, in this study single bubble and bubble pair simulations were done using the apparent viscosity calculated at the characteristic time of the single bubble. However, this is an arbitrary numerical procedure since one can also define the reference viscosity for two bubbles (considered as a single one with the equivalent volume). The important point here is that, when the apparent viscosity between the Newtonian and its Newtonian counterpart is held constant (this might be very difficult to do experimentally), two bubbles rising in a thinning fluid will rise faster than in the Newtonian fluid, unlike the single bubble case.

The shear rate formed around a bubble or a pair of bubbles can be visualized using the numerical code. In figure 6.5 the shear rate fields are shown for the thinning fluid with $n = 0.5$ ($10 < Re < 16$). The shear rate attained around the bubble pair is clearly higher (up to four times) than that appearing in the single bubble case. As can be

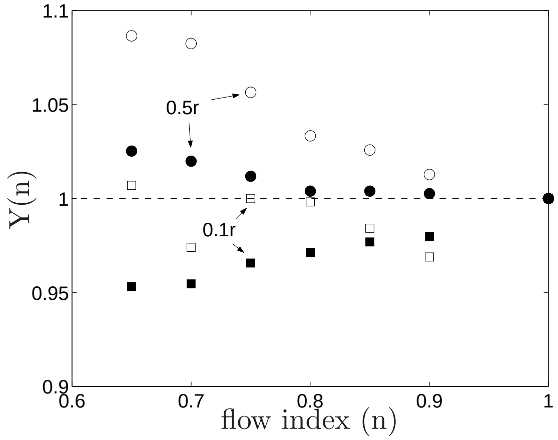

Figure 6.4: Drag coefficient ratio Y(n) as a function of the flow index for the in-line bubble pair; filled symbols: trailing bubble, empty symbols: leading bubble; (□) gap separation distance of $0.1r$, (○) gap separation distance of $0.5r$. As the bubble velocity was obtained from the average between the velocities at the top and bottom nodes of the bubble boundary, the minimum seen in the leading bubble for $0.1r$ could be due to bubble surface deformation.

expected, the zone with the higher shear rate surrounds the bubble pair, forming a single "jacket", when the bubbles become very close each other. Note that the numerical code is also capable to reproduce the axial elongation of the trailing bubble prior to contact. The so called "equilibrium position" between two in-line bubbles, reported by Yuan & Prosperetti (1994), was not observed for either the experimental and numerical tests.

The center-to-center separation distance between the bubbles as a function of the time is shown in figure 6.6 for the three bubble sizes used in this work. The experimental and numerical results are both shown using the dimensionless distance $d^* = \delta/r$ and the dimensionless time $t^* = t(U_{SI}/r)$, δ being the separation distance between bubble centers. In the following d_s^* is also used on several occasions and refers to an edge-to-edge or gap separation between bubbles. Three stages can be observed similar to the drafting-kissing-tumbling scenario reported for settling solid particles (Happel & Pfeffer 1960). The first one (drafting) corresponds to the approaching of the trailing bubble towards the leading one. This stage is characterized by an almost constant negative slope of the $t^* - d^*$ curve, meaning that a constant approach velocity occurs. Note that when the Re number is increased (viscosity gradients become less important) the initial slope has the same value regardless of the value of the flow index (figures 6.6b and 6.6c). The numerical simulations for these early times t^* are in good agreement with the experimental results. The second stage (kissing) can be easily identified by the change of the initial slope. The contact of the bubbles is accompanied by an elongation of the trailing bubble followed by a slight contraction of both bubbles due to the collision. The third stage (tumbling or not-tumbling) is the one that marks the difference between Newtonian and non-Newtonian liquids. Concerning shear-thinning fluids, small and medium size bubbles ($d_b = 2.1mm$ and $2.8mm$) rising in the $n = 0.5$ fluid, and small bubbles rising in the $n = 0.85$ fluid, remained together after contact. The bubble pairs in these cases either maintained a

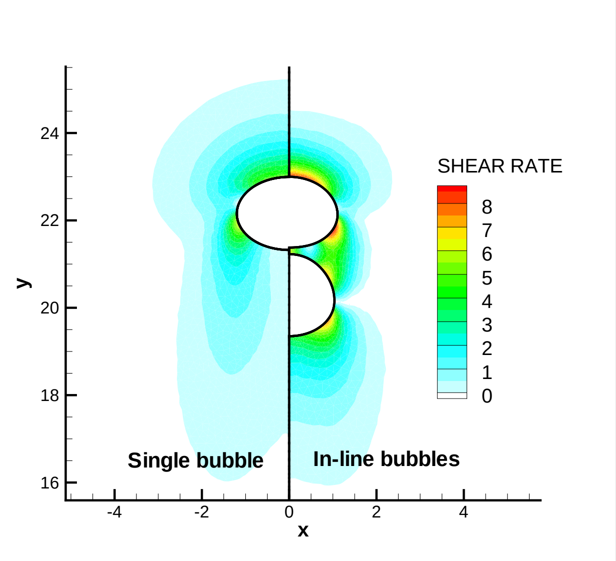

Figure 6.5: Shear rate contours obtained for a single bubble and an in-line pair rising in the $n = 0.5$ fluid. The values were taken at the same time (t*=5) for both the single and bubble pair. The initial separation of the bubbles was $4r$. The shear rate was estimated using the formula inside the square brackets of equation 4.3 and normalized by the characteristic time r/U_{SI}.

vertical orientation (not-tumbling) or an orientation with a certain angle, switching their relative position as they ascended (figure 6.7b). In the rest of the cases the bubbles turned to the horizontal position after contact and separated (tumbling), as shown in figure 6.7a.

The dimensional analysis of this section will be discussed in section 6.3.6 to link it with the results obtained in bubble swarms. The condition for bubble pairing (or clustering, in the case of bubble swarms) needs to fulfill certain conditions of inertia and bubble deformability. For practical purposes, one can draw a line of a constant Morton number in a Eo-Re plot to delimit the conditions of bubble pairing (clustering) and free bubbles. This “critical” Morton number seems to be of the order of 10^{-3} (see section 6.3.6). Concerning the Newtonian fluid, it was found that two bubbles rising in tandem at low Re ($0.4 < Re < 1.3$) also form a stable doublet (figure 6.6a). This contrast with the results obtained below (section 6.3) where for the same fluid and bubble size bubble pairing was not seen in bubbly flows. This indicates that bubble clustering in Newtonian fluids at low Re is greatly influenced by the amount of gas fraction (Cartellier *et al.* 1997). The fact that two bubbles rising in a Newtonian fluid can form a stable doublet supports the hypothesis that two *deformable* bodies moving in a fluid at low Re will prefer to move as a single body being surrounded by a common flow field. The deformability condition is emphasized since for rigid particles the pairing described here was not observed, even at low Re numbers (Happel & Pfeffer 1960). This apparent contradiction supports, in fact, the general tendency found in section 6.3.6: for a given Eötvös number, bubbles tend to form clusters if the Re number is low; on the other hand, for a given Re, bubbles tend to form clusters if the Eo number is high (more deformable bubbles). This argument is not

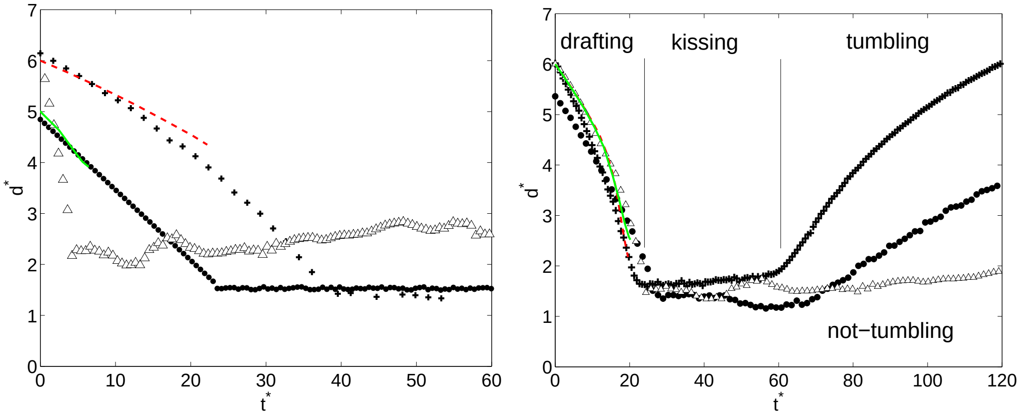

(a) small bubbles (b) medium bubbles

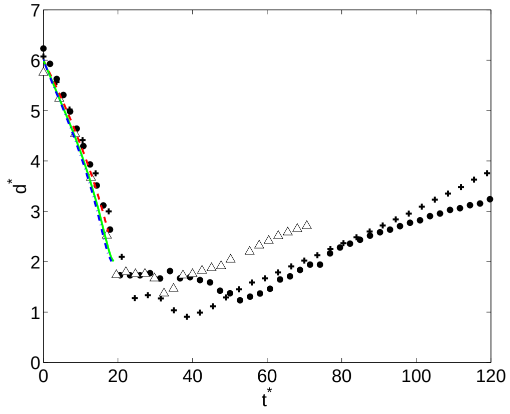

(c) large bubbles

Figure 6.6: Center-to-center dimensionless distance as a function of the dimensionless time of two bubbles released in tandem. The initial separation distance was approximately 6r. (a) $d_b = 2.1mm$, $0.45 < Re < 4.5$, (b) $d_b = 2.8mm$, $2 < Re < 6.4$, (c) $d_b = 3.6mm$, $4.8 < Re < 13.1$. Experimental results: (+) Newtonian fluid; (●) $n = 0.85$ fluid; (△) $n = 0.55$ fluid. Numerical results: (red line, $- - -$) Newtonian fluid; (green line, $-$) $n = 0.85$ fluid; (blue line, $.-$) $n = 0.55$ fluid (numerical results for this fluid using the smaller and medium bubble sizes are not shown due to the large computational time needed to complete the simulations). The computational domain size used for the Newtonian fluid with the smaller bubble ($Re \sim 1$) was $16r \times 70r$.

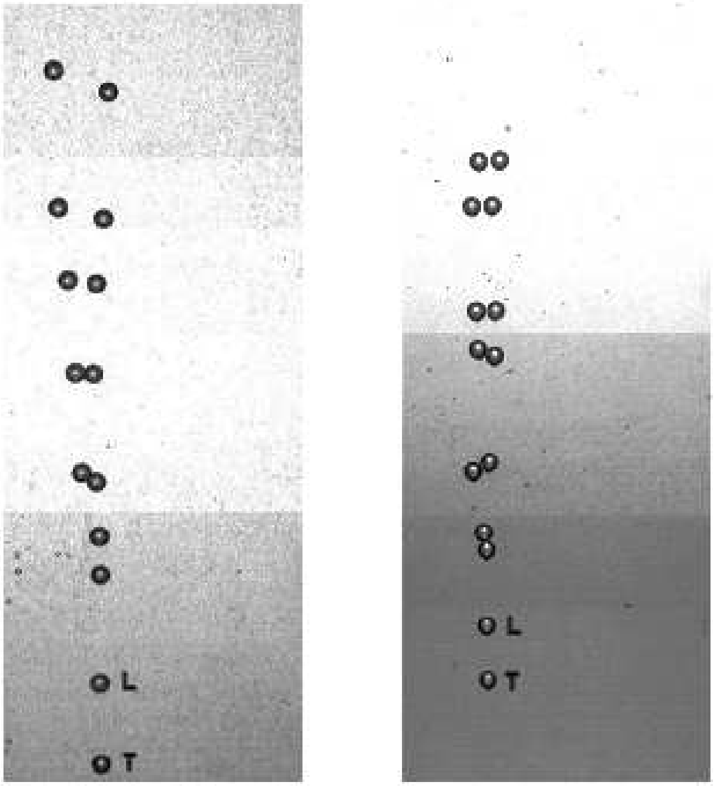

(a) Newtonian, Eo=0.9, Re=1.3 (b) n=0.55, Eo=0.7, Re=4.5

Figure 6.7: Non consecutive snapshots of the bubbles position taken with the movable camera. The bubble size is 2.8mm. The size of the image is approximately $7 \times 17 cm^2$. The Δt between shots is 0.5s. (L) leading and (T) trailing bubbles. The indicated Re number corresponds to the maximum value reached by the bubbles.

new: it was already reported by Manga & Stone (1993, 1995) for Newtonian fluids.

Figure 6.6 suggests that the thinning effect during the drafting process can only be observed at low Re numbers, that is to say, when the rate of approach of the trailing bubble is dependent on the flow index (figure 6.6a). Using the experimental velocity of the bubbles, we can compute the ratio of the drag coefficient of the trailing bubble Cd_T to the leading one Cd_L as:

$$\frac{Cd_T}{Cd_L} = \left(\frac{U_L}{U_T}\right)^2 \tag{6.7}$$

where U is the instantaneous velocity of the bubbles. The drag ratio at a separation distance of $\delta = 4r$ for different values of the flow index n is shown in figure 6.8. The data with $0.4 < Re < 4.5$ (small bubbles) confirms the observation that the mean drag of a bubble pair is less than its Newtonian counterpart, unlike the single bubble case. Such effect is nevertheless seen only at low Re values. As inertia is increased, the decrease of the drag with the flow index is more subtle.

In the case when the tumbling stage appears, the value of the drag ratio Cd_T/Cd_L becomes almost one (the separated bubbles attain the velocity of a single one). This can be seen in figure 6.9 with the Newtonian and $n = 0.8$ fluids. In this figure the experimental drag ratio Cd_T/Cd_L for the medium bubble size was plotted as a function of the dimensionless time. The values of the Newtonian fluid correspond to the case shown in figure 6.7a. For the case when the bubbles continued traveling as a pair (figure 6.7b, $n = 0.55$ fluid), the evolution of the drag ratio is very different (filled circles in figure 6.9). In this case, the movement of the bubbles forming the pair produces an oscillatory behavior of the drag ratio Cd_T/Cd_L: when the trailing bubble catches the leading one, the pair turns towards the horizontal alignment due to the pressure directed against the bubble motion. This horizontal arrange is nevertheless not stable because it leads to the separation of the bubbles (Legendre *et al.* 2003), which in turn causes a passage form low to high viscosity zones as the characteristic shear rate will decrease. A possible configuration is then a diagonal alignment. The bubble located at the front will cause a reduced viscosity path, hence the bubble in the back will be accelerated, reaching the bubble at the front and passing it. The process is repeated again. A similar periodic movement has been observed for the case of groups of settling particles formed by three (experimental results, $Re < 0.2$) or four bodies in Newtonian flows (numerical results, $Re \ll 1$), see the works of Jayaweera *et al.* (1964), Hocking (1964), Manga & Stone (1995). However, the periodic movement observed here for the case of two bodies has not been observed in Newtonian fluids, neither for settling particles (Happel & Pfeffer 1960, Jayaweera *et al.* 1964) nor for ascending bubbles (this work). A periodic transverse movement between a pair of bubbles rising side-by-side has been observed in Newtonian flows (Sanada *et al.* 2009), but this occurs at $Re \sim 300$, which has very different hydrodynamics than those obtained at low Re. Hence, we believe that the oscillatory behavior seen in figure 6.9 is due to non-Newtonian effects.

Apart from the differences found during the tumbling stage, the drafting process observed in the different fluids is very similar, the most significant differences being those at low Re numbers. Figure 6.10 shows the bubble velocity ratio U_L/U_T as a function of the separation d^* for all the fluids and bubble sizes. The plot includes all the data prior to bubble contact ($\delta > 2r$). In spite of the data scatter, the trend is close to the analytical

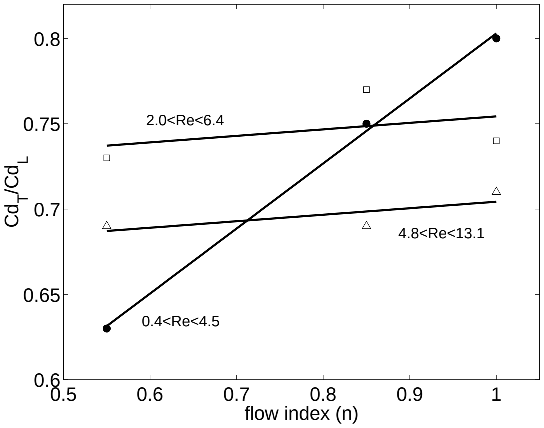

Figure 6.8: Experimental drag ratio Cd_T/Cd_L in terms of the flow index n. (●) small bubbles, (□) medium bubbles, (△) large bubbles. Separation distance between bubbles: $\delta = 4r$.

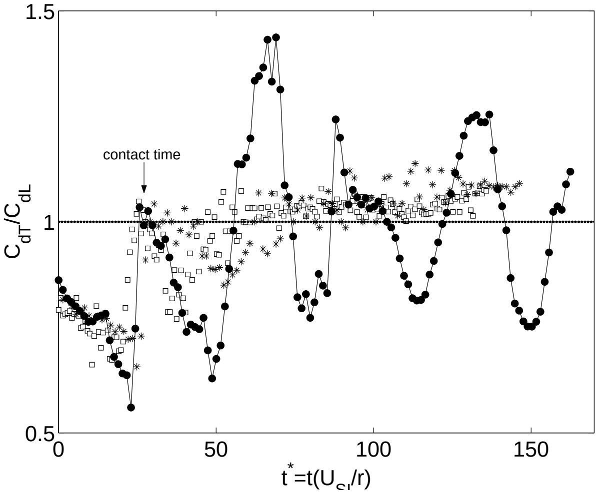

Figure 6.9: Experimental drag ratio Cd_T/Cd_L in terms of the dimensionless time t^*. (□) Newtonian fluid, ($*$) $n = 0.85$ fluid, (●) $n = 0.55$ fluid. The bubble diameter is $d_b = 2.8mm$.

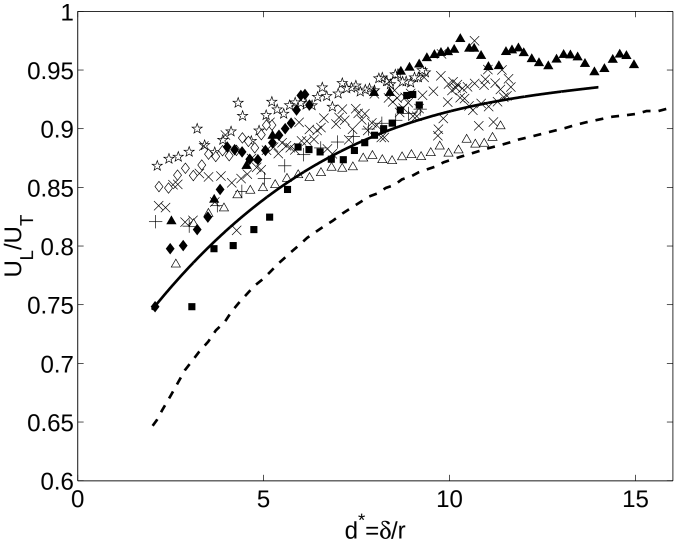

Figure 6.10: Experimental velocity ratio U_L/U_T in terms of the dimensionless distance d^*. ($\star$) $d_b = 2.1mm$, Newtonian fluid, ($\times$) $d_b = 2.8mm$, Newtonian fluid, ($+$) $d_b = 3.6mm$, Newtonian fluid, ($\Diamond$) $d_b = 2.8mm$, $n = 0.85$ fluid, ($\triangle$) $d_b = 3.6mm$, $n = 0.85$ fluid, (■) $d_b = 2.1mm$, $n = 0.55$ fluid, (◆) $d_b = 2.8mm$, $n = 0.55$ fluid, (▲) $d_b = 3.6mm$, $n = 0.55$ fluid. ($--$) theoretical solution for rigid spheres (Stimson & Jeffery 1926), ($-$) theoretical solution for gas bubbles (Rushton & Davies 1973).

solution of Rushton and Davies (1973) for gas bubbles rising in a Newtonian fluid. This analytical solution was based on the theoretical study made by Morrison (1973), which took into account the velocity of the leading wake. The agreement of the experimental data with the theoretical prediction suggest that the principle of superposition is also valid for shear-thinning fluids. The deviation of the experimental values from the theoretical prediction at short separation distances ($\delta < 7r$) could be due to the fact that the analytical solution does not take into account higher order terms that captures the proximity of the two bubble boundaries.

6.2.2 Two-bubble interaction: horizontal alignment

As mentioned by other authors (Happel & Pfeffer 1960, Legendre *et al.* 2003), two bubbles rising side-by-side with $Re < 30$ will experience repulsion due to the high pressure between the bubbles due to converging streamlines. Here it was found, as in Wenyuan *et al.* (2009), that two abreast bubbles rising in shear-thinning fluids also follow this rule; however, the thinning condition can considerably decrease the rate of separation between bubbles. In figure 6.11 the separation distance d^* is shown as a function of time t^* for the small ($0.4 < Re < 1.3$) and large ($4 < Re < 7.5$) bubbles and for several initial separation distances d^*_o. The experimental values are included as well as the numerical results. In this figure we can observe that the separation distance between bubbles increases with time for most of the cases; nevertheless, it was found that the rate of separation decreases when the thinning behavior increases (there is hardly any separation in the $n = 0.55$

fluid). This behavior reveals that the low viscosity zone produced by the bubble pair weakens the repulsive force between the bubbles aligned horizontally and decreases the rate at which the two bubbles separate. Additionally, it can be seen that the slope of the curves slightly decrease as the initial separation is increased, revealing that the interaction is weaker for larger separations. The 2D numerical results showed the same general trend found in the experiments; however, the rate of separation was considerably higher. Other authors (Ekambara *et al.* 2005) have already reported important differences between 2D simulations and the experimental results. In this case, it seems that the disc-shaped bubbles overestimate the lift forces acting on each of their boundaries. A full 3D simulation would be needed to obtain a closer agreement with the experimental results.

Figure 6.12 illustrates simulations of the lateral separation in Newtonian as well as in a shear-thinning fluid. Note that the bubbles separate from each other in both cases. In a general way, the experimental and numerical results obtained in this section suggest that the thinning behavior is not capable to attract two bubbles rising parallel in a fluid, unlike what has been observed in viscoelastic fluids (Joseph *et al.* 1994, Hu *et al.* 2001). Gheissary and van den Brule (1996) observed an attractive behavior of two settling particles moving in a thinning fluid made with Carbopol. Nevertheless, it has to be pointed out that the fluids used by these authors had a viscosity above one thousand times that of water and presented a gel-like behavior. In this kind of fluids the shear-thinning behavior can be originated from the structure breakdown of the gel, as mentioned by the authors, giving place to a different behavior during the interaction of two bodies.

The instantaneous drag of the two bubbles rising side-by-side was calculated and compared with the single bubble value for the case of the $n = 0.85$ fluid. The drag value of each bubble was calculated using eq. 1.28:

$$\frac{Cd}{Cd_{single}} = \frac{V_z |\mathbf{v}|_{single}{}^3}{V_{zsingle} |\mathbf{v}|^3} = \frac{V_z V_{zsingle}{}^2}{|\mathbf{v}|^3} \tag{6.8}$$

The drag ratios for the left (the one formed at the central capillary) and right bubbles as a function of the horizontal distance d^* between bubble centers are shown in figure 6.13. The analytical expression found by Legendre *et al.* (2003) for two spherical bubbles rising side-by-side in Newtonian fluids for the limiting case of $d^* \gg 1$ and $d^* Re \ll 1$ is also shown. It can be seen that the drag ratio decreases as the bubbles became closer. This agrees with the general trend found in viscous dominated flows, where the liquid encounters less resistance in moving around the two bodies rather than passing in the gap between them. The pair will then move as a single body. As the separation distance is increased, the drag value tends to the single bubble one. The differences in the values between the left and right bubbles are due to the proximity of the wall and the appearance of a slight differences in the vertical position between bubbles. The fact that the experimental values for the $n = 0.85$ fluid are close to the analytical expression of Legendre and coauthors indicates that in the limit of $d^* \gg 1$ the effect of the thinning behavior is irrelevant and only contributes to the value of the Re number at which the bubbles move. The results presented here are also in qualitative agreement with the behavior found by Liang *et al.* (1996) for the case of rigid particles fixed in the space in an horizontal alignment.

It should be pointed out that the role of the lateral movement experienced by two abreast bubbles, described in this section, on the formation of clusters in bubbly flows is

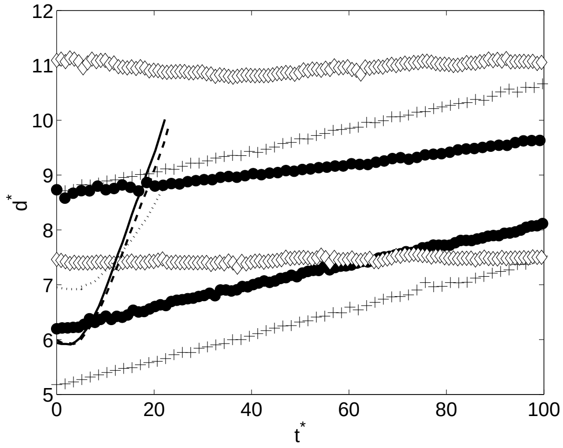

(a) small bubbles

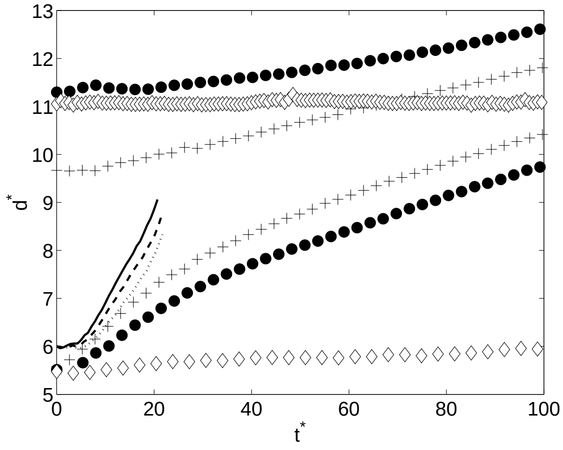

(b) large bubbles

Figure 6.11: Dimensionless distance in terms of the dimensionless time of two bubbles released side-by-side. (a) $d_b = 2.1$, $0.4 < Re < 1.3$; (b) $d_b = 3.6$, $4.0 < Re < 7.5$. Experimental results: (+) Newtonian fluid, (•) $n = 0.85$ fluid, (◊) $n = 0.55$ fluid. Numerical results: (−) Newtonian fluid, (−−) $n = 0.85$ fluid, (···) $n = 0.55$ fluid.

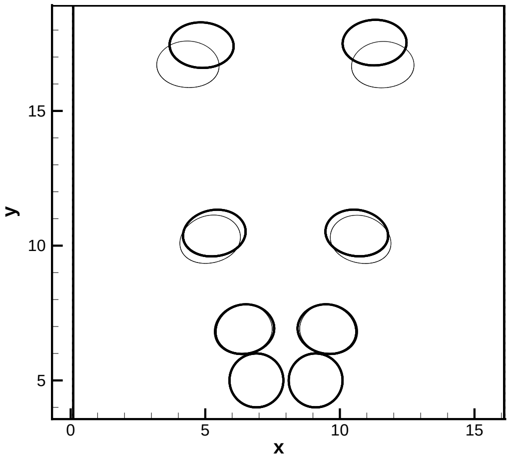

Figure 6.12: Numerical simulations of bubbles pair released side-by-side in the thinning n=0.55 fluid (thick lines) and its Newtonian (thin lines) counterpart. The bubbles positions in both fluids were taken at the same time. Initial separation distance: $\delta = 2.2r$, $Re \sim 10$.

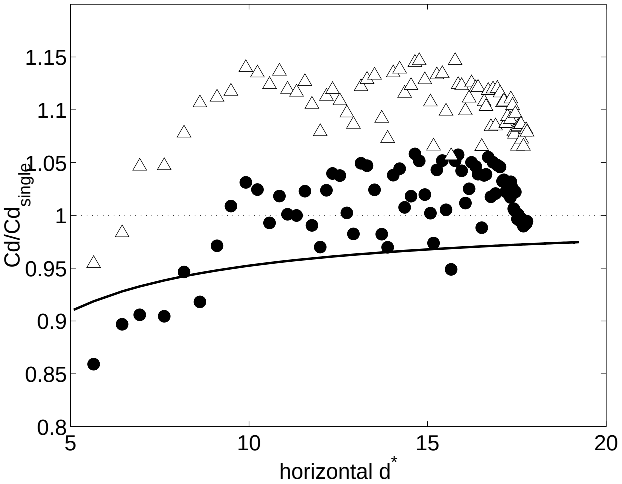

Figure 6.13: Drag ratio Cd/Cd_{single} in terms of the horizontal distance d^* for two off-line bubbles released in the $n = 0.85$ fluid. (•) left bubble, (△) right bubble, (−) $Cd/Cd_{single} = (1 + [1/2d^*])^{-1}$ (Legendre *et al.* 2003), $d_b = 3.7mm$, $Re \approx 3.5$

not as clear as the in-line alignment where, as we saw in section 6.2.1, two bubbles may or may not cluster depending on the inertia and deformability of the bubbles. Intuitively speaking, although a lateral repulsion between bubbles at low Re will give place to a higher homogeneity in the bubble spatial distribution on the horizontal plane, this effects will be secondary due to bubble attraction and pairing in the vertical plane and with angles $> 40°$. This issue will be discussed further in the next section.

6.2.3 Two-bubble interaction: varying the angle of approach

In this section the ALE code was used to gain some insight of the hydrodynamic interaction of a bubble pair which is not aligned horizontally nor vertically. For the experiments, although the production of bubbles to be aligned at an arbitrary angle (and preserving the same separation distance) is doable (consider, for example, a staggered initial arrangement), the necessary work to manipulate and change one arrangement for another could be rather arduous; hence, the use of simulations to predict the different behaviors is well justified. The case of the thinning fluid with n=0.55 and its Newtonian counterpart is shown in figure 6.14a, where the initial separation between bubbles centers was $4r$ and the initial angle (with respect to the horizontal) was 42°. The variation of the dimensionless distance between bubbles is plotted against the dimensionless time in figure 6.14b. The Newtonian case, now having an initial angle of 76°, is shown in figure 6.15. In figures 6.14a and b we can see that the bubbles rising in the Newtonian fluid approach each other but they do not make contact and eventually separate. This tumbling process happens even though the bubbles touch each other, as in figure 6.15. However, in the thinning fluid the trailing bubble catches up with the leading one and makes contact with it. After this drafting and kissing process the bubbles do not separate, the so-called tumbling motion is not observed. This behavior indicates that the bubbles are "forced" to stay in a low viscosity region, produced by a high shear rate zone, rather than separate from each other (the same trend was seen experimentally with the in-line bubbles during the non-tumbling stage). When the two interfaces come too close to each other (about $0.03r$), the local resolution becomes insufficient and the code eventually fails to converge. That was where the simulations in the thinning fluid ended.

To explore the effect of the degree of shear-thinning, other simulations were also carried out with the $n = 0.85$ and 0.76 fluids. The results are shown in figure 6.16 for three initial angles θ_o: 42°, 61° and 76° and for the same initial distance of $4r$. The Eo and Re numbers indicated in this figure were selected from the single bubble experiments in order to compare the simulations at a fixed value of Eo or Re.

First, it was observed that for the Newtonian counterpart cases, the bubbles separate after contact (as in figure 6.15). For these cases initial angles up to 88° were tested. In the shear-thinning fluids, the behavior at initial angle $\theta_o \geq 61°$ (figure 6.16c-f) is more or less the same as for bubbles in tandem (figure 6.7), that is; the two bubbles will form a doublet if $Mo \gtrsim 10^{-3}$ and will separate otherwise. For $\theta_o = 42°$, the greater horizontal separation weakens the interaction between the bubbles such that doublet formation is achieved only for the most shear-thinning fluid in figure 6.16b. The $n = 0.55$ fluid in figure 6.16a has a $Mo = 2 \times 10^{-3}$ but nevertheless experience separation. For the other cases in figure 6.16a and b, there is initial attraction between the two bubbles but they

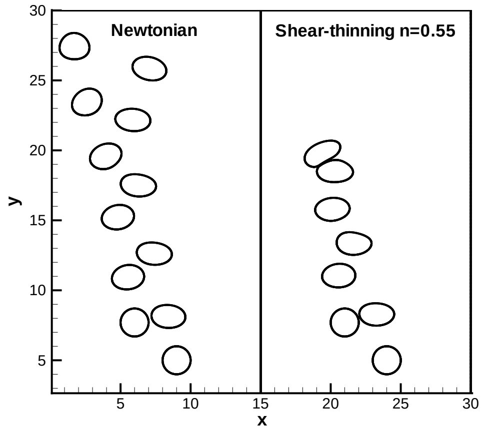

(a) bubble position

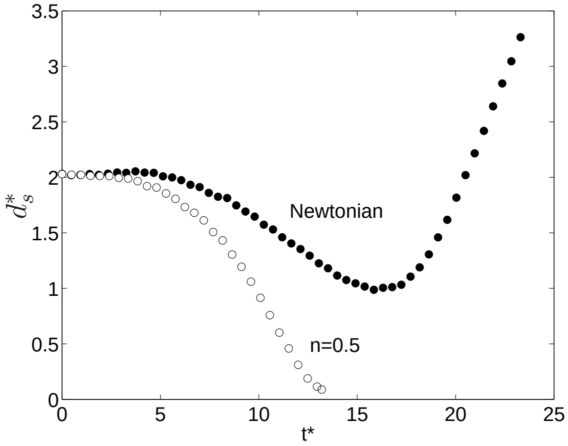

(b) dimensionless distance between bubbles as a function of time

Figure 6.14: Bubbles position and dimensionless separation distance for the n=0.55 fluid and its Newtonian counterpart. The initial separation distance between bubble centers was $\delta = 4r$, the initial angle was 42°, Re∼10.

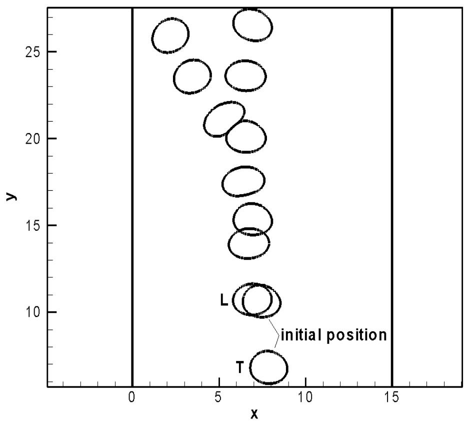

Figure 6.15: Bubbles position for the Newtonian counterpart of the $n = 0.55$ fluid having an initial separation distance of $\delta = 4r$ and an initial angle of 76°; (L) leading and (T) trailing bubbles.

eventually drift apart. The decrease of d^* in the $n = 0.55$ fluid (figure 6.16a) at $t^* = 20$ is due to the proximity of the wall.

In order to explain more in detail the results observed in figure 6.16, the viscosity profile around a single bubble was computed for the $n = 0.55$ and 0.85 fluids having the same Eötvös number (Eo=3). The results shown in figure 6.17 are similar to the ones obtained by (Zhang *et al.* 2010) for similar Re numbers ($Re \sim 10$). The maximum viscosity values agree well with the values given by the rheological data fitted with the Carreau model. These viscosity profiles were analyzed in two different ways: first, a definition of the viscosity gradient was introduced by computing the difference between the viscosity value on the bubble surface (η_{min}) and the viscosity value (η) located at two bubble diameters form the bubble surface. The curves of such viscosity gradient as a function of the angle formed with the horizontal plane is shown in figure 6.18a. Then, the η/η_{min} ratio for different distances from the bubble surface was obtained at a fixed angle. The results for an angle of 20° are shown in figure 6.18b. In figure 6.18a we can see that the viscosity gradient is not homogeneous around the bubble due to the presence of the bubble wake, which extends the region of non-zero shear rate and hence increase the region of viscosity recovery. On the other hand, near the horizontal plane, the decay of the shear rate occurs in a smaller region; therefore, the values of the viscosity gradient are larger.

For the cases shown in figure 6.18a the maximum viscosity gradient occurs at an angle of 20° in both fluids; however, the viscosity gradient found in the $n = 0.55$ at this angle is 5 times larger than the one found in the $n = 0.85$ fluid. The fact that the higher values of the viscosity gradient lie near the horizontal plane could explain why the fluids with higher thinning behavior can promote bubble clustering at lower angles, as we saw in figure 6.16. In this sense we think that the viscosity gradients produce a different stress distribution around the bubble than the one formed in a Newtonian fluid; such stress gradients will not work as a net driving force but will reduce the repulsive force created

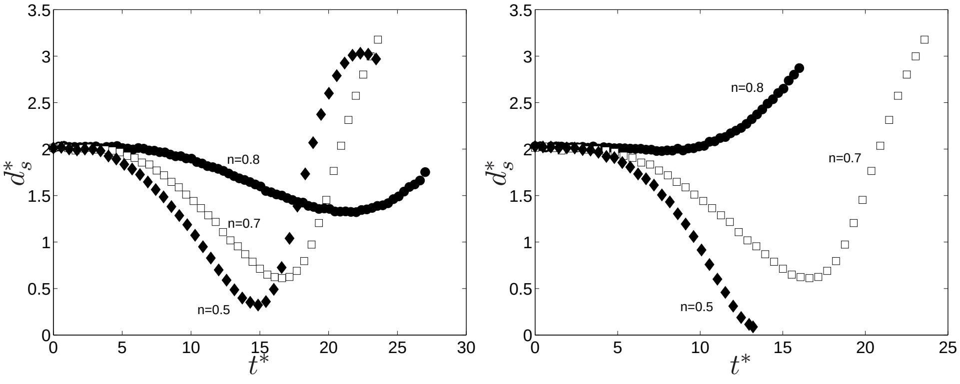

(a) $Eo = 2.6$, $\theta_o = 42°$ (b) $Re = 3.5$, $\theta_o = 42°$

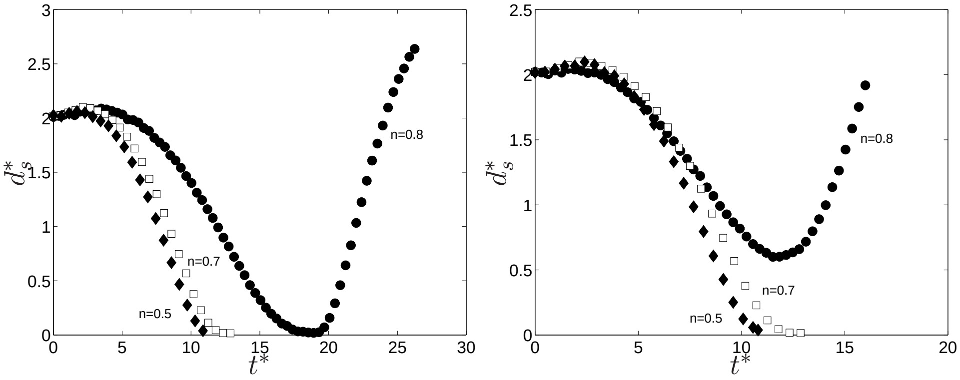

(c) $Eo = 2.6$, $\theta_o = 61°$ (d) $Re = 3.5$, $\theta_o = 61°$

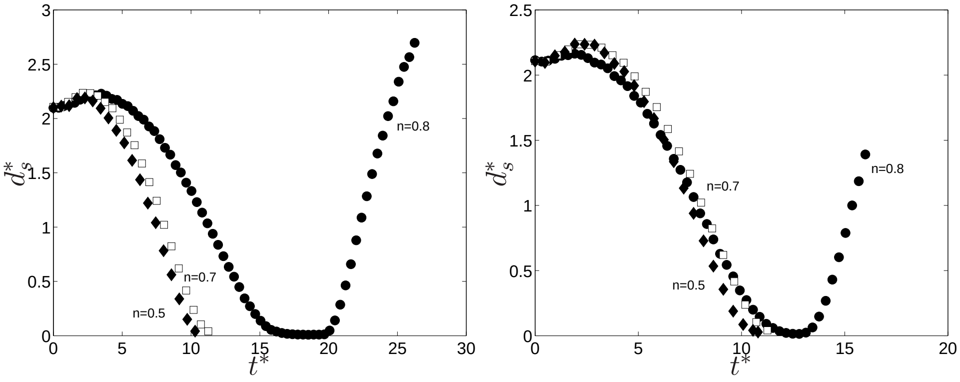

(e) $Eo = 2.6$, $\theta_o = 76°$ (f) $Re = 3.5$, $\theta_o = 76°$

Figure 6.16: Dimensionless distances d_s^* between bubble boundaries as a function of the time t^* for several thinning conditions and initial angles. (●)n=0.85, (□)n=0.76, (♦)n=0.55; initial distance, $\delta = 4r$. The Eo and Re numbers were selected from the experimental results for single bubbles. The experimental Mo number for the $n = 0.55$ fluid is 2×10^{-3} and for the other fluids is around 7×10^{-4}.

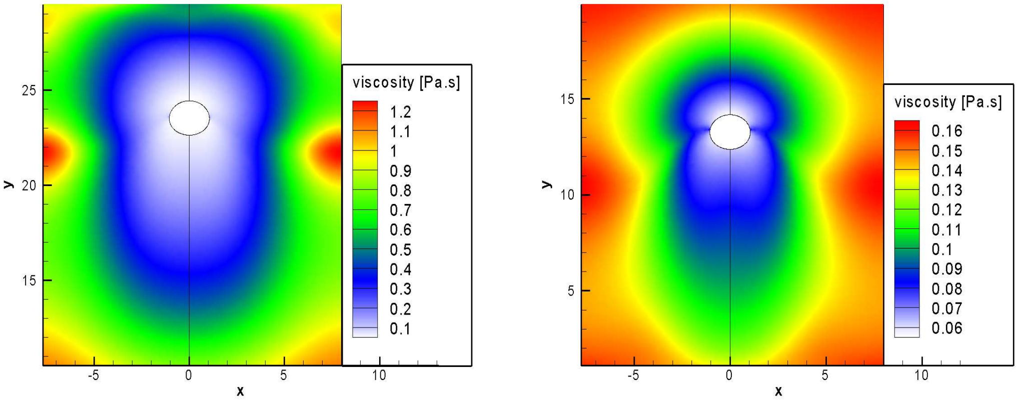

(a) single bubble $n = 0.55$

(b) single bubble $n = 0.85$

Figure 6.17: Viscosity contours around a single bubble immersed in the n=0.55 and 0.85 fluids. The viscosity was estimated when the bubbles achieved a steady velocity, $t^* = 7.6$, Eo=3. To avoid high viscosity values at low shear rates, an upper limit to the viscosity was introduced fitting the rheological data with the Carreau model.

by the bubble vortices, giving more chances to a bubble to be trapped by a leading wake. In figure 6.18b we can see how the viscosity ratio η/η_{min} increases with the distance from the bubble surface. The difference between the $n = 0.55$ (clustering condition) and 0.85 (free bubble condition) fluids is clear: in the case of the most thinning fluid the viscosity ratio reaches a value of 27, while in the other fluid reaches only a value of 3 at the same d_s^*. The viscosity ratio of the $n = 0.55$ fluid depicted in figure 6.18b acts as a viscosity "hole" which prevents another bubble to escape from the low viscosity region.

To compare the viscosity profile obtained for a single bubble with the one obtained for a bubble pair, the viscosity of two bubbles in contact rising in the $n = 0.55$ fluid was computed. The results are shown in figure 6.19. In this case we can see that the region of the lowest viscosity value ($\sim 0.05 Pa{\cdot}s$) comprises a larger area than the one occupied in the single bubble case. We may think then that the increase of the cluster size will increase the region of the lowest viscosity value but at the same time decrease the viscosity gradient. Note also that in the rear part of the bubble pair a region of high viscosity start to form due to the appearance of a toroidal vortex, in agreement with the work of Zhang *et al.* (2010).

From all these observations three mechanisms for cluster formation in shear-thinning fluids can be proposed: (*i*) The viscosity gradients that appear in the wake of a bubble ascending in a thinning fluid can reduce the repulsive force produce by the bubble vortices. This makes possible for a bubble to be caught in the wake of another bubble; if the thinning behavior increases, the critical angle of inversion of the lift force (from repulsion to attraction) is decreased, leading to a more effective clustering; (*ii*) if the Morton number is higher than 10^{-3}, the bubbles do not tumble after contact, a doublet is then

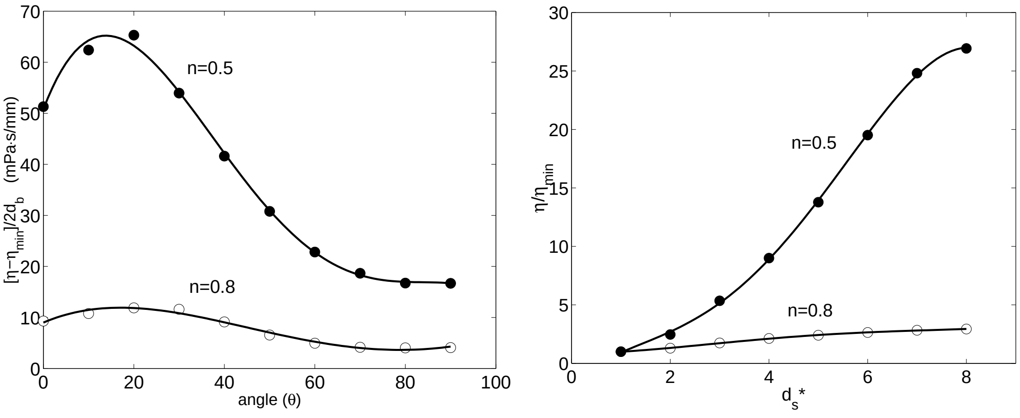

(a) (b)

Figure 6.18: (a) Values of the viscosity gradient as a function of the angle made with the horizontal plane for the bubbles presented in figure 6.17, $d^* = 5r$. (b) Viscosity ratio as a function of the dimensionless distance at a fixed angle of 20°.

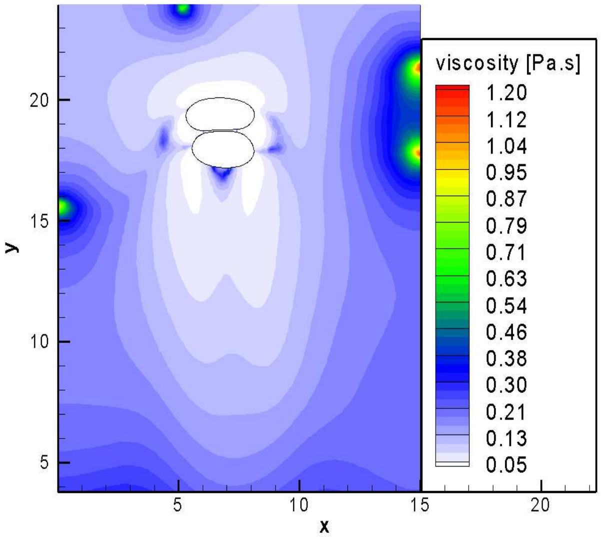

Figure 6.19: Viscosity contours around a bubble pair immersed in the n=0.55 fluid. The viscosity was estimated when the bubbles achieved a gap separation distance of $0.06r$, Eo=3. The initial angle was 76°. The Carreau model was again used as in figure 6.17.

formed; (iii) once two bubbles form a pair, they create a wake with lower viscosity which attracts more bubbles, leading to the formation of bubble clusters; however, the increase of the cluster size will decrease the viscosity gradients and the growth of the clusters will then stop. In this sense, we understand the formation of bubble clusters in thinning fluids as a mechanism that promotes the development of a Newtonian-like behavior; this is done by increasing the characteristic size of the flow and so decreasing the effective viscosity. The effect that the thinning property has on the interaction of two bubbles (reducing the repulsive force produced by the converging streamlines) has an interesting relation with the amount of the momentum transported in a thinning fluid. Let us consider first shear stress in a Newtonian fluid: $\tau = -\mu\dot{\gamma}$. This relation can be interpreted as the momentum transfer from high to low regions of shear, that is, the momentum per unit area and time is proportional to the negative of the velocity gradient (Bird *et al.* 1998). Hence, the momentum flux per unit time and volume, P, can be calculated as the gradient of the shear stress. Considering now the power law model $\tau = -k\dot{\gamma}^n$ we can calculate P as:

$$P = -\frac{\partial}{\partial y}(\eta\dot{\gamma}) \tag{6.9}$$

where $\eta = k\dot{\gamma}^{n-1}$. Therefore,

$$P = -\eta(n-1)\dot{\gamma}' - \eta\dot{\gamma}' \tag{6.10}$$

where $\dot{\gamma}' = \partial\dot{\gamma}/\partial y$. Comparing this expression with the Newtonian one, we have:

$$\frac{P}{P_N} = \frac{\eta}{\mu} + (n-1)\frac{\eta}{\mu} \tag{6.11}$$

In the case of a Newtonian fluid ($n = 1$), $P/P_N = 1$, as expected. However, if the fluid is shear-thinning, the ratio P/P_N decreases with n, that is, the momentum transport decreases as the fluid becomes more shear thinning. Hence, the viscosity gradients that appear around the leading bubble will reduce momentum transfer which, in turn, will tend to keep the trailing bubble trapped behind the leading one. We must make clear that the term "viscosity gradient" that has been used here actually refers to an additional function, in terms of a power of $\dot{\gamma}$, that has been included in the shear stress equation. This function is the one that deflects the stress transport from a linear function (the steady velocity profile in a thinning fluid submitted to shear flow will be similar to an unsteady velocity profile developed in a Newtonian fluid).

Regarding the formation of clusters, we need to point out that the cluster deformability (imagining the cluster as one big bubble) must also play an important role in the increment of the cluster size. As mentioned by Manga and Stone (1993, 1995), the increase of the deformability of the bubble surface leads to the formation of streamlines that propitiates the alignment and contact of two separate bubbles. The velocity field formed around a cluster can also trap additional bubbles that could contribute to its growth.

We have seen that for all the fluids studied here, including the Newtonian one, the trailing bubbles located within an angle of 40° with respect to the horizontal are not attracted by the leading one. On the contrary, bubbles located outside this region, that is, closer to the vertical axis, experience an attractive force that leads to the contact between

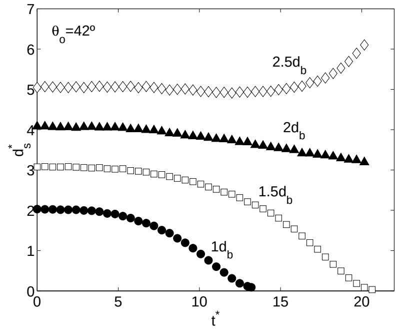

Figure 6.20: Dimensionless distance between bubble boundaries as a function of the dimensionless time (t*) for the $n = 0.5$ fluid and several separation distances. (●) $d_s^* = 2$, (□) $d_s^* = 3$, (▲) $d_s^* = 4$, (◊) $d_s^* = 5$, initial angle: 42°.

bubbles. This behavior is the opposite to that observed for high Re flows where, according to Biesheuvel & van Wijngaarden (1982), Kok (1993a) and Spelt & Sangani (1998), two bubbles positioned with angles between $35 - 54°$ experience attraction, while with an angle above $35 - 54°$, near the vertical axis, experience repulsion. The general description of the bubble motion in terms of the angle of approach in this work is in agreement with other experimental work (Wenyuan *et al.* 2009) for the case of the thinning fluids.

Finally, aside from the shear-thinning behavior and angle of alignment, we can expect the bubble-bubble interaction to be also dependent on the separation distance between bubbles. This effect is shown in figure 6.20 for a fixed flow index value and initial angle (n=0.55 and 42°). We can see that when the distance between bubbles surpasses two bubble diameters, the trailing bubble is no longer attracted by the leading one; in fact, they become nearly horizontally aligned and start increasing their separation distance. The same trend was seen with the other thinning fluids. These results suggest that in dilute bubbly flows, bubble clusters will not be formed due to the distance between them. Nevertheless, this condition is difficult to achieve experimentally, as we will see in the next section.

6.3 Bubble swarms in thinning fluids

Up to this point, we have learned that two bubbles rising in a thinning fluid can miss the tumbling stage under some flow conditions. It must be emphasized that the viscosity gradients are not capable by themselves to produce an attractive force (like the normal forces in an elastic fluid will do) between bubbles. What is happening is that once the bubbles are together due to collision or by means of a leading wake (which can be a "thinning wake"), the viscosity gradients can decrease the repulsive flow between bubbles, leading to the formation of a stable doublet. The numerical simulations suggest that the doublet will catch additional bubbles until the group produces a "Newtonian-like" flow in the surrounding liquid. In this section, we will see the formation of such bubble clusters. Also, the bubble velocity variance produced and the flow conditions necessary for they appearance are described. Before doing this, however, we need to revise some general issues on bubbly flows.

6.3.1 Bubbly flow regime and cluster formation

As pointed out by other authors (Buchholz *et al.* 1978, Schumpe & Deckwer 1982) the transition from bubbly to the heterogeneous regime, which is characterized by the presence of multi-dispersed bubble swarm (see the introduction), can be identified by a change in the slope of the gas volume fraction as a function of the superficial gas velocity. The slope of the curve changes (decreases) as a consequence of the change of the bubble volume. In figure 6.21 the gas fraction value is shown as a function of the superficial gas velocity for the Newtonian and a thinning fluid (n=0.85) for several bubble diameters. For both cases the mean bubble size produced by each capillary bank was practically the same. For the Newtonian case (filled symbols) the bubbles with the smaller $\overline{d}_b$ produce higher gas fraction values, as expected. The transition to the heterogeneous flow can be seen by the change of the linear slope of the curves for the three different bubble diameters. All the measurements reported hereafter in this paper were taken before the transition to the heterogeneous regime. The Φ_g values obtained for the thinning fluid are similar to the Newtonian case for 3.1 and 4.2mm bubble diameters; for the smaller bubbles (2.1mm) the gas fraction values are clearly below the Newtonian ones; this is due to the presence of bubble clusters, as we will see below. Additionally, note that the $\Phi_g = U_g/\overline{U}_{SW}$ relation for homogeneous bubbly flows produces a curve generally above the experimental values. This could be due to the fact that the liquid velocity was neglected from the Φ_g calculation. Other authors (Ulbrecht & Baykara 1981) have shown that the value of the liquid velocity $\overline{U}_L$ developed in the central plume of the flow (produced by the viscous bubble flow and not by the movement of the whole continuous phase) is also an important parameter for the estimation of the gas fraction. The relation $\Phi_g = \overline{U}_L U_g/\overline{U}^2_{slip}$ was proposed by these authors, where $\overline{U}_{slip} = \overline{U}_{SW} - \overline{U}_L$. According to this formula (and using an iterative procedure, such as *fzero* in $Matlab^{®}$), the estimated values of the liquid velocity in the central plume[9] is 0.8-2cm/s for the Newtonian fluid and 2.7-4.7cm/s in the n=0.85 fluid. These liquid velocity values have been experimentally measured, in fact, in Newtonian flows ($10 < Re < 40$, Palacios-Morales 2005).

Figure 6.22 shows images of the bubbly flows produced in the column. The images correspond to the Newtonian fluid and the shear-thinning fluid with n=0.55 for the smallest bubble size. The formation of large bubble aggregates in the thinning fluid is largely evident (figures 6.22c, 6.22d). The difference with the Newtonian case (figures 6.22a and 6.22b) is striking. While the orientation of such clusters is mainly horizontal, spheroidal clusters and small bubble chaining can also be seen. It is worthwhile to mention that the clusters are not static while rising through the fluid; on the contrary, they have a dynamic structure. A careful observation reveals that the bubbles move in toroidal trajectories, rising in the center and descending on the exterior part of the cluster. As the gas fraction increases, just before the regime transition, the bubbles embedded in such clusters inevitably coalesce and form large cap bubbles. A similar toroidal or periodic

---

[9] Although in this case the flow cannot be referred as a "central plume" since the bubbles were released from several capillaries and not just one, this term refers to the liquid motion in the central part of the column, discarding the liquid motion near the column walls.

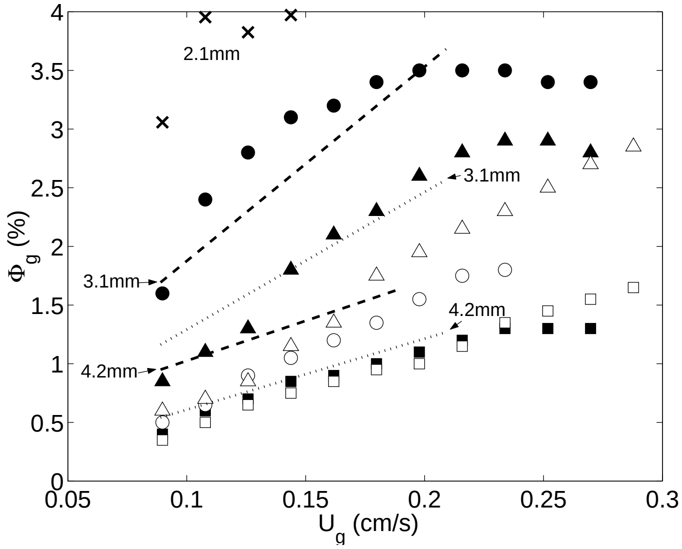

Figure 6.21: Gas fraction values as a function of the superficial gas velocity. Filled symbols: Newtonian fluid, empty symbols: n=0.85 fluid, (○) $\overline{d}_b$=2.1mm, (△) $\overline{d}_b$=3.1mm, (□) $\overline{d}_b$=4.2mm. The lines and the crosses refers to the values calculated according to $\Phi_g = U_g/\overline{U}_{SW}$: (×) Newtonian fluid with $\overline{d}_b$=2.1mm; (−−) linear regression ($R^2 > 0.95$) for the Newtonian fluid with $\overline{d}_b$=3.1mm and 4.2mm; (...) linear regression ($R^2 > 0.95$) for the n=0.85 fluid with $\overline{d}_b$=3.1mm and 4.2mm.

movement has also been observed in the case of settling particles forming clusters at low Re (Jayaweera *et al.* 1964, Hocking 1964). Nevertheless, besides the difference between the degree of deformation, such periodic movement seen in Newtonian fluids disappear as soon as inertia ($Re > 0.2$) or the number of particles (> 7) are increased. Figure 6.22 clearly shows that clustering in thinning fluids appears above these limiting factors.

6.3.2 Bubble size distribution

Figure 6.23 shows the histogram of the bubble diameter for the Newtonian fluid and the n=0.76 fluid; the plot shows data taken for each capillary bank. In both cases the curves show a narrow distribution of the bubbles diameters produced by the capillary banks indicating that the formation of nearly mono-dispersed bubbly flows was accomplished. In addition, it can be seen that the bubble diameter distributions are similar for both cases, indicating that the different fluids used in this work allowed the formation of bubbles with similar mean bubble diameters. The same behavior was observed in the other thinning fluids; the only exception was the $n = 0.32$ fluid with the smallest capillary diameter for which the mean bubble diameter was 36% higher than all the other cases.

6.3.3 Mean bubble velocity and drag coefficient

Figure 6.24 shows the ratio of the mean bubble velocity with the single bubble one as a function of the gas fraction; the three bubble sizes produced in the bubble column are included. The theoretical values reported by Gummalam and Chhabra (1987) and

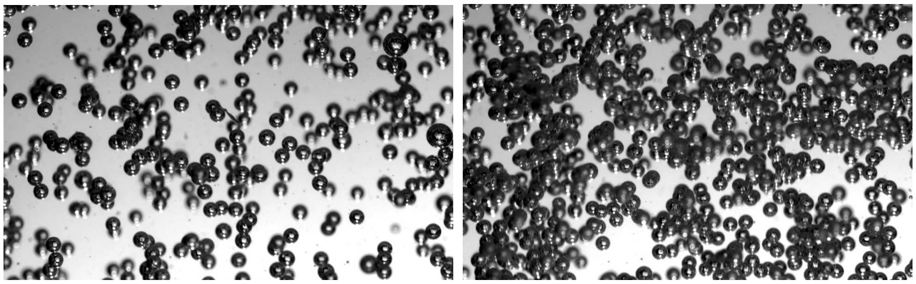

(a) Newtonian fluid, Φ_g=0.65%, Re=0.9, Eo=0.9 (b) Newtonian fluid, Φ_g=1.5%, Re=0.7, Eo=0.8

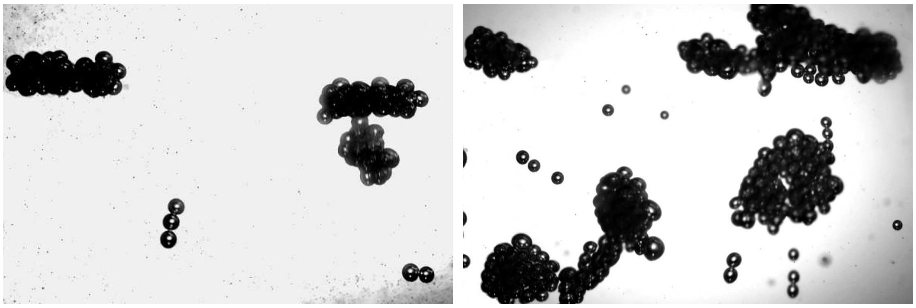

(c) n=0.55, $\Phi_g \sim 0.05\%$, Re=3.6, Eo=0.8 (d) n=0.55, Φ_g=0.65%, Re=3.0, Eo=0.7

Figure 6.22: Bubbly flow pictures taken at different gas fraction values for the Newtonian fluid and the n=0.55 thinning fluid. The magnification of the images are approximately the same. The image size is about 5x3cm. The bubble size (2.1mm) correspond to the one produced by the smallest capillary diameter. The Reynolds number was computed using the mean bubble diameter and velocity of the bubbly flow.

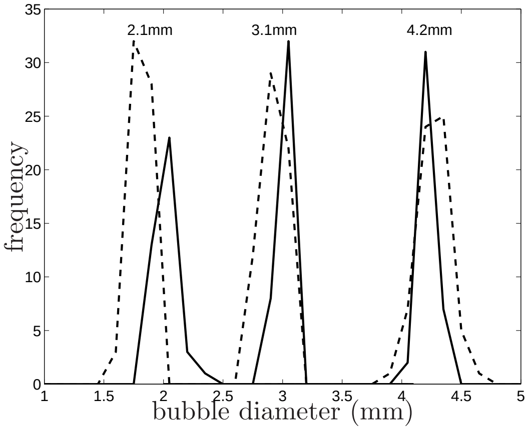

Figure 6.23: Histograms of the equivalent mean bubble diameters $\overline{d}_b$ for the Newtonian (−) and n=0.76 (−−) fluids produced by the three capillary banks; 15 classes were used to sort the bubble diameters. The frequency refers to the number of values found in each class.

Chhabra (1998) for creeping and high Re flows ($100 < Re < 300$) are also shown for their lowest flow index values and for their Newtonian results. The experimental and theoretical (see figure 2.3) results agree in the sense that the $\overline{U}_{SW}/U_{SI}$ curve has a positive slope for small gas fractions. This means that, unlike the Newtonian flows, the hydrodynamic hindrance produced by bubbles interactions does not produce a reduction of the bubble velocity with Φ_g; in the shear-thinning cases this effect is compensated by the reduction of the apparent viscosity produced by the local shear rate values. Hence, the Happel cell model used by Gummalam & Chhabra captures the basic nature of these flow types. This fact also agrees with the early results of Buchholz *et al.* (1978). The values of the gas fraction at which the maximum $\overline{U}_{SW}/U_{SI}$ value was observed in the experiments was, nevertheless, much smaller than the theoretical ones. In fact for $\Phi_g \geq 1\%$ the heterogeneous regime is observed, that is why measurements at higher volumetric flow rates or gas fractions (where the maximum theoretical values were found) are practically impossible to attain in a bubbly flow regime. Additionally, the experimental values of the velocities ratios were found to be much larger than the theoretical ones. As the bubble size decreases, the difference between the theoretical and experimental values increases (up to nine times for the case of the n=0.57 fluid, see figure 6.24c). Hence, the Happel cell model is not sufficient to explain the whole phenomenon. The effect which is not accounted for in this model is the appearance of bubble clusters (like those shown in figure 6.22c and 6.22d). These clusters are responsible for the high $\overline{U}_{SW}/U_{SI}$ values found in the experiments. The shape of the curves in figure 6.24 indicates that the clusters grow up to a certain size just before the transition to the heterogeneous regime. The last important difference between both results is that while in the theoretical data the velocity ratio increases monotonically with the thinning behavior (decreasing the flow index value), the experimental results do not necessarily follow this trend. For instance, in figures 6.24a and 6.24b the curves of the fluids with n=0.85 and 0.32 are closed to the theoretical ones while the fluids with n=0.55 and 0.76 are far from them due to the formation of clusters.

The values of the drag coefficient (in terms of a drag correction factor $X = C_d Re/24$) were also reported in the theoretical work of Gummalam and Chhabra (1987). Their results showed that the C_d increases with the gas volume fraction for $n > 0.4$, as is commonly observed, but decrease for index flow values below 0.4. In Chhabra (1998) the C_d values for $Re = 50$ were also reported. This author mentioned that the C_d increases with the gas volume fraction, obtaining again the common trend found in Gummalam & Chhabra (1987). In a recent numerical work of the same group (Kishore *et al.* 2008), where the Happel cell model was also used, the C_d values were found to increase with the gas fraction at the same n value although such increase was found to be negligible for $\Phi_g < 0.001$. In the present work an estimation of the C_d values of the bubbly flows were also obtained for low gas fractions. The C_d values were computed using equation 1.29 and the values of the mean bubble diameter and velocity of the flow. For comparison, the constitutive equation for D_d proposed by Ishii & Zuber (1979) was also used:

$$C_d = C_d(Re_{SI})\left(\frac{U_{SI}}{U_{SW}}\right)^2 (1 - \Phi_g) \qquad (6.12)$$

where the functional dependance of $C_d(Re_{SI})$ was obtained using the single bubble data

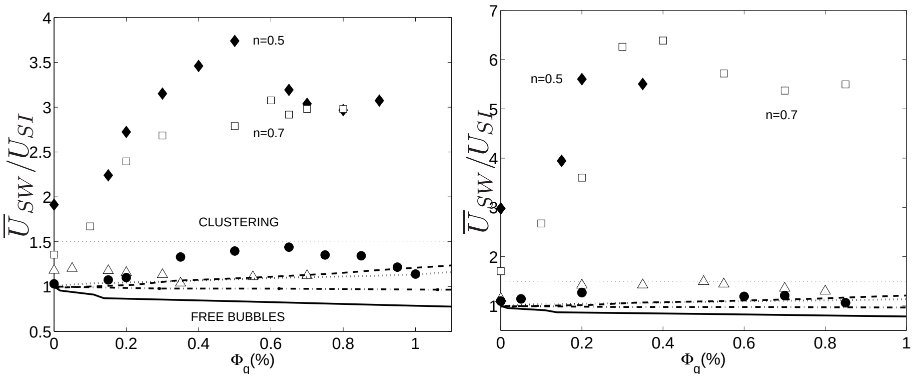

(a) $\overline{d}_b$=4.2mm (b) $\overline{d}_b$=3.1mm

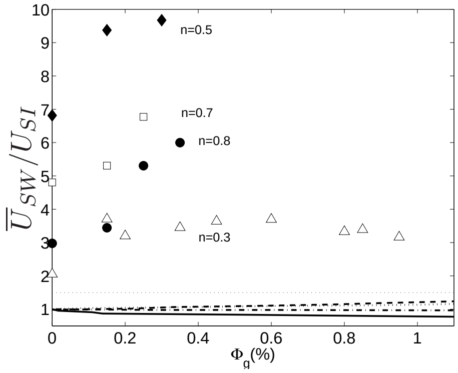

(c) $\overline{d}_b$=2.1mm

Figure 6.24: $\overline{U}_{SW}/U_{SI}$ ratio as a function of the gas hold up Φ_g for the three mean bubble diameters. (●) n=0.85, (□) n=0.76, (♦) n=0.55, (△) n=0.32, theoretical values (Gummalam & Chhabra 1987, Chhabra 1998): (−) creeping flow n=1.0, (···) creeping flow n=0.3, (-·-) $100 < Re < 300$ n=1.0, (−−) $100 < Re < 300$ n=0.2. The dotted horizontal line at 1.5 divides the free bubble and cluster formation regimes.

n	Φ_g	Re	C_d	C_d eq.6.12	C_d ref. Kishore *et al.*
0.32	0.001	10.3	3.9	4.2	
	0.002	10.9	3.6	3.9	
	0.003	10.9	2.8	3.6	
0.55	0.001	5.2	2.6	6.0	4.0
	0.003	5.8	2.3	5.3	
0.76	0.001	3.6	4.2	8.0	5.5
	0.002	4.2	3.3	6.5	
	0.007	4.3	2.8	6.0	

Table 6.1: Drag coefficient values for different thinning fluids and gas volume fractions. In order to calculate $C_d(Re_{SI})$ of equation 6.12 the respective bubble diameter obtained in the bubble column was used. The data of Kishore *et al.* (2008) correspond to the C_d values found for $n = 0.6$ and 0.8 and a gas fraction of 0.001.

for each fluid (figure 6.1). This equation was proposed considering a multiparticle system moving in one dimension in an infinite medium (absence of walls). The results are shown in Table 6.1.

It can be observed that the drag coefficients actually decreases as the gas volume fraction increases for the same fluid and Re number, unlike the general trend found by Kishore *et al.* (2008). Such decrease of the C_d is directly related to cluster formation and growth. Unlike the Newtonian fluids, where the C_d increases with the gas fraction, in bubbly shear-thinning fluids it decreases. It can be seen also that equation 6.12 and the numerical results of Kishore *et al.* both overestimate the values of the C_d because they do not consider interactions or associations among bubbles.

6.3.4 Cluster size

The equivalent cluster diameter $\overline{d_c}$ for one of the thinning fluids (n=0.76) is presented in figure 6.25 as a function of the gas volume fraction. In this plot the $\overline{d_c}$ values produced by the smallest and largest capillaries are shown both in dimensional and dimensionless form (scaled by the bubble diameter $\overline{d_b}$). The ratio $(\overline{d_c}/\overline{d_b})^3$ was used because it is directly proportional to the number of bubbles in a cluster. In this particular fluid clusters were observed for the three bubble sizes tested, that is, bubble clusters are formed no matter what the value of the $\overline{d_b}$ is. Also in this fluid we obtained more data of the cluster diameters before the heterogeneous regime occurred. For the $n = 0.55$ fluid the transition to this regime occurs at lower gas fractions. On the one hand we can observe in figure 6.25a that the cluster size and growth rate is the same for the two bubble diameters, suggesting that the size of the clusters is mainly determined by the fluid properties, channel width and the amount of available gas but not on the bubble size. On the other hand, it was verified (figure 6.25b) that the number of bubbles embedded in the cluster is larger for the case of the small bubbles than the larger ones. Additionally, it was found that the normalized standard deviation of the cluster size $(\sigma/\overline{d_b})$ is larger for the ones made with small bubbles (up to 123) in comparison to the ones made with the larger ones (up to 5), indicating that the clusters made with the small bubbles interchange bubbles more often with their surroundings.

6.3.5 Bubble velocity variance

We can expect that bubble cluster formation will affect the agitation levels in the gas; hence, a larger bubble velocity variance will be present in comparison with flows where no clusters are found. To verify this argument the bubble velocity variance was measured. The normalized values of the variance ($T_b/\overline{U}_{SW}^2$) for the thinning fluid with n=0.85 were determined for the three bubble diameters; these results are shown in figure 6.26. For this fluid no cluster formation was observed for the medium and large bubbles; clusters appeared only with the smaller bubble size (see figure 6.24). As can be observed, the normalized bubble velocity variances for the medium and large bubbles ($4 < Re < 14$) are in agreement with the values obtained by Martínez-Mercado *et al.* (2007) for a Newtonian fluid with similar Re values ($10 < Re < 30$). In the case of the smaller bubbles (2.1mm, with $1.7 < Re < 3.4$), where clusters are formed, the $T_b/\overline{U}_{SW}^2$ values surpass by nearly one order of magnitude the values achieved by the unclustered cases. This cluster-fluctuation relation seen at low Re numbers is very different from that expected in potential flows (Spelt & Sangani 1998). A common feature in high Re flows is that clustering is suppressed by bubble velocity fluctuations (Figueroa-Espinoza & Zenit 2005). In the present study, fluctuations are actually enhanced by the clusters. Such difference adds to the already large list of the contrasting behavior between inertial and viscous dominated flows. Similar $T_b/\overline{U}_{SW}^2$ values and behavior were obtained for the other thinning fluids.

It is interesting to note that the values of the bubble velocity variance found here for a range of $1.7 < Re < 3.4$ and thinning conditions are of the same magnitude as the liquid velocity variance found by Cartellier & Rivière (2001) for similar Re values ($0.66 < Re < 1.48$) and gas fractions in Newtonian fluids, although in their experiments the liquid phase was forced to flow in a co-current manner with the gas phase. Cartellier *et al.* (1997) observed that in these low Re flows the dispersion was composed by free bubbles, bubble pairs, some triplets and clusters composed by more than five bubbles; they also reported a gas concentration increase at the center of the column. As the volumetric gas flow rate was further increased, the gas fraction profile gained the classical saddle shape, that is, with wall peaked distributions, and bubble aggregates were dissociated. Although in the present work the types of bubble associations mentioned by Cartellier *et al.* (1997) in a Newtonian fluid was not observed, the $\overline{U}_{SW}/U_{SI}$ ratios obtained with this fluid with the smallest and medium bubble diameters were higher than one (up to 1.3) in the limit of zero gas fraction, contrary to that observed by Zenit *et al.* (2001), reveling a kind of long distance interaction between bubbles. In addition to this, the bubble velocity variance measured for the Newtonian fluid at low Re numbers ($0.6 < Re < 1.1$) also surpassed by nearly one order of magnitude the values of more inertia dominated flows (Martinez-Mercado *et al.* 2007, see figure 6.26).

From all this evidence one can argue that in viscous dominated bubbly flows (in both Newtonian and thinning fluids) the long range interactions promote the increase of the rise velocity of the bubbles comparing with the single bubble case. This kind of behavior is similar to the one seen with settling particles (Jayaweera *et al.* 1964, Hocking 1964). Other effects of these viscous flows could be the increase of bubble fluctuations, precisely due to the long range bubble interactions, and a net repulsion force between the

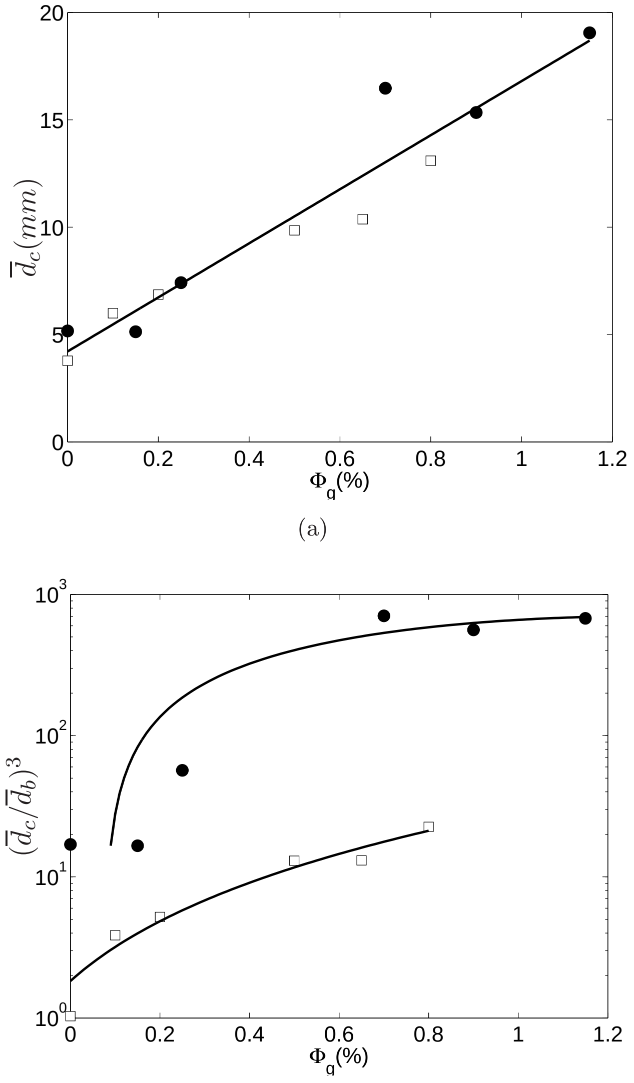

(a)

(b)

Figure 6.25: Mean equivalent cluster diameter $\overline{d}_c$ as a function of Φ_g for the n=0.76 fluid. In figure 6.25b the values are divided by the mean equivalent bubble diameter $\overline{d}_b$ and elevated to the third power. (•) $\overline{d}_b$=2.1mm, (□) $\overline{d}_b$=4.2mm. The lines are only visual aids.

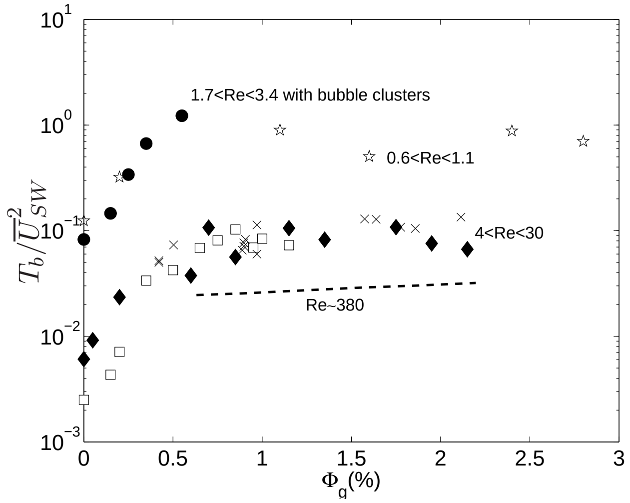

Figure 6.26: Bubble velocity variance T_b divided by $\overline{U}_{SW}^2$ as a function of Φ_g. Experimental values of this work: (●) $\overline{d}_b$=2.1mm, $n = 0.85$; (⧫) $\overline{d}_b$=3.1mm, $n = 0.85$; (□) $\overline{d}_b$=4.2mm, $n = 0.85$; ($\star$) $\overline{d}_b$=2.1mm, Newtonian fluid. Other experimental values: (×) data taken from Martínez-Mercado *et al.* (2007) with Newtonian fluids, (−−) data taken from Zenit *et al.* (2001).

bubbles and the column walls (Vasseur & Cox 1977), which could explain the abnormal gas fraction profiles obtained by Cartellier *et al.* (1997). Clustering in thinning fluids has, however, important differences with the one observed in Newtonian fluids, as we have observed through all this section and explained in section 6.2.3.

6.3.6 Conditions for cluster formation

As proposed earlier, bubble clustering seen in thinning fluids is a mechanism that these fluids have in order to decrease the viscosity gradients in the surrounding liquid. An expression capable to predict the size of a cluster for certain values of Φ_g and η (as a function of $2U_{(SW or SI)}/d_b$) can be proposed. This could be done in future works (perhaps, the clusters grow until the viscosity η_∞ in the surrounding liquid is achieved; this is just, however, an innocent proposition). What was done in this work was to recognize the conditions in which bubble clusters will appear. As we saw in section 6.3.3, the increase of the velocity ratio $\overline{U}_{SW}/U_{SI}$, due to bubble clustering, does not depend directly on the value of the flow index n. This means that a more thinning fluid does not necessarily induces bubble clustering. It was found that a combination of the values of the Reynolds and Eötvös numbers give the conditions for cluster formation. The value of the flow index is taken into account in the apparent viscosity included in the Re number. This kind of dependence of the forces acting on the bubbles with the flow index is in agreement with the results of Zhu *et al.* (2003), who worked with thinning fluids that were forced to pass through a fixed arrangement of rigid spheres. They found that the drag force experimented on a test particle does not depend on the values of the flow index but on the Reynolds number and the spacing between particles.

To identify the hydrodynamic conditions for which bubble clusters are formed, we can use an Eötvös-Reynolds plot for the single bubble cases (using figure 6.1). For the case of isolated bubbles the Eo-Re plot is often used to identify the shapes of the bubbles (Clift *et al.* 1978). Cluster formation can be identified by direct observation of the bubbly flow and also by evaluating the change of $\overline{U}_{SW}/U_{SI}$ with the gas volume fraction. When the velocity ratio was larger than 1.5, cluster formation was observed. In figure 6.24a, for example, bubble clusters are formed in the $n = 0.5$ and 0.7 fluids; in figure 6.24c all the thinning fluids formed bubble clusters since $\overline{d}_b$ was small. The relation $\overline{U}_{SW}/U_{SI} = 1.5$ only serves as a distinction between the condition where the velocity of the bubble swarms was higher than the single velocity but without the formation of clusters, as in the Newtonian fluid. Cluster identification was made mainly by simple observation. In the case of the $n = 0.32$ fluid with the smaller bubbles (2.9mm), cluster identification was not easy at gas fractions around 0.4%. At this value the clusters become progressively diluted by the whole flow. Nevertheless, we recognized these flows as part of the clustering condition since the values of $\overline{U}_{SW}/U_{SI}$ were above 1.5. Another parameter that can be used to recognize bubble clustering is the bubble velocity variance. As shown in section 6.3.5, bubble clustering increases considerably the velocity variance of the bubbles. In the bubbly flows presented in this work the normalized standard deviation $\sqrt{T_b/\overline{U}_{SW}^{\,2}}$ was about ±0.4 in unclustered flows while it reached up to ±5.0 when clusters were formed.

The result of this mapping is shown in figure 6.27; it includes the five fluids used in this work and considers clustering condition in bubble flows and the not-tumbling stage seen in the experiments of bubble pairs. We can describe this plot as follows: the data is separated according to the clustering (or not-tumbling) behavior, filled and empty symbols show flow conditions where clustering was or was not detected, respectively. For instance, a filled symbol was assigned to a Eo-Re point if for the same bubble diameter and liquid properties the bubbles clustered for a particular gas volume fraction. This mapping is easy to do because the gradual increase of the gas fraction produce only a slight increase of $\overline{d}_b$. A separation of the two regimes can be observed. Clearly, the clustering is observed when the viscous effects are more important than the inertial ones (small Re). Hence, as inertia increases it is possible to break the clustering behavior. Additionally, the deformability of the bubbles is also important. For a given value of Re, a flow with more deformable bubbles will tend to cluster more easily (as the Eo increases). The separation between the two regimes is given approximately by the iso-Morton line of 10^{-3}. Previously, a Morton value of 4×10^{-4} was proposed (Stewart 1995, Smolianski *et al.* 2008) as a transition indicator from non-coalescing flows to coalescing flows in Newtonian fluids. This suggest that the transition of non-interacting to interacting bubbles is a general condition for inelastic fluids, including the Newtonian and shear-thinning fluids.

The Mo number increases from top to bottom in a Eo-Re plot. The tendency to form bubble clusters increases with the Morton number. That is why the n=0.55 fluid, with the highest Mo number, has the biggest $\overline{U}_{SW}/U_{SI}$ values (see figure 6.24) followed by the n=0.76 fluid and finally by the n=0.85 and 0.32 fluids. We could infer from figure 6.27 that at very low Re numbers, in the creeping flow regime, the curves displayed in figure 6.24 will have the same trend as the theoretical ones, that is to say, the n=0.32 fluid will have the highest $\overline{U}_{SW}/U_{SI}$ values, as it will have the highest Morton number, followed by the n=0.55 and so on. Another way to interpret figure 6.27 is by stating

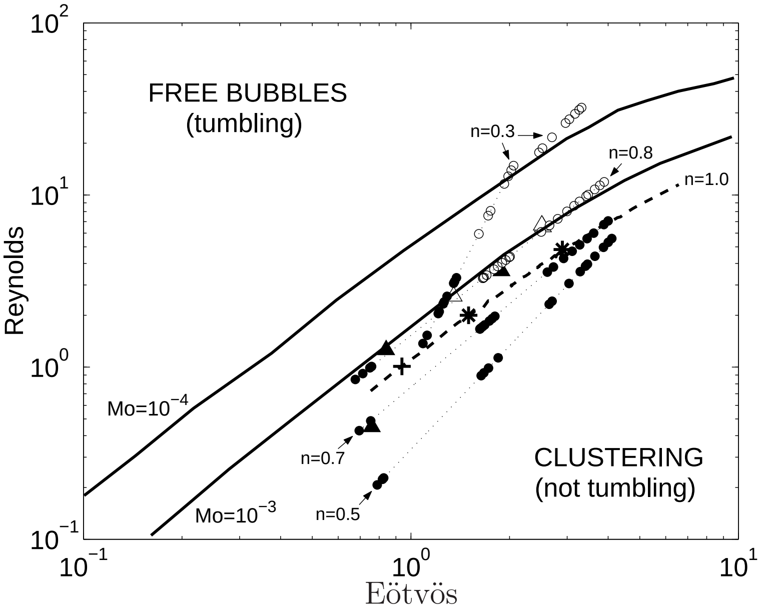

Figure 6.27: Cluster condition (not-tumbling stage) mapped in a Eo-Re curve of the single bubbles. (●) hydrodynamic conditions for bubble clustering, (○) hydrodynamic conditions for free bubbles, (▲, +) hydrodynamic conditions where the tumbling stage was not seen in the bubble pair experiments in the thinning and Newtonian fluids, respectively; (△, ∗) hydrodynamic conditions where the tumbling stage was seen in the bubble pair experiments in the thinning and Newtonian fluids, respectively; (−) $Mo = 10^{-3}$ and 10^{-4}, (−−) Morton line (3.6×10^{-3}) for the Newtonian fluid (in the Newtonian bubbly flow experiments no cluster formation was seen). The iso-Morton lines were taken from Clift *et al.* (1978).

that liquids having a high Mo number (high viscosity) are condemned to provoke bubble clustering. Fortunately, a thinning fluid can have the opportunity (depending on the bubble size) to scape from this regime since it does not follow a iso-Morton curve (see the $n = 0.3$ fluid). As discussed by other authors (Stewart 1995, Legendre *et al.* 2003), bubble interaction strongly depends on the bubbles wake and vortices structure, which in turn evolve as the Re number is increased or the bubble shape is changed. The degree of deformation of a bubble, measured with the Eötvös (or Bond) number is another important factor that enhances bubble alignment and coalescence, as explained by Manga & Stone (1993, 1995). In this work a maximum Eo number of 10 was reached. It would be interesting to investigate if bubbles with $Eo >$40 and $Mo > 10^{-3}$, in which according to Clift *et al.* (1978) the skirted and dimpled ellipsoidal-cap bubbles are formed, also form clusters in thinning fluids.

Chapter 7

Results: elastic fluids

In the previous chapter we learned that shear-thinning fluids (with negligible elasticity) are capable to produce larger bubble clusters much stronger than those observed in Newtonian flows. We additionally gained some insights of the mechanism involved in bubble pairing by using computational algorithms. Now is time to leave the thinning fluids aside and focus our attention in the elastic Boger-type fluids used in this work. Free bubbles and clustering conditions were also observed in these Boger fluids; however, we will see that the mechanism involved in the regime change is quite different from that proposed previously. Actually, the hydrodynamic conditions that resulted from the bubbly flow in the Boger fluids were below the $Mo \approx 10^{-3}$ correlation (so we could expect that these fluids will show bubble clustering for any Eo-Re combination). The condition change in these fluids is more drastic than that found in the thinning fluids (and so a little more easy to identify) and is related to the elastic effects on the bubble surface. Unlike the thinning fluids, the comparison of the experimental results with numerical simulations is limited. A few numerical results will be shown and the main limitations that the numerical codes have in simulating fluids with memory or elastic effects will be discussed. The results presented in this chapter also appear in two papers (Vélez *et al.* 2011c and Vélez *et al.* 2011d).

7.1 Single bubbles in Boger fluids

In section 5.2 the rheological characterization (based on rheometric shear flows) of two Boger-type fluids were presented: the first one (Boger-1) was a semidiluted solution of polyacrylamide that has an almost constant viscosity value and normal forces that grow exponentially with the shear rate; the second one (Boger-2) was an associative polymer (Soto *et al.* 2006, Mendoza-Fuentes *et al.* 2009) which also has a constant viscosity value (up to $\dot{\gamma} \approx 6$) and normal forces (higher than the first fluid). We will see that in spite of the similar behavior of these fluids, they can act differently under the same conditions (a rising bubble) due to their different response to extensional flow.

7.1.1 Boger-1 fluid

The terminal velocity of single bubbles as a function of the volume for the Boger-1 fluid and a Newtonian reference fluid (with the same viscosity but without elasticity) are shown in figure 7.1. The presence of a velocity jump discontinuity is evident ($H = 1.3, V_{crit} = 19.3 mm^3$). The velocity jump is also accompanied by the formation of a cusp (a change in the curvature of the surface) in the rear part of the bubble. As the Boger-1 fluid constitute a semidilute polymer solution, the explanation of the origin of the velocity jump must be closer to the surface-active agents hypothesis (see section 2.1). First of all, the velocity discontinuity is not a 'jump' in the sense of increase but in the sense of a velocity recovery. In figure 7.1 it can be seen that after the jump occurs, the velocity values become closer to the Newtonian ones. Secondly, this fluid has a value of a surface tension gradient $\Delta\sigma = \sigma_s - \sigma = 64.8 - 55.6 = 9.2 mN/m$, where σ_s and σ are the solvent and solution surface tension values respectively, revealing that the polymer used has surface activity. The V_{crit} could not be predicted with the Bond and Capillary criteria according to Rodrigue & DeKee (2002); the scaling parameter β proposed by Rodrigue & DeKee (1999b), which take into account the surface tension gradient, proved to predict the critical volume correctly. The parameter β proposed by these authors was defined as:

$$\beta = \left(\frac{\sigma}{\Delta\sigma}\right)^{0.1} \left(\frac{\tau r}{\sigma}\right)^3 \left(\frac{\sigma}{N_1 r}\right) \tag{7.1}$$

where τ and N_1 are the shear stress and first normal stress difference produced by a shear rate of $\dot{\gamma} = U/r$, r being the radius of the bubble. The authors noted that the velocity jump occurs when $Bo/\beta \approx 1300$, the Bond number being defined as $Bo = \rho g r^2/\sigma$. The Bo/β relation in terms of the bubble volume for the Boger-1 fluid is shown in figure 7.2. The last term of equation 7.1 has also been used (in the form of $N_1 d_b/\sigma$) as a critical parameter for the velocity jump in viscoelastic fluids (Soto *et al.* 2006). In this case, however, it is not capable to predict the correct V_{crit}.

The third feature of the Boger-1 fluid is that a negative wake was not seen (corroborated with PIV measurements) in any of the bubbles produced ($0.35 < V[mm^3] < 180$). The velocity field found in the wake left by a bubble rising in the Boger-1 fluid having a volume above the critical one is shown in figure 7.3a. For this fluid a trace of flow reversal is not seen in the downstream direction; actually, the flow structure is very similar to that seen in Newtonian flows. The normalized vertical velocity along the symmetry axis as a function of the normalized distance from the bubble center is shown in figure 7.4. We can see that this fluid does not give place to a change of the flow configuration as described by Herrera-Velarde *et al.* (2003) during the velocity jump, demonstrating that the two phenomena are not always related. The change of the flow configuration can increment the velocity jump magnitude (compare, for example, the value of H obtained in this work [1.3] and the values obtained by Herrera-Velarde and coauthors [$H \approx 2.1$]); however, in view of the present results, such change is not necessary for the velocity jump to occur. The absence of the negative wake in this fluid is in agreement with the negative wake criteria provided by Dou & Phan-Thien (2004), which predicted that no negative wake will form in an Oldroyd-B fluid (or a diluted Boger fluid). Other authors have seen the formation of a negative wake in an Oldroyd-B fluid in numerical simulations

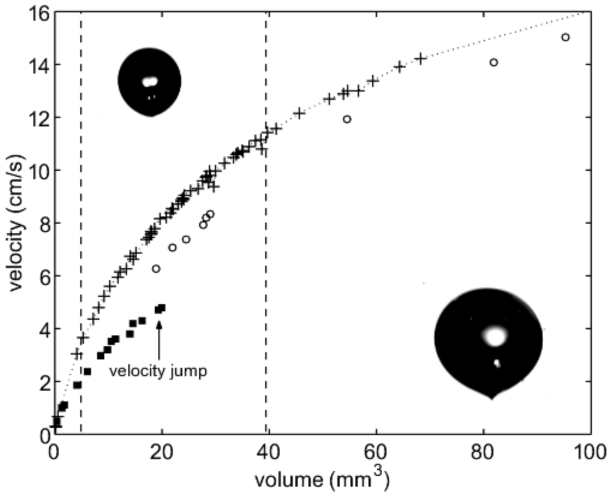

Figure 7.1: Single bubble velocity as a function of the bubble volume; (+) Newtonian fluid, (■) values before and after (○) the velocity jump in the Boger-1 fluid. The maximum Reynolds number reached was around 10. The vertical dashed lines indicate the mean volume of the bubbles produced with the capillary banks (section 7.3): the left one is for the bubbles having a $\overline{d}_b$ of 2.1mm and the right one for bubbles having a $\overline{d}_b$ of 4.2mm. The images on the left and right show typical bubbles before and after the jump.

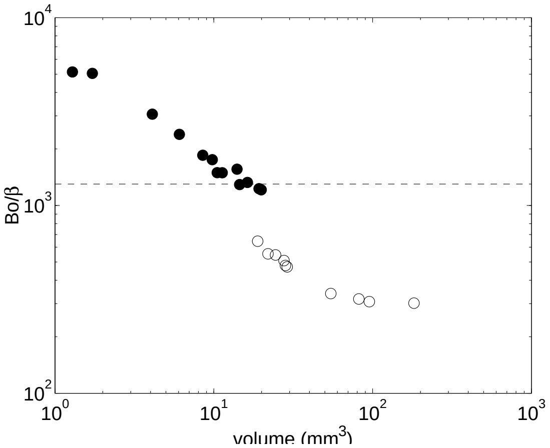

Figure 7.2: Bo/β criterion for the velocity jump in the Boger-1 fluid; filled symbols: values before the velocity jump, empty symbols: values after the velocity jump; horizontal line: $Bo/\beta = 1300$.

(see Pillapakkam *et al.* 2007); however, we have to note that these authors worked in the Maxwelliam limit, i.e. $c > 1$.

The Dou-Phan-Thien criteria is directly related with the extensional properties of the fluids, which in turn can provide a notorious difference between semidiluted and a concentrated polymer solutions (Barnes *et al.* 1989). Figure 7.5 shows the Trouton ratio as a function of the elongational rate for the HASE 1.5% fluid and one of the Boger fluids reported by Pelletier *et al.* (2003), similar to the Boger-1 fluid used in this work. The Trouton ratio is defined as $\eta_E(\dot{\epsilon})/\eta(\sqrt{3}\dot{\epsilon})$, where η_E is the extensional viscosity evaluated at a certain elongational rate $\dot{\epsilon}$ and η the viscosity evaluated at a shear rate $\dot{\gamma} = \sqrt{3}\dot{\epsilon}$ (Jones *et al.* 1987). In the semidiluted polymer fluid the extensional viscosity is higher than the shear viscosity and this relation increases with the elongational rate. In the HASE fluid, on the other hand, the increase of the Trouton ratio is followed by an extensional thinning region. This behavior is due to the construction and rupture of structures due to the extensional flow (Mendoza-Fuentes *et al.* 2009). The strain-thickening behavior seen in this fluid has been associated with the formation of a negative wake (in terms of the slope made by the extensional viscosity with the elongational rate, see the background section). A lesser strain-thickening fluid (as the HASE fluid) is more prone to form a negative wake.

Zana & Leal (1978) argued that changes in the flow is the reason for the changes in the interfacial conditions during the velocity jump: prior to jump, the flow is shear dominated and the bubble surface behaves rigidly due to the polymer molecules adsorbed on it; after the jump, the bubble surface behaves as a free interface as the polymer molecules are desorbed from it resulting from the extensional flow, which now dominates the fluid flow. We explored if this argument can fit the results shown in this study. First, a natural shear time was computed using the expression:

$$\lambda_{shear} = \frac{\Psi_1(\dot{\gamma})}{2\eta(\dot{\gamma})} = \frac{N_1(\dot{\gamma})}{2\eta(\dot{\gamma})\dot{\gamma}^2} \tag{7.2}$$

where Ψ_1 is the first normal stress coefficient. The shear rate is taken as U_{SI}/r. This expression results when solving the convected Maxwell model in simple shear flow. In the case of the Oldroyd-B model the natural shear time is $\lambda_1 - \lambda_2$, where λ_1 and λ_2 are the relaxation and retardation time respectively (Bird *et al.* 1987). The relaxation time for a fluid submitted to extensional flow was taken from the work of Stelter *et al.* (2002). They reported the relaxation times and steady extensional viscosities for several polymeric solutions using an elongational device. In that work, the relaxation time was measured from the diameter decrease of a liquid thread during the elongational flow caused by capillary forces (the elongational flow is self-sustaining and establishes a rate of strain in accordance with the particular fluid, see Stelter *et al.* 2000). The relaxation time was chosen for one of their fluids made with 400ppm of nonionic polyacrylamide ($M_w = 8 - 10 \times 10^6$g/mol) dissolved in a 80/20 (w/w) glycerin-water mixture ($\lambda_{ext} = 0.55s$). The natural shear time and the extensional relaxation time are both shown in figure 7.6. The velocity jump can be seen again in this figure. What it is interesting here is that the values found before and after the velocity jump are approximately separated by the characteristic extensional time of the fluid. This fits the argument of Zana & Leal, that is to say, when λ_{shear} is the limiting time the polymer molecules are forced to stay in touch with the bubble

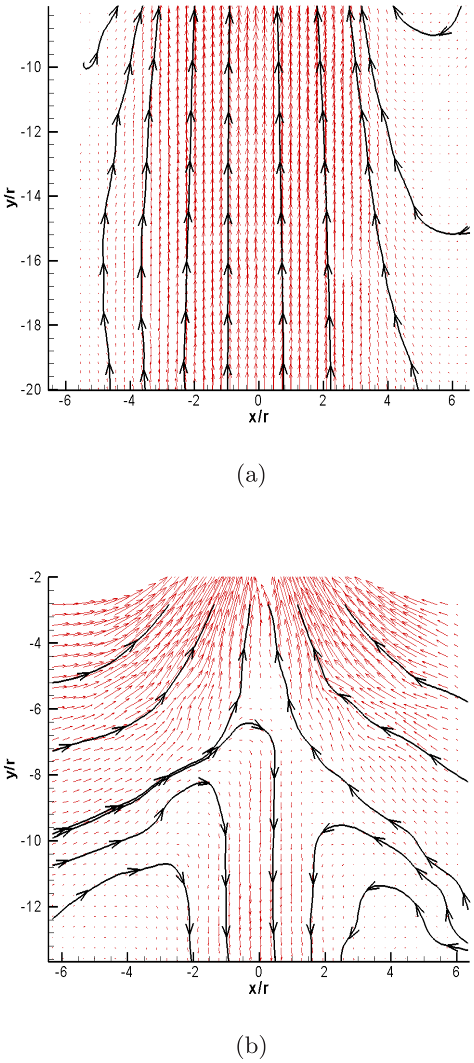

Figure 7.3: Velocity field obtained by PIV of the wake left by the passage of a single bubble (having a volume above the critical one) in the (a) Boger-1 (semidiluted solution, $d_b = 5.13mm$) and (b) Boger-2 (associative polymer, $d_b = 7.18mm$) fluids. The black lines denote some of the streamlines appearing in the flow. The center of the bubbles is located at (0,0). The grid coordinates were normalized by the bubble radius.

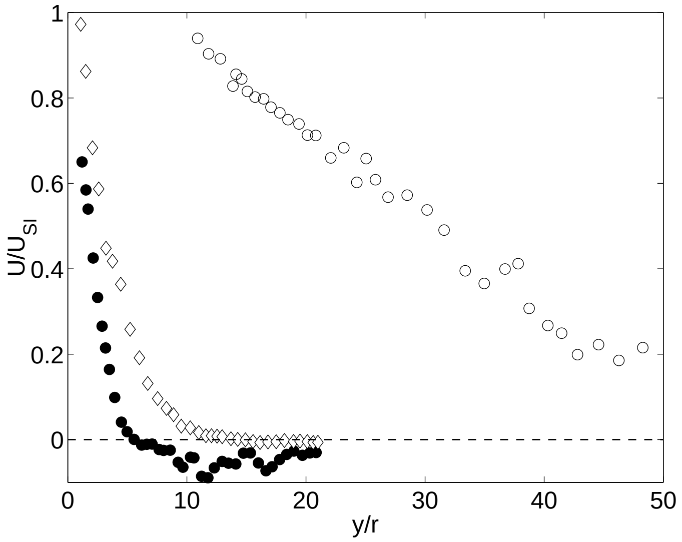

Figure 7.4: Vertical liquid velocity U normalized by the velocity of the bubble U_{SI} as a function of the dimensionless distance y/r, y being the vertical distance and r the bubble or cluster radius. Single bubble case for the semidiluted Boger-1 fluid (○); single bubble case for the concentrated Boger-2 fluid (●) and cluster (◇) from figure 7.9.

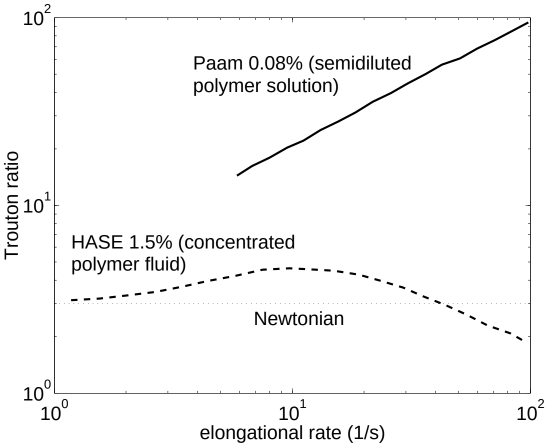

Figure 7.5: Trouton ratio for a semidiluted and concentrated polymer fluids. The values of the Paam 0.08% solution were calculated using the experimental data of Pelletier *et al.* (2003); the values of the HASE 1.5% fluid were estimated using the predicted extensional viscosity values of Mendoza-Fuentes *et al.* (2009).

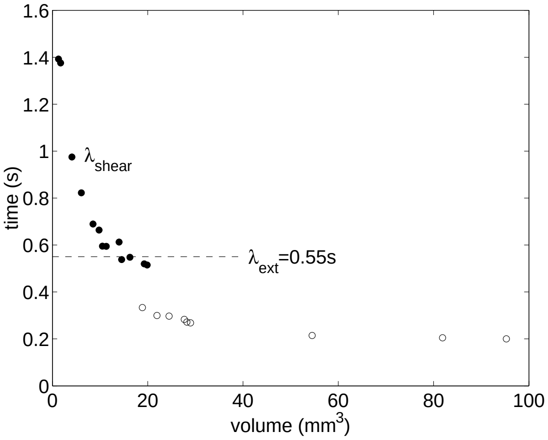

Figure 7.6: Natural times of the bubbles rising in the Boger-1 fluid in terms of its volume. (○) Natural time for shear flow λ_{shear} before (filled symbols) and after (empty symbols) the velocity jump. (−−) extensional relaxation time λ_{ext} of the fluid.

surface; on the other hand, when λ_{ext} becomes the limiting time (the λ_{shear} becomes faster), the polymers are pulled out from the bubble surface. It is worth mentioning that the extensional flow developed in the rear part of a bubble do not necessarily implies that a reverse flow (negative wake) will be produced. The location of an inversion point separating the upward and downward flows will rather depend on the properties of the extensional viscosity (see figure 7.5).

7.1.2 Boger-2 fluid

The volume-velocity plot for single bubbles rising in the HASE fluid (Boger-2) is shown in figure 7.7 (circular symbols). A velocity jump can be seen at $V_{crit} \approx 40mm^3$ ($H = 1.5$). As mentioned by Soto *et al.* (2006), the velocity jump experienced by bubbles rising in this fluid is accompanied by the formation of a cusped end shape on the bubbles and a negative wake; the HASE fluid is also capable to produce long tails that originate in the bubble cusp (Soto *et al.* 2008). We can see in figures 7.3b and 7.4 that the negative wake appears after a certain distance from the bubble surface, as found by other authors (Herrera-Velarde *et al.* 2003, Frank & Li 2005, Kemiha *et al.* 2006, Soto *et al.* 2006, Pillapakkam *et al.* 2007); also note that the flow configuration is completely different from the one formed in non-elastic flows and in semidiluted polymer solutions ($c < 1$), such as the Boger-1 fluid. Unlike the latter one, in which the shear rate at which the velocity jump occurs coincide with the change of the slope of the normal force (see figure 5.5); for the case of the Boger-2 fluid the jump occurs at a shear rate in which normal forces are not yet measurable (see figure 5.7). Hence, the hydrodynamic criteria in this fluid can only be applied if the rheological data is extrapolated to lower shear rates (Soto *et al.* 2006, Mendoza-Fuentes *et al.* 2009). For example, Soto *et al.* (2006) employed the Bautista-Manero model (Bautista *et al.* 1999) to estimate the value of the normal stress difference N_1 at which the velocity jump occurs. Using the dimensionless number $N_1 d_b/\sigma$

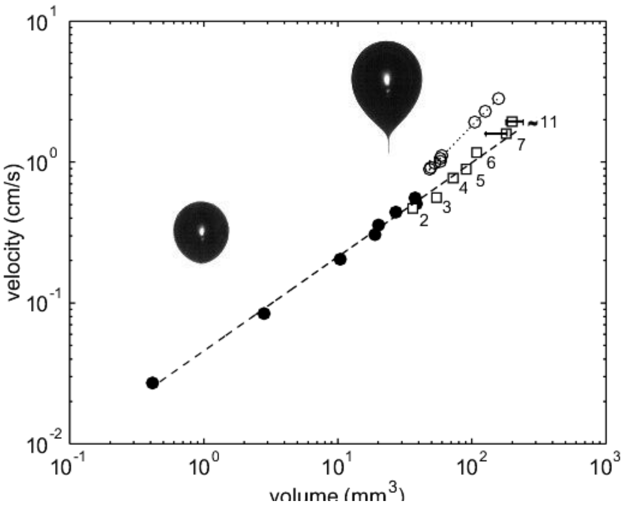

Figure 7.7: Terminal velocity as a function of the volume for the Boger-2 fluid. (●) single bubble velocities before the jump, (○) single bubble velocities after the jump. (□) velocity of the bubble clusters. The numbers in the plot indicate the number of bubbles forming the cluster. The horizontal lines in the squares indicate the uncertainty of the volume. The maximum Reynolds number reached was around 0.1.

proposed by these authors, we found good agreement with the critical value reported by them ($\Pi \approx 0.25$).

To complete our understanding of the nature of the velocity jump, we conducted a series of experiments to determine the terminal velocity and flow field around groups of bubbles (clusters) in the concentrated Boger-2 fluid. For this highly viscous fluid, it is easy to release several bubbles at once (of a known volume) without coalescence. By considering small bubbles (having a volume below the critical one), clusters consisting of several bubbles could be produced to have an equivalent volume equal to those bubbles which experience the velocity jump. The bubble clusters were made by collecting different numbers of bubbles produced by a syringe with a similar volume ($V \approx 22mm^3$). Figure 7.7 shows the terminal velocity of the bubble clusters with different number of bubbles. The numbers in the figure correspond to the number of bubbles (N) forming the cluster, which correspond to the images shown in figure 7.8. Relative motion between the bubbles was not observed within the cluster; however, some internal motion can be seen in similar fluids with lower viscosity (not shown here). Note that bubble groups having $N < 7$ form regular polyhedrons; a similar behavior was observed in the case of settling particles moving at low Reynolds numbers, see Jayaweera *et al.* (1964) and Hocking (1964). Also note that the groups having 3 or 4 bubbles, which have an equivalent volume $V > V_{crit}$ (for single bubbles), do not show a cusped end shape. Surprisingly, the bubble groups do not experience the velocity jump observed for the case of single bubbles. In fact, the velocity of clusters closely follow the volume-velocity trend for single bubbles before the critical volume.

In figure 7.9 the velocity field behind a bubble cluster (N=11, $V \approx 240mm^3$) is shown. The flow field was compared with that produced by a single bubble with a similar volume

($V \approx 200mm^3$). Immediately after the passage of the bubble or the bubble cluster ($|y/r| < 12$), the flow field between these two cases is different: while in the single bubble case an inversion point of the flow appears at $y/r \approx 7$ (see figure 7.3), in the case of the bubble cluster the appearance of a negative wake is not readily observed. However, if the flow is analyzed at farther regions from the bubble cluster ($y/d = 21$, figure 7.9b), a weak flow reversal can be observed. Clearly, the flow structure left by the bubble cluster is more asymmetric than that produced by a single bubble; also, the maximum velocity achieved in the negative wake of the cluster is 92% less than the value found in the single bubble case. However, it is clear that an inversion point of the flow is also seen in the case of the clusters, which did not present a velocity discontinuity (see also figure 7.4). We may argue then that the absence of the velocity jump in the bubble clusters is mainly due to the restriction of the surface mobility: the clusters behave like a single bubble but having a segmented interface; hence, the surface mobility is significantly reduced (specially for bubbles located at the top of the cluster), giving place to a partial obstruction of the "cleaning" mechanism at the bubble surface and thus avoiding the velocity jump. In view of these results, we are more inclined to think that the appearance and magnitude of the negative wake is a result of the extensional rate exerted by the bubble (which depends on the bubble size and velocity), rather than the cause of the terminal velocity value. However, both phenomena could be related in a more complex way. The terminal velocity of the bubble (or cluster), together with the flow structure around it, could be the result of both mechanisms interacting at the same time.

7.1.3 Numerical simulations

As mentioned above, the use of numerical solutions to study the flow of viscoelastic fluids is rather limited. The lack of success of the algorithms is due, in general, to the poor interpolation schemes for the stress tensor values among the elements or control volumes. The stress in a viscoelastic fluid experiences a combination of deformation and convection during the fluid flow, this can give place to the appearance of very steep exponential profiles (Fattal & Kupferman 2005) even for moderate Deborah numbers ($De \sim 1$, the permissible values of the characteristic time covers only those flows with very low Re numbers). Because of this, several authors (Singh & Leal 1993, Frank & Li 2005, Fattal & Kupferman 2005, Radl *et al.* 2007, Pillapakam *et al.* 2007) have concentrated their efforts in proposing strategies to deal with this problem[10]. Only Frank & Li (2005) have successfully simulate (using a free-energy-based lattice Boltzmann scheme) the flow around a bubble, including the negative wake, using "realistic" rheological data. Nevertheless, the comparison between their experimental and numerical results was only qualitative and they used the generalized Maxwell model (no frame invariant) to account for the memory effects.

---

[10] The general failure of the numerical codes to solve the flow in viscoelastic fluids is known as the *"High-Weissenberg Number Problem"*, or HWNP. Among the strategies that have been proposed to manage this problem are the use of exponential basis functions of the stress variable (Fattal & Kupferman 2005), artificial diffusion in the constitutive equation (Radl *et al.* 2007), application of special algorithms to preserve the positiveness and boundedness of the stress tensor (Singh & Leal 1993, Pillapakam *et al.* 2007, Radl *et al.* 2007), and implementation of upwinding schemes in the discretization of the constitutive equations (Singh & Leal 1993, Pillapakam *et al.* 2007).

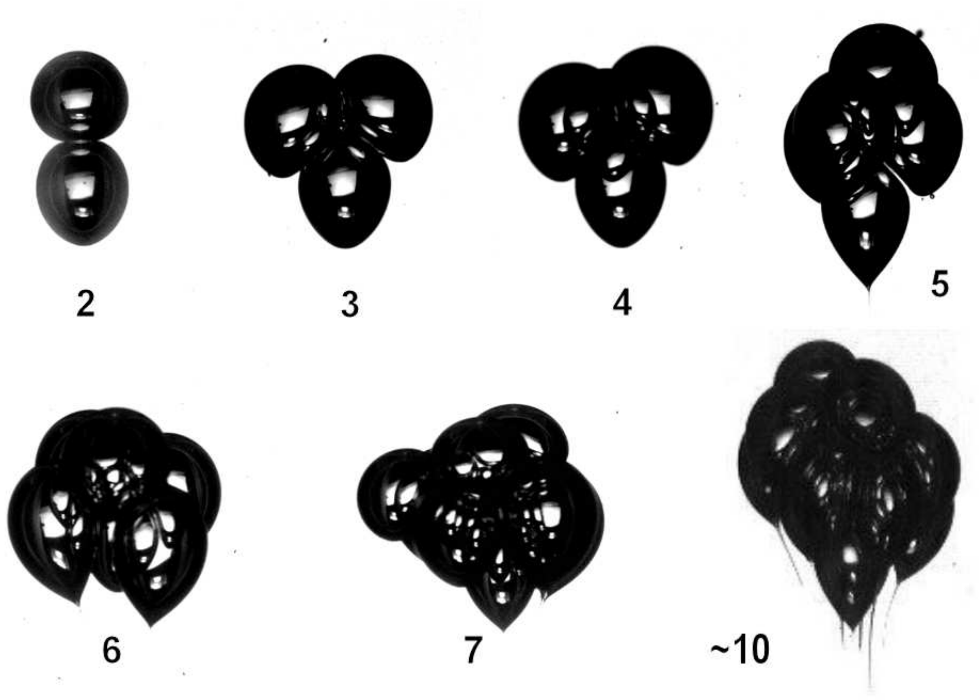

Figure 7.8: Pictures of the bubble groups. The numbers indicate the number of bubbles forming the group (see figure 7.7). Note that the bubbles form regular, but not uniform, polyhedrons with $N < 7$. For instance, the cluster with four bubbles form a tetrahedron, the one with five an hexahedron and the one with six an octahedron.

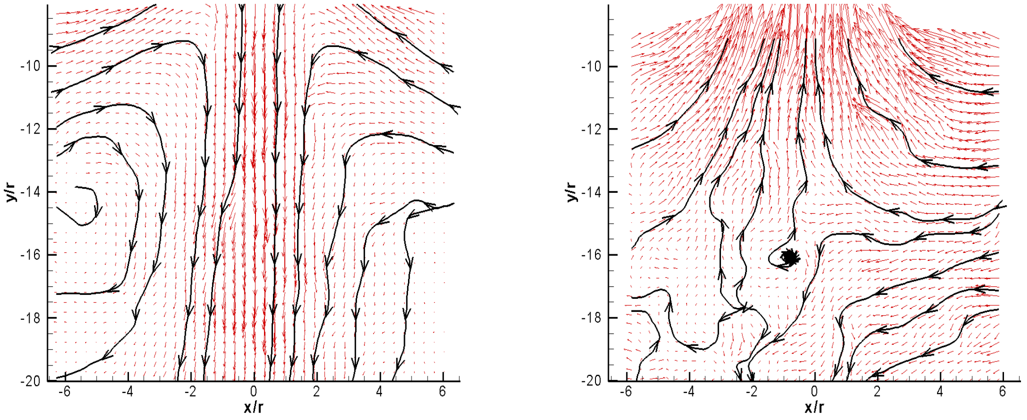

(a) (b)

Figure 7.9: Velocity field obtained by PIV in the Boger-2 fluid of the wake left by the passage of a single bubble or a bubble cluster having both a volume above the critical one; (a) single bubble ($V = 194mm^3$); (b) bubble cluster (N=11, $V \approx 240mm^3$). The black lines show some of the flow streamlines. The center of the bubble or the cluster is located at (0,0). The grid coordinates were normalized by the bubble radius or the equivalent cluster radius. The Reynolds and Weber number for the single bubble is around 0.12 and 0.23 respectively.

Since the ALE code used in this study is not appropriate to deal with the HWN problem, the few results that are shown in this section represent the transient or unsteady behavior of the bubbles. Figure 7.10 shows the velocity field and some streamlines of the flow produced by an Oldroyd-B fluid having a concentration parameter value of $c = 12.6$ (concentrated solution). The physical data used by Pillapakam *et al.* (2007) were used here to generate the negative wake. In agreement with these authors and others (Herrera-Velarde *et al.* 2003), the flow field shows two vortex rings: the first one corresponds to the usual convection of the fluid that is displaced by the bubble; the second one is generated by the reverse flow in the rear part of the bubble (a similar flow structure has been found by Radl *et al.* 2007 using the Giesekus and Phan-Thien models). Note also that the bubble is highly deformed in the rear. This characteristic “teardrop” shape acquired by the bubbles rising in highly viscous, elastic fluids, is created by the restoring forces that appear when the polymer chains experience a deformation in the radial and θ directions: when the equator of the bubble has past from a reference point, the polymer chains will tend to return to some previous configuration; this will cause inwards bending of the surface of the bubble. As we move to the lower side, the curvature of the surface will increase gradually. At the very tip the curvature of the bubble, offset by the superficial forces, will be very high; the normal stresses will be also high due to the converging streamlines and the extensional flow concentrated around this region. The profile of the normal stresses around the bubble showed in figure 7.10 can be seen in figure 7.11. In addition, the numerical resolution at the tip or trailing end of the bubble constitutes a mayor computational issue. This issue is discussed below.

Now, two important points must be emphasized: the negative wake appearance (and velocity jump discontinuity seen in numerical simulations of an Oldroyd-B fluid) and the geometrical resolution at the bubble tip. In figure 7.10 we can observe that a negative wake can be formed behind a bubble rising in an Oldroyd-B fluid. This flow is a reproduction of the results of Pillapakam *et al.* (2007). Figure 7.12 shows the values of the bubble velocity in terms of the volume obtained by these authors for different values of c; the segmented line in the figure corresponds to the values of the velocities obtained in a Newtonian fluid having the same physical data but without elasticity (these results were obtained in this work using the ALE code and the original data of Pillapakam and coauthors). We can see that a clear velocity jump is observed for several values of c (above 5.8); additionally, the velocity values obtained after the velocity jump are higher than the ones obtained in the Newtonian fluid. All these numerical results seem to contradict the arguments exposed in the previous section supported by the discussion of Dou & Phan-Thien (2004) and on the results shown above (for the Boger-1 fluid): an Oldroyd-B model cannot generate a negative wake. Secondly, in the volume-velocity plot corresponding to the Boger-1 fluid (figure 7.1), we observed that the velocity discontinuity did not lead the bubble to a large increase of the velocity but to a recovery from the elastic stress acting upon its surface. How can we conciliate these two apparently contradictory results?.

The answer seems to be in the value of the concentration parameter c. In a diluted Boger or Oldroyd-B fluid ($c < 1$), the elastic response of the polymer is retarded by the solvent viscosity. In this case the behavior will be very similar to the one obtained for the Boger-1 fluid. For the cases when $c > 1$, the Oldroyd-B fluid will behave more like a Maxwell fluid, that is; the elastic (springs) behavior will be more free to act depending on the degree of deformation since the retardation time will be comparatively small. This will give place to the results obtained for the Boger-2 fluid. The question of whether a concentrated Boger-type fluid can give place to a real velocity jump (above the values achieved by its Newtonian counterpart) remains as an open question. We cannot, however, be totally confident with the numerical results obtained so far. Note, for example, that is unlikely that a real concentrated polymer solution will behave like an Oldroyd-B fluid; is more probable that such fluid will behave as the Boger-2 fluid does and which have to be modeled, in turn, by special models which consider the polymer structure (see Bautista *et al.* 1999, Mendoza-Fuentes *et al.* 2009). Moreover (and this is where the experimentalist can throw the “first stone” to the people working in numerical simulations), the physical data chosen by Pillapakam *et al.* (2007) is quiet unrealistic. As far as we know, there is no polymer solution having a surface tension value as low as $10mN/m$ (which was the value employed in this simulations in order to produce a notable surface deformation)[11]. A deeper understanding of the matter will require a comparison between experiments done in a concentrated polymer solution and in a Newtonian counterpart fluid, or; run simulations with realistic physical data.

Concerning the shape of the tail acquired by bubbles ascending in viscoelastic fluids, there have been some studies (Liu *et al.* 1995, Soto *et al.* 2008) which have mentioned the variety of the shapes that can be observed for different values of the bubble volumes:

---

[11] The surface tension value of pure eter ethylic is, for instance, 17 mN/m.

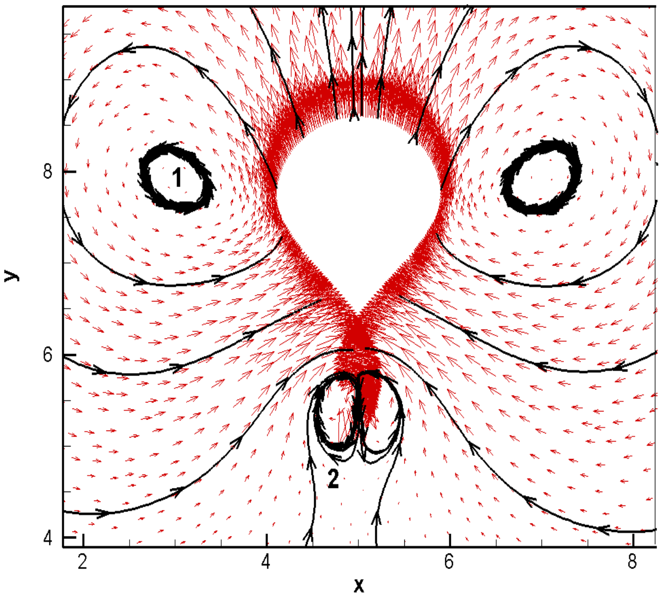

Figure 7.10: Velocity field and some streamlines formed in the transient flow around a bubble rising in an Oldroyd-B fluid. The physical parameters were taken form Pillapakam *et al.* (2007): $\rho = 1000 kg/m^3$, $\eta = 1.02 Pa{\cdot}s$, $\sigma = 10 mN/m$, $\lambda_1 = 0.1s$, $c = 12.6$, $d_b = 3mm$. The instantaneous flow field was taken at $t^* = 5.3$. This particular run was made using the 2D geometry, the axysimmetric configuration is more prone to code blow-ups. The numbers in the figure indicates the number of vortex rings generated around the bubbles.

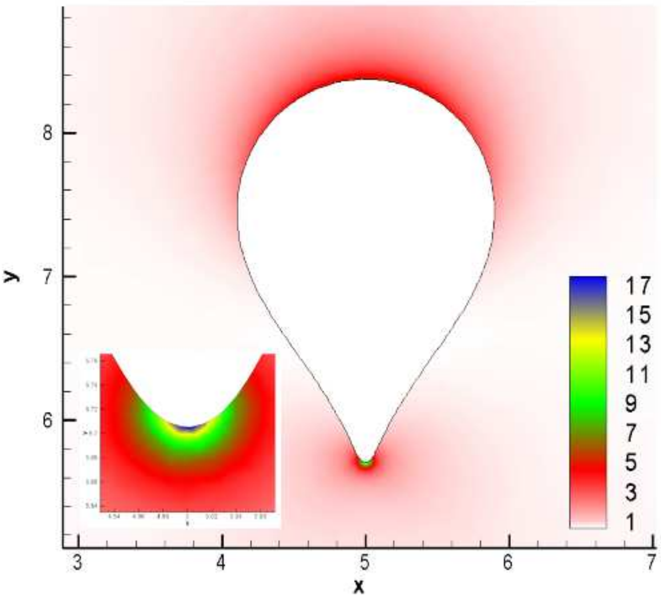

Figure 7.11: Dimensionless values of the normal stresses (trace of the stress tensor) formed around a bubble rising in an Oldroyd-B fluid. The physical data is shown in figure 7.10, $t^* = 4.7$. The inset shows the stress profile at the bubble tip.

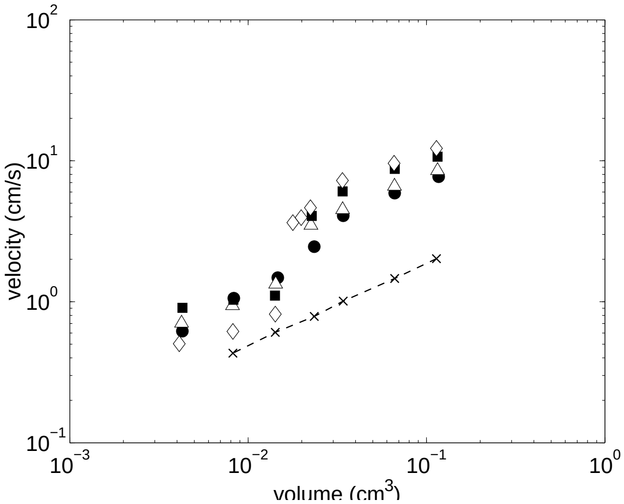

Figure 7.12: Terminal velocity of the bubbles rising in an Oldroyd-B fluid in terms of its volume for different values of c: (●) 4.1, (△) 5.8, (■) 9.2, (◊) 12.6 (data taken from Pillapakam *et al.* 2007). The (×) marks correspond to the velocity values obtained in a Newtonian fluid counterpart having the same physical values but without elasticity; these results were obtained in this work using the ALE code.

from the usual axisymmetric cusp, passing through a “knife” or “chisel-edge” shape, up to different patterns (“fish backbone”) generated during the breakup of the tail (Soto *et al.* 2008). Interestingly, Liu *et al.* (1995) even found that the chisel-edge shape is oriented in a particular manner with the walls of the container. Due to the spatial discretization done by the numerical procedures, the finite elements (or volumes) techniques have the inherent problem in defining the correct geometrical configuration at the bubble tail (Pillapakam *et al.* 2007). As a curious observation, the mesh structure formed by the elastic forces computed in the simulations done here cause the overlapping of the spatial mesh at the trailing edge of the bubble (like a formation of a back cavity). Regardless of whether this cavity is correct or not, is worth mentioning that none of the numerical algorithms currently available have been able to reproduce the formation of a long tail and its subsequent breakage or collapse for the case of a bubble rising in a non-Newtonian fluid[12]. Both behaviors have been observed in experiments (Soto *et al.* 2008) and have a close relation with the fracture of the network structure in concentrated polymer solutions.

7.2 Bubble pairs and chains in Boger fluids

In the previous section we saw that the effects of the elasticity on the bubble motion have a close relation with the surface properties of the bubbles (although a direct evidence of this is not presented, the experimental results and the analysis suggests that this indeed happens). Other experimental essays have also revealed this kind of relation between these two properties (Sullivan *et al.* 2008). In this section, and specially in the next one, we will see the influence of these coupled effects in the motion of more than two bubbles. Unlike the previous chapter, in which four different shear-thinning fluids were presented and their behavior characterized; here the results for the Boger-1 (semidiluted) fluid will be shown. Therefore, the discussion will be shorter (but interesting) than that presented before.

To begin with, a detailed description of the interaction of two bubbles rising in a Boger fluid will be omitted since the general behavior resulted to be qualitatively similar to the one shown in the last chapter: If the bubbles are small (low inertia), the bubbles will have the chance to travel as a doublet (vertically aligned) after the drafting and kissing stages. If the bubbles are large, the inertia will tend to separate them after contact. Sometimes, the bubbles having $V > V_{crit}$ performed a series of rebounds between them during their ascension through the column. Interestingly, the formation of the cusp in the rear part of the bubbles (for this case a negative wake is not observed) does not prevent the trailing bubble to catch up with the leading one. Li and coauthors (Li *et al.* 2001) have shown, additionally, that two in-line bubbles rising in a viscoelastic fluid (presumably, a semidiluted solution) follow the usual drafting process even in the presence of a negative wake[13].

---

[12] There is, by the way, some advances in the numerical solution of the breakage of weakly viscoelastic filaments, see Ardekani *et al.* (2010).

[13] The question of whether a negative wake can or cannot prevent the collision of two bodies moving in tandem cannot be answered yet. For instance, Riddle *et al.* (1977) observed that two particles released in tandem in a highly viscous elastic fluid can, depending on their initial separation, converge or diverge during its travel through the liquid. Although they did not verify the presence of a negative wake, we

In the case of the bubbles released side-by-side (small bubbles $d_b = 2.4mm$) it was observed that they almost conserved their initial separation distance. We[14] started from this result and performed a series of experiments to see if the rate of bubble release (the inverse of the injection period T) had some influence in the interaction of bubbles displaying a horizontal arrange. This was also done because we were expecting to see some kind of attraction between the bubbles, similar to the behavior seen by Joseph *et al.* (1994) for the case of settling particles. Figure 7.13 shows images of bubble chains produced 1cm away from each other. Figures 7.13a and b present images, the second one taken 2.8s after the first one, of two bubble chains produced with a flow rate of $60ml/h$ ($T = 0.17s$). Figures 7.13c and d present the same setup but now having a flow rate of $130ml/h$ (T=0.08s). In the first row of the figure we can observe that the bubbles (see the bubble pair marked with arrows) located in different chains do not came in contact. In the second row, however, the bubbles do come in contact with the bubbles rising in the other chain; after some time, some bubble pairing is seen. The discovery of these results made us to think that the increase of the injection rate (increase of the rate of consecutive deformations to the fluid) will lead to the accumulation of elastic stresses.

In the background chapter we mentioned that Li and coauthors (1997) proposed and performed a series of experiments in order to simulate the consecutive passage of bubbles through a fluid and measure the stresses forming on it (a methodology known as "rheological simulations", see Li *et al.* 1997 & 1998). In this work the same methodology was employed to see if the Boger-1 fluid was also capable, as the fluids employed by these authors, to generate residual stresses. It turned out that the viscosity of the Boger-1 fluid was not sufficiently high to generate residual shear stresses that allow us to distinguish differences between this fluid and its Newtonian counterpart. We decided then to conduct unsteady measurements of the first normal stress difference, N_1. A controlled-deformation rheometer (*ARES-RFS III, TA Instruments USA*) was programmed to apply a steady shear rate to a fluid sample, starting from rest. The shear rate corresponded to that of a bubble ascending freely ($\dot{\gamma} = U/r = 72.3s^{-1}$, U being the vertical bubble velocity for the case presented in figure 7.13c). The evolution of N_1 was determined throughout the process until a steady state was reached. After a certain time, the deformation was stopped to also determine the relaxation of N_1 with time. Figure 7.14 shows the N_1 values normalized by the steady state value as a function of time.

The transient values of N_1 in the increase phase can be fitted to an empirical saturation equation of the form:

$$N_1 = \frac{N_{max}(t - t_o)}{\lambda_{growth} + t - t_o} \tag{7.3}$$

where N_{max} is the maximum hypothetical steady N_1 value reached by the initial slope before the overshoot, λ_{growth} is the time for which the $Nmax/2$ value is reached and t_o is the reference time (when N_1 has a zero value). On the other hand, the relaxation curve

---

can argue that the behavior observed could be in close relation with the flow structure formed behind the leading particle.

[14] The idea to do this actually came from an undergraduate student, Diego Sámano (see Sámano 2011).

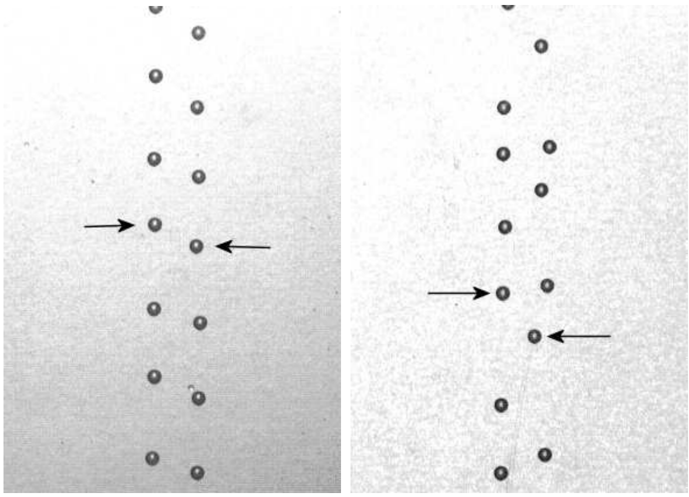

(a) 60 ml/h, initial condition (b) 60 ml/h, t=2.8s

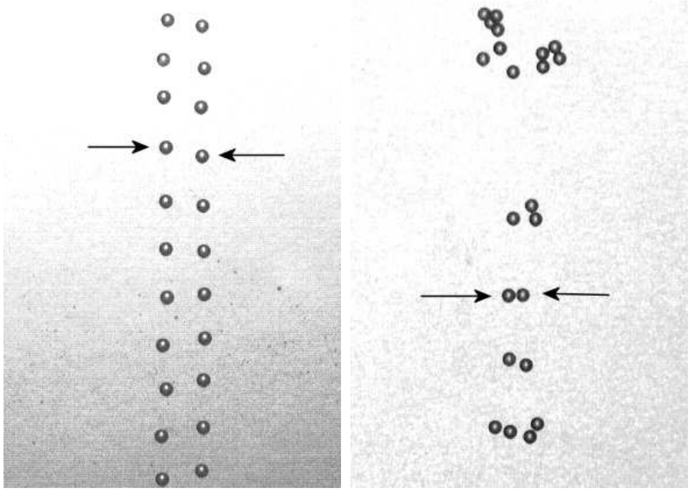

(c) 130 ml/h, initial condition (d) 130 ml/h, t=2.8s

Figure 7.13: Bubble chains produced at different gas flow rates with bubbles having a $V < V_{crit}$. Separation between bubbles chains: 1cm; $d_b = 2.4mm$, $Re \approx 2.3$.

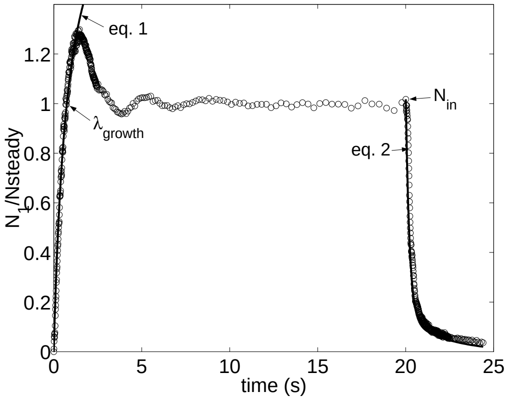

Figure 7.14: Normal stress values of the Boger-1 fluid taken at a steady shear rate of $72.3s^{-1}$. The deformation rate was stopped at a time of 20s. The original curve was filtered in order to eliminate mechanical oscillations of the rheometer motor. The parameters depicted in the figure corresponds to eq. 7.3 and 7.4: N_{steady}=32Pa, N_{max}=65.9Pa, $\lambda_{growth} = 0.79s$, $a_1 = 0.866$, $\lambda_1 = 0.208s$, $a_2 = 0.133$, $\lambda_2 = 2.303s$.

can be modeled using the exponential decay equation:

$$N_1 = N_{in} \left[\sum_{i=1}^{2} a_i e^{-(t-t_{in})/\lambda_i} \right] \tag{7.4}$$

where N_{in} is the initial value at the time t_{in} at which the shear deformation is stopped, λ_i are the relaxation times and a_i are constants related with λ_i. The accumulation of normal stress due to the consecutive passage of the bubbles can therefore be approximated using these two equations alternately and considering the values of the injection period T and the characteristic bubble time $t_b = 1/\dot{\gamma}$. For instance, eq. 7.3 is used until the time t_b is reached, then we continue computing the stress with eq. 7.4 making $t_{in} = t_b$ until the time $t_b + T$ is reached. After this, we use eq. 7.3 again (updating the t_o value) up to a time $2t_b + T$ and so on. Figure 7.15 shows the rheometric values of the normal stress in the form N_1/N_{steady} as a function of the normalized time t/t_b together with two curves obtained from eqs. 7.3 and 7.4. The value of the repulsive stress produced by the converging streamlines in between two spherical bodies is also shown in figure 7.15, according to the equation proposed by Vasseur & Cox (1977):

$$S_L = -\frac{9}{2}\eta U \left(\delta\delta^*\right)^{-1} \left[2 - (\delta^* + 2)e^{-\frac{1}{2}\delta^*}\right] \tag{7.5}$$

where δ is the separation distance between centers and $\delta^* = \rho\delta U/\eta$, ρ and η being the liquid density and viscosity respectively. This value represents the stress necessary for two bubbles to attract each other when rising side-by-side.

The dotted curve in figure 7.15 represents the experimental case showed in figure 7.13c ($T \approx 6t_b$). In this case the normal stress reached a value above that produced by the passage of a single bubble but is slightly below the value of the repulsive stress (eq. 7.5). The continuous line represents the case when $T = t_b$, which can be reached in continuous

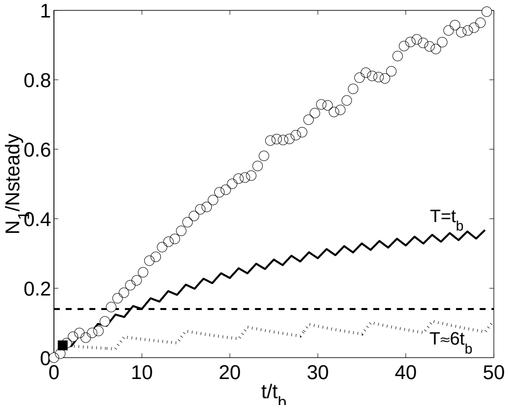

Figure 7.15: Normalized normal stress, N_1/N_{steady}, as a function of the normalized time t/t_b ($t_b = 0.01382s$); (○) experimental values; dotted and continuous lines: estimated values of the normal stress using eq. 7.3 and 7.4 for $T \approx 6t_b$ and $T = t_b$ respectively; (■) normal stress value produced by the passage of a single bubble. The dashed horizontal line corresponds to the normalized repulsive stress generated by two abreast spherical bodies from eq. 7.5. The maximum value of the abscissa is less than $\lambda_{growth}/t_b = 57$.

bubbly flows like those shown in the next section. This curve rapidly surpasses the value of the repulsive stress; hence, in this case the normal stress can be expected to induce the pairing of the bubbles and therefore clustering. Note that in neither case, the rheometric steady value of N_1 is reached. This is an important observation since such value is often used in the analysis of flows.

The results presented in this section suggest that the accumulation of normal stresses due to the consecutive passage of bubbles is a determining parameter in the formation of clusters in elastic fluids, in accordance with Li and coauthors (1998). It is worth mentioning, however, that the accumulation of elastic stress is not a necessary condition for all the fluids to produce clustering. For example, Joseph and coauthors (1994) observed the attraction of two particles falling in viscoelastic fluids without any previous passage of other particles. Again, the key point can rely on how concentrated is the polymer solution; i.e., how large are the normal stresses comparing with the viscous ones. What we can speculate in these cases is the fact that the passage of several bubbles (with no-slip condition) or particles could change the critical distance necessary to attract two bodies by elastic forces: two bubbles rising in different chains and having an initial horizontal separation distance δ_o will feel an attractive forces and converge while a bubble pair will keep constant their separation distance with time.

7.3 Bubble swarms in Boger fluids

Figure 7.16 shows images of bubble swarms rising in the Boger-1 fluid for two bubble sizes: one having a diameter (2.1mm) corresponding to a volume below the critical one (see fig. 7.1), and the other having a diameter (4.2mm) above the critical value. We can see that the difference in bubble dispersion between one case and the other is striking. For the case when the bubbles have a volume below the critical one, large vertical clusters are formed in the fluid flow. When the bubbles have, on the other hand, a volume above the critical one, there is no clustering and the bubble dispersion is greatly improved (in figure 7.16e we can see that the bubbles attain the characteristic teardrop shape).

For the case of bubbly flows, the accumulation of elastic stress should increase as the gas fraction (or the number of bubble chains) is increased. Therefore, we can expect that at low gas fractions the elastic effects will not be large enough to cause cluster formation. Such gas fraction value can be estimated if we consider that the mean separation distance $\overline{\delta}$ between bubbles is proportional to $1/N^{1/3}$, N being the bubble number density and equal to $6\Phi_g/\pi d_b^3$; hence, the gas fraction will be proportional to $\frac{\pi}{6}(d_b/\overline{\delta})^3$. Using the experimental value of the bubble diameter ($d_b = 2.1mm$) and the mean separation distance for the case where no clustering where observed between the two chains (figure 7.13a and b, $\overline{\delta} = 1.36cm$), the gas fraction below which we could expect that no clustering occurs is 0.002. With our setup, however, it is not possible to conduct experiments for such small values of Φ_g.

Based on the results obtained in this section and in the previous one, we can conclude that when the accumulated elastic stress is larger than the viscous repulsive stress, aggregation occurs. Also, we can argue that the elastic accumulation increases with $\dot{\gamma}$, i.e., with the bubble size. However, this argument contradicts the observation of dispersion for large bubbles ($V > V_{crit}$). Therefore, the effect that large bubbles have on the fluid must be different. Poor elastic accumulation could occur if the bubbles are not imposing deformation on the fluid; that is to say, that such bubbles are "slipping" through the liquid. This can only occur if the surface of bubbles has become mobile (surface active agents have been liberated from the interface). This fact supports the argument that the bubble velocity discontinuity is a result of a self-cleaning mechanism of the interface, as suggested by Rodrigue & De Kee (2002).

The accumulation of restoring forces are not the unique promoters of bubble clustering in elastic fluids. These forces are indeed the ones that carry out the attraction of the bubbles in vertical arrangements among the bubble chains; but the generation of a long (and unique) vertical clusters, like the ones seen in figures 7.16a and c, is a macroscopic flow event. What is happening here is that, as soon as the bubbles form separate vertical clusters, the disperse phase is segregated to one large column of gas due to the appearance of a long recirculation loop of the continuous phase. In most cases, this column of gas actually tend to ascend near a column wall while the liquid descends in the opposite one. In these cases, the amount of gas retained in the liquid almost falls to zero. In the case of the bubbles having a volume above the critical one, the appearance of a recirculation loop also occurs but the bubbles rise in a free manner within the main plume. The fluctuating velocity field of the liquid within the ascending flow can be obtained with the PIV system. The flow containing a good dispersion of the gas phase must present a better spatial distribution of the average agitation value. The probability density function of the liquid agitation obtained in the unclustered and clustered fully developed flows are shown in figure 7.17. The vertical velocity variance T_L was normalized with the mean bubble velocity U_{SW} ($Tnorm = T_L/U_{SW}^2$). The values shown in the figure correspond to the liquid agitation found in the ascending flow of the bubbles, i.e., without considering the liquid circulation loop. The results are presented in terms of $Tnorm - < Tnorm >$, $< Tnorm >$ being the average agitation value. The curves show that the probability of finding a homogeneous agitation is larger in the unclustered flow than in the flow where large bubble clusters are formed, in accordance to the visual observation shown in figure 7.16. The lines in figure 7.17 denote a normal pdf fitting of the experimental values[15].

---

[15] The normal density function (or gaussian) have the form: $f(y) = \frac{1}{\sigma\sqrt{2\pi}} e^{-(y-\mu)^2/2\sigma^2}$, $-\infty < y < \infty$; where μ is the mean and σ the standard deviation. For more information or consultation of normal area curves see Mendenhall and Sincich (1997).

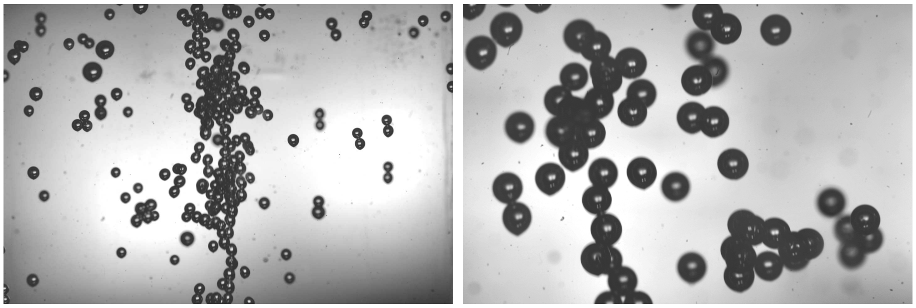

(a) $d_b = 2.1mm, V < V_{crit}, \Phi = 0.4\%$ (b) zoom of (a)

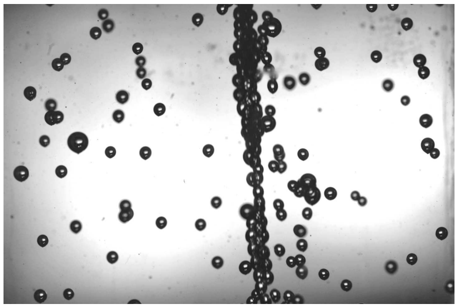

(c) $d_b = 2.1mm, \Phi = 0.5\%$

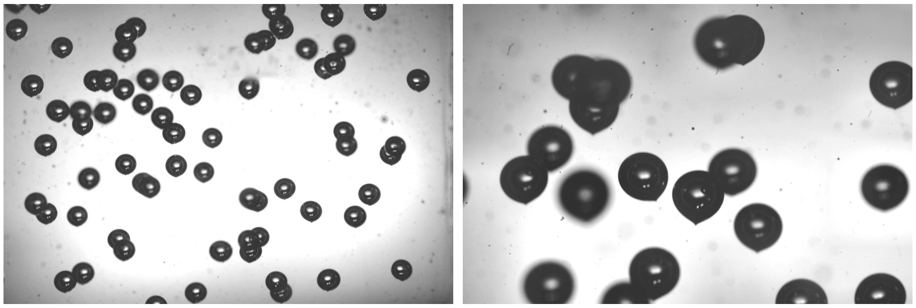

(d) $d_b = 4.2mm, V > V_{crit}, \Phi = 0.4\%$ (e) zoom of (d)

Figure 7.16: Images of the bubbly flows rising in the Boger-1 fluid. The gas fraction values reported for the bubbles having a diameter of 2.1mm was measured at the beginning of the experiment (when the valve was opened). In these cases, the evolution of the gas fraction with time becomes very unstable and in many cases falls to zero due to phase segregation.

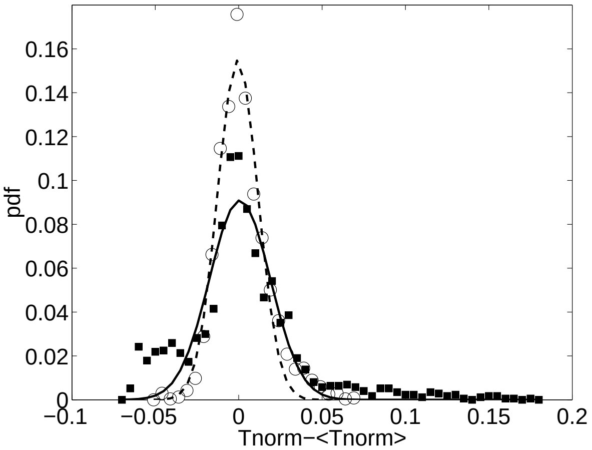

Figure 7.17: Probability density function of the vertical agitation values of the liquid obtained for the Boger-1 fluid; (○) unclustered flow: $d_b = 4.2mm$, $< v_L >$=10.95 cm/s, $< T_L >= 9.7cm^2/s^2$; (■) clustered flow: $d_b = 2.1mm$, $< v_L >$=12.58 cm/s, $< T_L >= 28cm^2/s^2$. $< v_L >$ is the mean vertical liquid velocity. In both cases $\Phi_g = 0.3\%$. The lines denote a normal pdf fitting of the experimental values.

Chapter 8

Some additional comments on aggregation in viscoelastic fluids

The phenomenon of particle aggregation (either with rigid or movable interfaces) is a general trend found in viscoelastic flows. This behavior was already seen in the early works of Nighgate *et al.* (1966, 1969) and Michele *et al.* (1977). These authors noted that rigid spheres as small as 60-70μm embedded in a viscoelastic matrix tend to form chaining structures when submitted to a rheometric flow. In this work we have seen that both, the thinning and the elastic behavior, are capable to cause clustering in bubbly flows. Before moving to the conclusions, I would like to say a few comments on two issues of my interest.

The first one is about the future of multiphase flow simulations in viscoelastic fluids. On the one hand, we have seen that there still a lot of work to be done with the so-called high-Weissenberg number problem. Although there has been a good progress in this regard, none of the computational schemes developed so far have shown to reproduce the experimental data (such as the terminal velocity of the bubbles). As shown by Frank & Li (2005), perhaps the easiest way to deal with this problem (without imposing additional constrains to the governing equations) is by using alternative schemes such as the Lattice Boltzmann models. On the other hand, one of the issues that have not been treated in depth is about the performance of the algorithms when two or more deformable bodies form a cluster. In this work we saw, for example, that the ALE code is capable to solve the flow of two bubbles (or even more, see figure 8.1b for a set of six bubbles rising in a Newtonian fluid) even though in some cases the gap between the two surfaces becomes very small (see figure 6.15). However, when this small space between the surfaces persist (when a stable doublet is formed), the numerical code becomes unstable and eventually fails to converge (figure 8.1a). In order to obtain satisfactory results in the future, this issue will also require special treatment. One of the strategies that can be proposed in this regard is the implementation of a collision model among deformable interfaces (something similar to what was proposed by Hu *et al.* 2001) or the use of the equations of motion but without the inertia terms (lubrication equations) only for the "difficult" regions. Another solution could be (simply) not to solve the equations of motion in the elements located in this narrow space. In any case, before thinking about a new strategy to solve the flow between the space left by two colliding bubbles, we need to see if other numerical schemes have the same problem. For instance, one may use the immersed boundary methods[16], and in particular, the diffuse-interface method (Yue *et al.* 2006), to see if the bubble clustering problem disappears.

The other subject that I want to consider are the implications that could have the clustering phenomenon in low Re flows and viscoelastic fluids in the aggregation of living cells. Before considering the influence of fluid dynamics in cell clustering, I must give a brief (non-specialized) summary of the subject from the traditional viewpoint. The development of multicellular organisms started about 1500 million years ago with the appearance of the first bacterial colonies (the appearance of the first individual cells was about 3500 million years ago). Plant cells like algae and animal cells (metazoa) also proved afterwards to be capable of establishing interactions and work division among the individual cells forming a cluster (Bonner 1998, Herron *et al.* 2009). The green algae (with a size of 10-20μm) was able, for example, to form aggregates composed of four cells up to 50,000 individual cells. Among the different theories that have been proposed to explain the origin of multicellularity, in the following just two of them will be described. The first one, the colonial theory, says that multicellularity arose from the cooperation of individual cells of the same specie that were in the beginning produced by other cells but then rejoined or that arose as a result of a partial failure of the cell division mechanism (the daughter cell will be attached to the mother cell and so on). The other one, the symbiotic theory, proposes that multicellularity was a result of the cooperation (again) of individual cells but that came form different species, i.e., having different roles since the beginning. Now, all the theories proposed so far by the traditional evolutionary biology assume that the mechanisms of multicellularity are mostly ruled by the genetic circuitry and the molecular pathways found in the living cells. For instance, no cell-to-cell communication or cell-cell adhesion had happened in the absence of a regulated production of organic molecules that will carry out these mechanism and others. Actually, cell differentiation resulted from the mutation (change) of the genetic information or from the different ways in “reading” this information among the different cells. Besides these genetic factors, several “physical” factors have been proposed that could explain the origin of multicellularity in ancient organisms that had more plasticity (change capacity) and a less controlled or integrated metabolism-genetic system (Furusawa & Kaneko 1993, Müller & Newman 2003, Newman *et al.* 2006). Among the physical factors that have been proposed we can find the ones that take into account the differences in surface tension among the cells, differential adhesion, gradients set up by diffusion or sedimentation, reaction-diffusion couplings. We can see that such factors do not rely directly on the genetic capacities of the organisms but simply on physical mechanisms[17].

---

[16] These methods consider the continuous and disperse phases as a single fluid, that is to say, the governing equations are solved through the entire domain (in our case, for example, the flow inside the bubbles is not solved). In order to do this, one needs to consider additional equations that takes into account the steep, but continuous, change of the material properties of the fluids in the interface (see Prosperetti & Tryggvason 2009).

[17] During the last year of my Ph.D. studies I realized that there is an increasing tendency of the engineers and physicist to address issues that were treated in the past exclusively by people form other disciplines, like biology. This has lead to a better understanding of the underlying physics governing the motion of living systems. See, for example, one of the papers written by E. Lauga entitled *“Life at high Deborah*

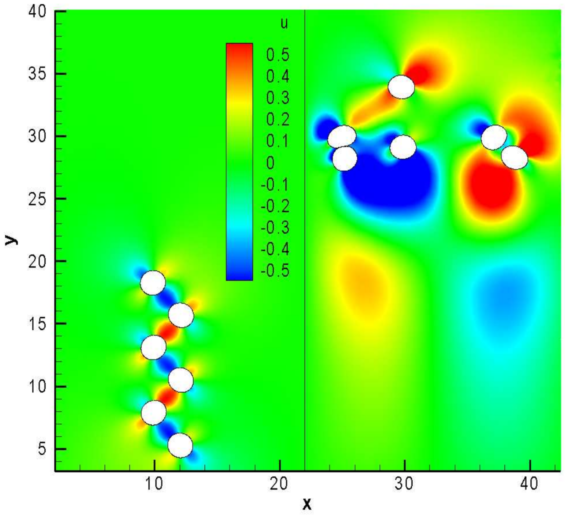

(a) $n = 0.7$, left image $t^* = 0.59$, right image $t^* = 12.59$

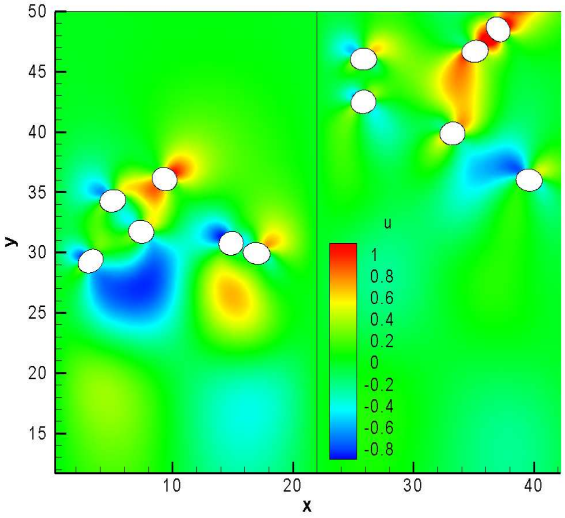

(b) Newtonian, left image $t^* = 12.59$, right image $t^* = 24.19$

Figure 8.1: Bubble positions and horizontal velocity map u (normalized with the terminal velocity of the single bubble) of a set of six bubbles released in the thinning fluid with $n = 0.76$ (a) and in its Newtonian counterpart (b). The image taken at the normalized time of $t^* = 0.59$ for the $n = 0.76$ fluid is identical to the one obtained with the Newtonian fluid at the same time. The code stopped at a $t^* = 12.59$ in the thinning case due to the formation of a bubble pair. Note that the bubble dispersion is different between one fluid and the other at time $t^* = 12.59$.

In view of these arguments, one might postulate that the clustering phenomenon seen in low Re viscoelastic fluids can be a suitable mechanism that could explain the aggregation of living cells. First of all, living cells are good candidates for clustering due to the low Re numbers (the size of the cells are in the order of microns) achieved if were submitted to some kind of flow (like sedimentation, shear inside a narrow channel, movement across the liquid surface). Secondly, the cells that had had a "soft" surface, like the animal cells, could have been more prone to form clusters due to the deformability character of their lipidic bilayer membrane. In the case where the primitive cells had also been submerged in a complex polymer solution (formed by a mix of proteins and nucleic acids), cell clustering could have been the rule rather than the exception; only the cells having a rigid membrane could have escaped from clustering in viscous thinning fluids. Although all the ideas described here are pure speculative, it is very intuitive to think that fluid dynamics at low Re and in viscoelastic fluids may explain by itself the aggregation phenomenon seen in living cells, i.e., the apparition of multicellular organisms. In this sense, the physical factors (or generic mechanisms, as named by Müller & Newmann 2003) could have left some bases on the organization of multicellularity; the morphology and dynamics of such mechanism was further resumed by the sophisticated genetic and biochemical systems, developed and established many years later.

---

number" (Lauga 2009), which is the non-Newtonian version of the classical paper of Purcell (Purcell 1977) entitled *"Life at low Reynolds number"*.

Chapter 9

Conclusions

More than fifty years have passed since the study of flows in polymeric solutions became a formal discipline. The state of the art and several important experiments and models on the subject can be found in the classic books of Bird *et al.* (1987), Barnes *et al.* (1989) and Chhabra (1993), among others. In this work we presented, in a systematic way, some of the main theoretical and experimental results that have been done in the field of bubble flows in non-Newtonian fluids. Advances and problems that still need to be solved were exposed. Also some contributions in the subject, which are summarized below, were offered.

The experimental setup consisted in producing a mono-dispersed bubbly flow in fluids with shear-thinning behavior ($0.3 < n < 1.0$) and negligible elasticity, on the one hand; and in fluids with high elasticity but nearly constant viscosity on the other. The bubble swarms experiments were complemented with the experimental and numerical study of the interaction of bubble pairs having different initial arrangements. For the experiments, a high speed camera and the Particle Image Velocimetry technique were used to characterize the flow field. The numerical simulations were conducted with the Arbitrary Lagrangian-Eulerian technique. The main message of this work can be summarized as follows: Bubble clustering in non-Newtonian fluids can be produced by the passive effect of the viscosity gradients or the active effect of the elastic restoring forces. In the case of the viscosity gradients effects, they do not act as a net force but rather decrease the momentum transfer between two neighboring bubbles due to the low viscosity zone produced by the bubble doublet. Since the thinning behavior is a generalization of the Newtonian liquids, its effects in bubble flows are decreased if the inertia of the system is increased (the viscosity gradients become less important) or if the surface forces become higher than the buoyancy forces (the coefficient of restitution is higher in the collision of two rigid bodies than in the collision of two deformable bodies). In the case of the elastic fluids, the restoring forces effect is active in the sense that they generate a perpendicular compressive force on the bubble flow making it form large vertical clusters. The elastic effects are, however, dependent on the boundary condition of the bubbles.

The main results obtained in the present work were the following:

Bubble pairs rising in thinning fluids

- Before contact, the bubble trajectories followed the general behavior found in Newtonian flows for $Re < 30$: a divergent path or repulsion is found between bubbles if the angle of approach lay within 40° from the horizontal, and a convergent path or attraction is observed otherwise.

- The wake formed behind a leading bubble attracts the trailing bubble. This attractive motion increased with the shear-thinning behavior (decreasing the flow index). Two bubbles in contact rising in a thinning fluid experience less drag than the bubbles rising in the Newtonian fluid counterpart, contrary to what is seen in the case of single bubbles. This effect is nevertheless hindered by the inertial effects.

- The numerical simulations suggested that the angle of inversion of the direction of the lift force between two rising bubbles can decrease due to the viscosity gradient formed near the horizontal plane of the bubbles when rising in a thinning fluid. This can lead to a more effective clustering if more than two bubbles are presented.

- After the drafting and kissing processes, bubbles rising in thinning fluids tend to stay together (not-tumbling) depending on the inertia and deformability of the single bubble. This proved to be an important difference between Newtonian and non-Newtonian flows. Furthermore, the bubbles forming pairs showed an oscillatory motion due to the reduced viscosity being formed by the leading bubble and the subsequent acceleration of the trailing one. In Newtonian flows, only the bubbles rising at $Re < 1$ formed pairs but did not showed such oscillatory behavior.

Bubble swarms rising in thinning fluids

- The visual observation of the flow revealed the formation of dense bubble clusters which grow with the gas fraction and increase the mean bubble velocity with respect to that achieved by single bubbles. Such clusters, which actually lead to contact between bubbles, have larger dimensions and lifetime than those observed in Newtonian potential flows.

- Qualitative agreement of the velocities ratio $\overline{U}_{SW}/U_{SI}$ as a function of the gas volume fraction was found with the theoretical studies of Gummalam and Chhabra (1987), and Chhabra (1998). Therefore, the Happel cell model can predict the effects of the reduction of the local viscosity together with the hydrodynamic hindrance provoked by bubble interactions.

- Quantitative agreement with the velocity ratio was not found between the experiments of this work and the theoretical predictions since the maximum of the velocity ratio $\overline{U}_{SW}/U_{SI}$ was found at lower gas fractions than those predicted by the theory. In fact, the permissible experimental gas fraction values are much lower than the theoretical ones for the cases of mono-dispersed bubbly flows. The heterogeneous or churn-turbulent regime has interesting issues by itself but cannot be used to compare experimental results with the available theoretical data.

- The magnitude of the velocity ratio $\overline{U}_{SW}/U_{SI}$ was higher than the theoretical one even at low values of the gas fraction. The difference is attributed to the formation of clusters which the Happel cell model does not account for.

- The ratio of the mean bubble velocity and the single bubble velocity did not follow an orderly correspondence with the flow index values, as seen in the theoretical works. Instead of this, the $\overline{U}_{SW}/U_{SI}$ values could be related to the values of the Reynolds and Eötvös numbers of the single bubbles. Moreover, the bubble clustering condition (and also the condition to form bubble pairs) was mapped in a Eo-Re plot. Two regimes were identified: a free bubble regime and a cluster formation regime. The limit between one and the other is close to a critical Morton number ($Mo = 4 \times 10^{-4}$) which has been identified as a transition indicator from non-coalescing to coalescing flows in Newtonian fluids.

- Measurements were also conducted to obtain the equivalent diameter of the bubble cluster and bubble velocity variance. These results suggest that the cluster growth is not related to the size of individual bubbles and that the dimensionless bubble velocity variance $T_b/\overline{U}^2_{SW}$ increases significantly when bubble clusters are formed.

Single bubbles and bubble pairs rising in Boger fluids

- For the first time it was shown that the velocity jump discontinuity, seen in the volume-velocity plot of single bubbles, can appear without the formation of a negative wake. The magnitude of the velocity jump and the formation of the negative wake are rather determined by the extensional properties of the fluid. The results obtained for single bubbles in the Boger-1 fluid and bubble groups in the Boger-2 fluid suggest that the change of the boundary conditions at the bubble surface is an important mechanism that triggers the velocity jump.

- Bubbles having a volume below the critical one tend to form clusters when rising as a pair of chains just when a certain value of the injection rate is exceeded. The results suggest that the accumulation of the restoring forces in the flow due to the consecutive passage of bubbles plays an important role in clustering formation. This feature was investigated by analyzing the unsteady behavior of the first normal stress difference.

Bubble swarms rising in Boger fluids

- The bubble dispersion and distribution of the velocity fluctuations (variance of the vertical velocity) in the liquid proved to be highly dependent on the bubble size: below the critical volume, the bubbles tended to form a large vertical cluster and hence segregation of the dispersed phase was observed; on the other hand, when the bubble size was above the critical one, the bubble dispersion and spatial distribution of the mean agitation levels were notably improved. Additionally, it was also observed that a recirculation loop of the liquid often appears in fully developed viscous elastic flows.

In addition to all these points, there are some practical applications that could emerge form this work. For instance, it is commonly accepted that bubble flows produced by small bubbles will render high values of the mass transfer coefficients. However, we have seen that bubble clusters are easily form with small bubble sizes and the dispersion of the gas decreased as a consequence. Hence, we may consider a bubble column equipped with two sets of capillary banks: one for the production of small bubbles and the other for the production of large bubbles (see Serrano-Garcia *et al.*). The proportion in volume of one size with the other could be operated according to the rheological properties of the working fluid.

The present work also constitutes one of the initial steps towards the understanding of bubbly flows in shear-thinning elastic fluids. We have seen that bubble clouds are formed in thinning fluids specially when the bubble surface is highly deformable; on the other hand, vertical clusters are formed in elastic fluids when the bubble surface presents a no-slip condition. Hence, we can expect a high variety of clustering structures in fluids having both behaviors. A key variable that could be use to interpret the results obtained in viscoelastic fluids is the parameter c, defined as the ratio of the polymer and solvent contribution to the zero-shear viscosity.

It is my hope that this work will contribute to the understanding of the formation of bubble clusters in non-Newtonian fluids, which is an important issue in multiphase flows as well as a precursor to bubble coalescence and change of regime in bubble flows.

Bibliography

[1] Acharya A., Mashelkar R.A., Ulbrecht J., Mechanics of Bubble Motion and Deformation in Non-Newtonian Media, Chem. Eng. Sci. 32 (1977) 863.

[2] Ardekani A.M., Sharma V.,McKinley G.H., Dynamics of Bead Formation, Filament Thinning, and Breakup in Weakly Viscoelastic Jets, J. Fluid Mech. 665 (2010) 46.

[3] Astarita G., Apuzzo G., Motion of gas bubbles in non-Newtonian liquids, A.I.Ch.E. J. 11 (1965) 815.

[4] Barnes H.A., Hutton J.F., Walters K., An Introduction to Rheology, Rheology series 3, Elsevier, 1989.

[5] Batchelor G.K. An Introduction to Fluid Dynamics, Cambridge University Press, U.K., 1991.

[6] Bautista F., de Santos J.M., Puig J.E., Manero O., Understanding thixotropic and antithixotropic behavior of viscoelastic micellar solutions and liquid crystalline dispersions. I. The model, J. non-Newtonian Fluid Mech., 80 (1999) 93.

[7] Bhaga D., Weber M.E., In-line interaction of a pair of bubbles in a viscous liquid, Chem. Eng. Sci. 35 (1980) 2467.

[8] Bhavaraju S.M., Mashelkar R.A., Blanch H.W., Bubble motion and mass transfer in non-newtonian fluids: Part I. Single Bubble in Power Law and Bingham Fluids, A.I.Ch.E. J. 24 (1978a) 1063.

[9] Bhavaraju S.M., Mashelkar R.A., Blanch H.W., Bubble motion and mass transfer in non-newtonian fluids: Part II. Swarm of bubbles in a power law fluid, A.I.Ch.E. J. 24 (1978b) 1070.

[10] Biesheuvel A., van Wijngaarden L., The motion of pairs of gas bubbles in a perfect liquid, J. Eng. Math. 16 (1982) 349.

[11] Bird R.B., Armstrong R.C., Hassager O., Dynamics of polymeric liquids, volume 1, John Wiley & Sons, USA, 1987.

[12] Bird R.B., Stewart W.E., Lightfoot E.N., Fenómenos de Transporte, Reverté, México, 1998.

[13] Bonner, J.T., The origins of multicellularity, Integrative Biology 1 (1998) 27.

[14] Brennen C.E., Fundamentals of Multiphase Flow, Cambridge University Press, 2005.

[15] Buchholz H., Buchholz R., Lücke J., Schügerl K., Bubble swarm behavior and gas absortion in non-Newtonian fluids in sparged columns, Chem. Eng. Sci. 33 (1978) 1061.

[16] Calderas F., Sanchez-Solis A., Maciel A., Manero O., The Transient Flow of the PET-PEN-Montmorillonite Clay Nanocomposite,Macromol. Symp. 283-284 (2009) 354.

[17] Cartellier A., Timkin L., Rivière N., New structures of Poiseuille bubbly flows due to clustering, Proc. ASME-FEDSM 97, paper 3528, Vancouver, June 22-26, 1997.

[18] Cartellier A., Rivière N., Bubble-induced agitation and microstructure in uniform bubbly flows at small to moderate particle Reynolds numbers, Phys. Fluids 13 (2001) 2165.

[19] Chehata D., Estudio de la Discontinuidad en la Velocidad de Ascenso de una Burbuja en un Fluido no Newtoniano, M.Sc. thesis, Universidad Nacional Autónoma de México, 2004.

[20] Chhabra R.P., Bubbles, Drops and Particles in Non-Newtonian Fluids, CRC, Boca Raton, FL, 1993.

[21] Chhabra R.P., Rising velocity of a swarm of spherical bubbles in power law fluids at high Reynolds numbers, Can. J. Chem. Eng. 76 (1998) 137.

[22] Choplin L., Sabatié J., Treshold-type shear-thickening in polymer solutions, Rheol. Acta 25 (1986) 570.

[23] Chung T.J., Computational Fluid Dynamics, Cambridge University Press, UK, 2002.

[24] Clift R., Grace J.R., Weber M.E., Bubbles, Drops, and Particles, Academic Press, NY, 1978.

[25] Crabtree J.R., Bridgwater J., Bubble coalescence in viscous liquids, Chem. Eng. Sci. 26 (1971) 839.

[26] Currie I.G., Fundamental Mechanics of Fluids, McGraw Hill, 1974.

[27] Deckwer W.-D., Nguyen-tien K., Schumpe A., Serpemen Y., Oxygen mass transfer into aerated CMC solutions in a bubble column, Biotechol. Bioeng. 24 (1982) 461.

[28] Deckwer W.-D., Bubble column reactors, Wiley, NY, 1992.

[29] Dijkhuizen W., van Sint Annaland M., Kuipers J.A.M., Numerical and experimental investigation of the lift force on single bubbles, Chem. Eng. Sci. 65 (2010) 1274.

[30] Dhole S.D., Chhabra R.P., Eswaran V., Drag of a Spherical Bubble Rising in Power Law Fluids at Intermediate Reynolds Numbers, Ind. Eng. Chem. Res. 46 (2007) 939.

[31] Doi H., Edwards S.F., The Theory of Polymer Dynamics, Clarendon-Oxford University Press, Northern Ireland, 1986.

[32] Dou H.-S., Phan-Thien N., Criteria of negative wake generation behind a cylinder, Rheol. Acta 43 (2004) 203.

[33] Ekambara K., Dhotre M.T., Joshi J.B., CFD simulations of bubble column reactors: 1D, 2D and 3D approach, Chem. Eng. Sci. 60 (2005) 6733.

[34] Fattal R., Fupferman R., Time-dependent simulation of viscoelastic flows at high Weissenberg number using the log-conformation representation, J. non-Newtonian Fluid Mech. 126 (2005) 23.

[35] Feys D., Verhoeven R., De Schutter G., Why is fresh self-compacting concrete shear thickening?, Cement and Concrete Research 39 (2009) 510.

[36] Figueroa-Espinoza B., Zenit R., Clustering in high Re monodispersed bubbly flows, Phys. Fluids 17 (2005) 091701.

[37] Frank X., Li H.Z., Complex flow around a bubble rising in a non-Newtonian fluid, Phys. Rev. E, 71 (2005) 036309.

[38] Furusawa C., Kaneko K., Origin of Multicellular Organisms as an Inevitable Consequence of Dynamical Systems, The Anatomical Record 268 (2002) 327.

[39] Galaction A.-I., Cascaval D., Oniscu C., Turnea M., Prediction of oxygen mass transfer coefficients in stirred bioreactors for bacteria, yeast and fungus broths, Biochem. Eng. J. 20 (2004) 85.

[40] Gavrilescu M., Chisti Y., Biotechnology—a sustainable alternative for chemical industry, Biotech. Adv. 23 (2005) 471.

[41] Gheissary G., van den Brule B.H.A.A., Unexpected phenomena observed in particle settling in non-Newtonian media, J. non-Newtonian Fluid Mech. 67 (1996) 1.

[42] Gill P.E., Murray W., Wright, M.H., Numerical Linear Algebra and Optimization, volume 1, The Advance Book Program, Addison-Wesley Publishing Company, CA, 1991.

[43] Godbole S.P., Schumpe A., Shah Y.T., Carr N.L., Hydrodynamics and Mass Transfer in Non-Newtonian Solutions in a Bubble Column, A.I.Ch.E. J. 30 (1984) 213.

[44] Götze L., Bailer O., Moritz P. (von Scala), Reactive distillation with KATAPAK, Catalysis Today 69, 1-4 (2001) 201.

[45] Gummalam S., Chhabra R.P., Rising velocity of a swarm of spherical bubbles in a power law non-Newtonian liquid, Can. J. Chem. Eng. 65 (1987) 1004.

[46] Hallez Y., Legendre D., Interaction between two spherical bubbles rising in a viscous liquid, published on line on March 02 2011.

[47] Happel J., Viscous flow in multiparticle systems: slow motion of fluids relative to beds of spherical particles, A.I.Ch.E. J. 4 (1958) 197.

[48] Happel J., Pfeffer R., The motion of two spheres following each other in a viscous fluid, A.I.Ch.E. J. 6 (1960) 129.

[49] Happel J., Brenner H., Low Reynolds number hydrodynamics with special applications to particulate media, Kluwer Academic Publishers, The Netherlands, 1991.

[50] Haque N.W., Nigam K.D.P., Viswanathan K., Joshi J.B., Studies on Gas Holdup and Bubble Parameters in Bubble Columns with (Carboxymethyl)cellulose Solutions, Ind. Eng. Chem. Res. 26 (1987) 86.

[51] Haque N.W., Nigam K.D.P., Viswanathan K., Joshi J.B., Studies on bubble rise velocity in bubble columns employing non-Newtonian solutions, Chem. Eng. Comm. 73 (1988) 31.

[52] Heijnen J.J., van't Riet K., Mass Transfer, Mixing and Heat Transfer Phenomena in Low Viscosity Bubble Column Reactors, Review Paper, Chem. Eng. J. 28 (1984) B21.

[53] Herrera-Velarde J.R., Zenit R., Chehata D., Mena B., The flow of non-Newtonian fluids around bubbles and its connection to the jump discontinuity, J. Non-Newtonian Fluid Mech. 111 (2003) 199.

[54] Herron M.D., Hackett J.D., Aylward F.O., Hichod R.E., Triassic origin and early radiation of multicellular volvocine algae, PNAS 106 (2009) 3252.

[55] Hirose T., Moo-Young M., Bubble Drag and Mass Transfer in non-Newtonian Fluids: Creeping Flow with Power-law Fluids, Can. J. Chem. Eng. 47 (1969) 265.

[56] Hocking L.M., The behavior of clusters of spheres falling in a viscous fluid. J. Fluid Mech. 20 (1964) 129.

[57] Hu H.H., Patankar N.A., Zhu M.Y., Direct Numerical Simulations of Fluid-Solid Systems Using the Arbitrary Lagrangian-Eulerian Technique, J. Comput. Phys. 169 (2001) 427.

[58] Humphrey A.E., Elmer L. Gaden Jr., Father of Biochemical Engineering, Biotech. Bioeng. 37 (1991) 995.

[59] Indei T., Necessary conditions for shear thickening in associating polymer networks, J. Non-Newtonian Fluid Mech. 141 (2007) 18.

[60] Ishii M., Zuber N., Drag Coefficient and Relative Velocity in Bubbly, Droplet or Particulate Flows, A.I.Ch.E. J. 25 (1979) 843.

[61] James D.F., Boger fluids, Annu. Rev. Fluid Mech. 41 (2009) 129.

[62] Jayaweera K.O.L.F., Mason B.J., Slack G.W., The behavior of cluster of spheres falling in a viscous fluid, J. Fluid Mech. 20 (1964) 121.

[63] Jones D.M., Walters K., Williams P.R., On the extensional viscosity of mobile polymer solutions, Rheol. Acta 26 (1987) 20.

[64] Joseph D.D., Liu Y.J., Orientation of long bodies falling in a viscoelastic liquid, J. Rheol. 37 (1993) 961.

[65] Joseph D.D., Liu Y.J., Poletto M., Feng J., Aggregation and dispersion of spheres falling in viscoelastic liquids, J. non-Newtonian Fluid Mech. 54 (1994) 45.

[66] Joseph D.D., Feng J., A note on the forces that move particles in a second-order fluid, J. non-Newtonian Fluid Mech. 64 (1996) 299.

[67] Kantarci N., Borak F., Ulgen K.O., Bubble column reactors, Process Biochem. 40 (2005) 2263.

[68] Katz J., Meneveau C., Wake-induced Relative Motion of Bubbles Rising In Line, Int. J. Multiphase Flow 22 (1996) 239.

[69] Katzen R., Tsao G.T., A View of the History of Biochemical Engineering, Adv. Biochem. Eng. Biotech., 70 (2000) 77.

[70] Kemiha M., Frank X., Poncin S., Li H.Z., Origin of the negative wake behind a bubble rising in non-Newtonian fluids, Chem. Eng. Sci. 61 (2006) 4041.

[71] Kilonzo P.M., Margaritis A., The effects of non-Newtonian fermentation broth viscosity and small bubble segregation on oxygen mass transfer in gas-lift bioreactors: a critical review, Biochem. Eng. J. 17 (2004) 27.

[72] Kim I., Elghobashi S., Sirignano W.A., Three-dimensional flow over two spheres placed side by side, J. Fluid Mech. 246 (1993) 465.

[73] Kishore N., Chhabra R.P., Eswaran V., Drag on ensembles of fluid spheres translating in a power-law liquid at moderate Reynolds numbers, Chem. Eng. J. 139 (2008) 224.

[74] Kok J.B.W., Dynamics of a pair of gas bubbles moving through liquid. Part I. Theory, Eur. J. Mech. B/Fluids 12 (1993a) 515.

[75] Kok J.B.W., Dynamics of a pair of gas bubbles moving through liquid. Part II. Experiment, Eur. J. Mech. B/Fluids 12 (1993b) 541.

[76] Kwon Y.W., Bang H., The Finite Element Method using MATLAB, CRC Press, USA, 1997.

[77] Larson R.G., The Structure and Rheology of Complex Fluids, Oxford University Press, 1999.

[78] Lauga E., Life at high Deborah number, Europhys. Lett. 86 (2009) 64001.

[79] Lawford H., Rousseau J., Bioreactor design considerations in the production of high-quality microbial exopolysaccharide, Appl. Biochem. Biotecnnol. 28/29 (1991) 667.

[80] Legendre D., Magnaudet J., Mougin G., Hydrodynamic interactions between two spherical bubbles rising side by side in a viscous liquid, J. Fluid Mech. 497 (2003) 133.

[81] Lessard R.R., Zieminski S.A., Bubble coalescence and gas transfer in aqueous electrolytic solutions, Ind. Eng. Chem. Fundam. 10 (1971) 260.

[82] Li H.Z., Mouline Y., Choplin L., Midoux N., Rheological Simulation of In-line Bubble Interactions, A.I.Ch.E.J. 43 (1997) 265.

[83] Li H.Z., Mouline Y., Funfschilling D., Marchal P., Choplin L., Midoux N., Evidence for in-line bubble interactions in non-Newtonian fluids, Chem. Eng. Sci. 53 (1998) 2219.

[84] Li H.Z., Frank X., Funfschilling D., Mouline Y., Towards the understanding of bubble interactions and coalescence in non-Newtonian fluids: a cognitive approach, Chem. Eng. Sci. 56 (2001) 6419.

[85] Liang S.-C., Hong T., Fan L.-S., Effects of Particle Arrangements on the Drag Force of a Particle in the Intermediate Flow Regime, Int. J. Multiphase Flow 22 (1996) 285.

[86] Liao Y., Lucas D., A literature review on mechanisms and models for the coalescence process of fluid particles, Chem. Eng. Sci. 65 (2010) 2851.

[87] Lind S.J., Phillips T.N., The effect of viscoelasticity on a rising gas bubble," J. Non-Newtonian Fluid Mech. 165 (2010) 852.

[88] Liu Y.J., Liao T.Y., Joseph D.D., A two-dimensional cusp at the trailing edge of an air bubble rising in a viscoelastic liquid, J. Fluid Mech. 304 (1995) 321.

[89] Macosko C.W., Rheology Principles, Measurements and Applications, Wiley-VCH, USA, 1994.

[90] Manga M., Stone H. A., Buoyancy-driven interactions between two deformable viscous drops, J. Fluid Mech. 256 (1993) 647.

[91] Manga M., Stone H. A., Collective hydrodynamics of deformable drops and bubbles in dilute low Reynolds number suspensions, J. Fluid Mech. 300 (1995) 231.

[92] Mark J.E. (Ed.), Polymer Data Handbook, Oxford University Press, N.Y., 1999.

[93] Martínez-Mercado J., Palacios-Morales C.A., Zenit R., Measurement of pseudoturbulence intensity in monodispersed bubbly liquids for $10 < Re < 500$, Phys. Fluids 19 (2007) 103302.

[94] Mase G.E., Continuum Mechanics, Schaum's Outline Series, McGraw Hill, 1970.

[95] Mena B., Manero O., Leal L.G. The Influence of Rheological Properties on the Slow Flow Past Spheres, J. non-Newtonian Fluid Mech. 26 (1987) 247.

[96] Mendenhall W., Sincich T., Probabilidad Y Estadística para Ingeniería y Ciencias, 4a. Ed., Prentice Hall, México, 1997.

[97] Mendoza-Fuentes A.J., Montiel R., Zenit R., Manero O., On the flow of associative polymers past a sphere: Evaluation of negative wake criteria, Phys. Fluids 21 (2009) 033104.

[98] Metz, B., de Bruijn E.W., van Suidam J.C., Methods for quantitative representation of the morphology of molds, Biotechnol. Bioeng. 23 (1981) 149.

[99] Michele J., Pätzold R., Donis R., Alignment and aggregation effects in suspensions of spheres in non-Newtonian media, Rheol. Acta 16 (1977) 317.

[100] Morrison F.A., Breakup of a bubble chain, Chem. Eng. Sci. 28 (1973) 1115.

[101] Morrison F.A., Undestanding Rheology, Oxford University Press, USA, 2001.

[102] Müller G.B., Newman S.A., Origination of Organismal Form, Beyond the Gene in Developmental and Evolutionary Biology, MIT Press, 2003.

[103] Narayanan S., Goossens L.H.J., Kossen N.W.F., Coalescence of two bubbles rising in line at low Reynolds numbers, Chem. Eng. Sci. 29 (1974) 2071.

[104] Newman S.A., Forgacs G., Müller G.B., Before programs: The physical origination of multicellular forms, Int. J. Dev. Biol. 50 (2006) 289.

[105] Nienow A.W., Agitators for mycelial fermentations, Trends in Biotechnology, 8 (1990) 224.

[106] Nighgate D.J., Particle Migration in Cone-plate Viscometry of Suspensions, Nature 211 (1966) 1390.

[107] Nighgate D.J., Whorlow R.W., End effects and particle migration effects in concentric cylinder rheometry, Rheol. Acta 8 (1969) 142.

[108] Oĝuz H.N., Prosperetti A., Dynamics of bubble growth and detachment from a needle, J. Fluid Mech. 257 (1993) 111.

[109] Palacios C.A.M. Estudio de la velocidad fluctuante de la fase continua de una mezcla gas-líquido. M.Sc. thesis, Universidad Nacional Autónoma de México, 2005.

[110] Pelletier E., Viebke C., Meadows J., Williams P.A., Dilute Polyacrylamide Solutions under Uiaxial Extensional Flow, Langmuir 19 (2003) 559.

[111] Peña C., Galindo E., Díaz M., Effectiveness factor in biological external convection: study in high viscosity systems, J. Biotechnol. 95 (2002) 1.

[112] Petrie C.J.S., One hundred years of extensional flow, J. non-Newtonian Fluid Mech. 137 (2006) 1.

[113] Phan-Thien N., Tanner R.I., A new constitutive equation derived from network theory, J. non-Newtonian Fluid Mech. 2 (1977) 353.

[114] Phillips R.J., Talini L., Chaining of weakly interacting particles suspended in viscoelastic fluids, J. Non-Newtonian Fluid Mech. 147 (2007) 175.

[115] Pillapakam S.B., Singh P., Blackmore D., Aubry N., Transient and steady state of rising bubble in a viscoelastic fluid, J. Fluid Mech. 589 (2007) 215.

[116] Pilz C., Brenn G., On the critical bubble volume at the rise velocity jump discontinuity in viscoelastic liquids, J. Non-Newtonian Fluid Mech. 145 (2007) 122.

[117] Prosperetti A., Tryggvason G., Computational Methods for Multiphase Flow, Cambridge University Press, U.K., 2009.

[118] Purcell E.M., Life at low Reynolds number, American Journal of Physics 45 (1977) 3.

[119] Radl S., Tryggvason G., Khinast J.G., Flow and Mass Transfer of Fully Resolved Bubble in Non-Newtonian Fluids, A.I.Ch.E. J. 53 (2007) 1861.

[120] Riddle M.J., Narvaez C., Bird R.B., Interactions between two spheres falling along their line of centers in a viscoelastic fluid, J. non-Newtonian Fluid Mech. 2 (1977) 23.

[121] Rodrigue D., De Kee D., Chan Man Fong C.F., Bubble velocities: further developments on the jump discontinuity, J. Non-Newtonian Fluid Mech. 79 (1998) 45.

[122] Rodrigue D., De Kee D., Chan Man Fong C.F., A Note on the Drag Coefficient of a Single Gas Bubble in a Power-Law Fluid, Can. J. Chem. Eng. 77 (1999a) 766.

[123] Rodrigue D., De Kee D., Bubble velocity jump discontinuity in polyacrylamide solutions: a photographic study, Rheol. Acta 38 (1999b) 177.

[124] Rodrigue D., De Kee D., Recent Developments in the Bubble Velocity Jump Discontinuity, in Transport Processes in bubbles, drops and particles, Edit. De Kee D., Chhabra R.P., Taylor and Francis G.B., 2002.

[125] Rodríguez-Monroy M., Galindo E., Broth rheology, growth and metabolite production of *Beta vulgaris* suspension culture: a comparative study between cultures grown in shake flasks and in a stirred tank, Enzyme and Microbial Technology 24 (1999) 687.

[126] Rushton E., Davies G.A., Slow unsteady settling of two fluid spheres along their line of centers, Appl. Sci. Res. 28 (1973) 37.

[127] Ruzicka M.C., On bubbles rising in line, Int. J. Multiphase Flow 26 (2000) 1141.

[128] Sanada T., Sato A., Shirota M., Watanabe M., Motion and coalescence of a pair of bubbles rising side by side, Chem. Eng. Sci. 64 (2009) 2659.

[129] Schumpe A., Deckwer W.-D., Gas holdups, specific interfacial areas, and mass transfer coefficients of aerated carboxymethyl cellulose solutions in a bubble column, Ind. Eng. Chem. Process Des. Dev. 21 (1982) 706.

[130] Sámano D., Estudio de la interacción de dos burbujas en líquidos adelgazantes, B.S. thesis, Universidad Nacional Autónoma de México, 2011.

[131] Serrano-Garcia J.C., Méndez S. Zenit R., The average properties of bidisperse bubbly flows, personal comunication, paper in elaboration.

[132] Shah Y.T., Kelkar B.G., Godbole S.P., Deckwer W.-D., Design parameters estimation for bubble column reactors, A.I.Ch.E. J. 28 (1982) 353.

[133] Singh P., Leal L.G., Finite-Element Simulation of the Start-Up Problem for a Viscoelastic Fluid in an Eccentric Rotating Cylinder Geometry Using a Third-Order Upwind Scheme, Theor. Computational Fluid Dynamics 5 (1993) 107.

[134] Singh J.P., Denn M.M., Interacting two-dimensional bubbles and droplets in a yield-stress fluid, Phys. Fluids 20 (2008) 040901.

[135] Smolianski A., Haario H., Luukka P., Numerical study of dynamics of a single bubbles and bubbles swarm, Appl. Math. Model. 23 (2008) 641.

[136] Soto E., Goujon C., Zenit R., Manero O., A study of velocity discontinuity for single air bubbles rising in an associative polymer, Phys. Fluids 18 (2006) 121510.

[137] Soto E., Zenit R., Manero O., Breakup of the tail of a bubble in a non-Newtonian fluid, Phys. Fluids 20 (2008) 091110.

[138] Sousa R.G., Pinto A.M.F.R., Campos J.B.L.M., Interaction between Taylor bubbles rising in stagnant non-Newtonian fluids, Int. J. Multiphase Flow 33 (2007) 970.

[139] Spelt P.D.M., Sangani A.S., Properties and Averaged Equations for Flows of Bubbly Liquids, Appl. Sci. Res. 58 (1998) 337.

[140] Stelter M., Brenn G., Yarin A.L., Singh R.P., Durst F., Validation and application of a novel elongational device for polymer solutions, J. Rheol. 44 (2000) 595.

[141] Stelter M., Brenn G., Yarin A.L., Singh R.P., Durst F., Investigation of the elongational behavior of polymer solutions by means of an elongational rheometer, J. Rheol. 46 (2002) 507.

[142] Stewart C.W., Bubble interaction in low-viscosity liquids, Int. J.Multiphase Flow 21 (1995) 1037.

[143] Stimson M., Jeffery G.B., The Motion of Two Spheres in a Viscous Fluid, Proc. Roy. Soc. A111 (1926) 110.

[144] Sullivan M.T., Moore K., Stone H.A., Transverse Instability of Bubbles in Viscoelastic Channel Flows, Phys. Rev. Lett. 101 (2008) 244503.

[145] Tan H., Tam K.C., Tirtaatmadja V., Jenkins R.D., Bassett D.R., Extensional properties of model hydrophobically modified alkali-soluble associative (HASE) polymer solutions., J. Non-Newtonian Fluid Mech. 4 (2000) 167.

[146] Tsamopoulos J., Dimakopoulos Y., Chatzidai N., Karapetsas G., Pavlidis M., Steady bubble rise and deformation in Newtonian and viscoplastic fluids and conditions for bubble entrapment, J. Fluid Mech. 601 (2008) 123.

[147] Tse K. L., Martin T., McFarlane C. M., Nienow A. W., Small bubble formation via a coalescence dependent break-up mechanism, Chem. Eng. Sci. 58 (2003) 275.

[148] Ulbrecht J.J., Kaykara Z.S., Significance of the central plume velocity for the correlation of liquid phase mixing in bubble columns, Chem. Eng. Commun, 10 (1981) 165.

[149] Van Wijngaarden L., Hydrodynamic interaction between gas bubbles in liquid, J. Fluid Mech. 77 (1976) 27.

[150] Van Wijngaarden L., On pseudo turbulence, Theor. Comput. Fluid Dyn. 10 (1998) 449.

[151] Vasseur P., Cox R. G., The lateral migration of spherical particles sedimenting in a stagnant bounded fluid, J. Fluid Mech. 80 (1977) 561.

[152] Vélez-Cordero J.R., Zenit R., Bubble cluster formation in shear-thinning inelastic bubbly columns, J. Non-Newtonian Fluid Mech. 166 (2011a) 32.

[153] Vélez-Cordero J.R., Sámano D., Yue P., Feng J.J., Zenit R., Hydrodynamic interaction between a pair of bubbles ascending in shear-thinning inelastic fluids, J. Non-Newtonian Fluid Mech. 166 (2011b) 118.

[154] Vélez-Cordero J.R., Sámano D., Zenit R., The bubble velocity discontinuity in elastic fluids with constant viscosity, under consideration for publication in J. Fluid Mech., 2011c.

[155] Vélez-Cordero J.R., Sámano D., Zenit R., Elasticity can produce agglomeration or dispersion in particulate flows, under consideration for publication in Phys. Rev. Lett., 2011d.

[156] Watanabe M., Sanada T., In-LineMotion of a Pair of Bubbles in a Viscous Liquid, JSME International J., Series B, 49 (2006) 410.

[157] Wenyuan F., Youguang M., Xiaolei L., Huaizhi L., Study on the Flow Field around Two Parallel Moving Bubbles and Interaction Between Bubbles Rising in CMC Solutions by PIV, Chin. J. Chem. Eng. 17 (2009) 904.

[158] Yang F., Bick A., Shandalov S., Brenner A., Oron G., Yield stress and rheological characteristics of activated sludge in an airlift membrane bioreactor, Journal of Membrane Science, 334, 1-2 (2009) 83.

[159] Yuan H., Prosperetti A., On the in-line motion of two spherical bubbles in a viscous fluid, J. Fluid Mech. 278 (1994) 325.

[160] Yue P., Zhou C., Feng J.J., Ollivier-Gooch C.F., Hu H.H., Phase-field simulations of interfacial dynamics in viscoelastic fluids using finite elements with adaptive meshing, J. Comput. Phys. 219 (2006) 47.

[161] Yue P., Feng J.J., Bertelo C.A., Hu H.H., An arbitrary Lagrangian-Eulerian method for simulating bubble growth in polymer foaming, J. Comput. Phys. 226 (2007) 2229.

[162] Zana E., Leal L.G., The dynamics and dissolution of gas bubbles in a viscoelastic fluid, Int. J. Multiph. Flow 4 (1978) 237.

[163] Zenit R., Koch D.L., Sangani A.S., Measurements of the average properties of a suspension of bubbles rising in a vertical channel, J. Fluid Mech., 429 (2001) 307.

[164] Zhang J., Fan L.-S., On the rise velocity of an interactive bubble in liquids, Chem. Eng. J. 92 (2003) 169.

[165] Zhang L., Yang C., Mao Z.-S., Numerical simulation of a bubble rising in shear-thinning fluids, J. Non-Newtonian Fluid Mech. 165 (2010) 555.

[166] Zhu C., Lam K., Chu H.-H., Tang X.-D., Liu G., Drag Forces of interacting spheres in power-law fluids, Mech. Res. Commun. 30 (2003) 651.

[167] Zlokarnik M., Trends and Needs in Bioprocess Engineering, Chem. Eng. Progress 86 (1990) 62.